Fingerprint Recognition: Contributions to Latent Matching and 3D Fingerprint Target Generation

By

Sunpreet Singh Arora

A Dissertation

Submitted to
Michigan State University
in partial fulfillment of the requirements
for the degree of

Computer Science – Doctor of Philosophy

2016

ABSTRACT

FINGERPRINT RECOGNITION: CONTRIBUTIONS TO LATENT MATCHING AND 3D FINGERPRINT TARGET GENERATION

By

Sunpreet Singh Arora

Automatic fingerprint capture and comparison methods have led to the ubiquitous use of fingerprint-based person recognition in applications ranging from law enforcement and border control to national identification and smartphone unlock. However, despite tremendous advancements in the state-of-the-art, improvements are still needed in case of some challenging applications, e.g, to recognize poor quality and distorted fingerprints acquired from non-cooperative users, improve fingerprint reader fidelity, and determine anti-spoofing capability of different fingerprint readers. In this thesis, we address two such impending challenges: (i) comparison of latent prints found at crime scenes to large collections of reference prints (rolled tenprints or slap fingerprints) in law enforcement databases, and (ii) operational evaluation of fingerprint recognition systems prior to large scale deployment.

We develop a feedback paradigm that uses reference print features to dynamically select latent features during matching. The paradigm automatically determines if dynamic latent feature selection would improve recognition performance using a statistical hypothesis test and qualitatively decides the regions in latent and reference prints for applying feedback. The paradigm when used in conjunction with a state-of-the-art latent matcher demonstrates marked improvement (0.5-3.5%) in latent matching accuracy.

Further, we develop a framework for crowdsourcing latent print feature markup to a pool of fingerprint examiners. The framework uses a statistical criterion to automatically determine when crowdsourcing is required, and a method to dynamically determine the number of examiners needed for latent feature markup. Significant recognition performance improvements (2.5-11.5%) are obtained using crowdsourced markups in conjunction with a state-of-the-art latent matcher.

Finally, we design and fabricate single-finger and whole hand 3D targets for operational evaluation of optical and capacitive fingerprint readers as well as for end-to-end evaluation of fingerprint recognition systems. 2D calibration patterns with known characteristics (e.g. synthetic fingerprints with known features, sine gratings with known orientation and spacing) are projected onto electronic 3D finger and hand surfaces to create electronic 3D single-finger and whole hand targets. A high-resolution 3D printer is used to manufacture physical 3D single-finger and whole hand targets from electronic targets. Other contributions include: (i) a method to chemically clean the 3D printed targets without impacting the engraved target patterns, (ii) a procedure to apply conductive coating of metal/metal oxides on the surface of 3D targets using DC sputtering, (iii) fidelity measurement techniques using optical microscopy to assess the 3D target generation process, and (iv) methods to evaluate fingerprint readers using the fabricated 3D targets. We demonstrate that the 2D calibration pattern features are reproduced with high fidelity both on the electronic and physical 3D single-finger and whole hand targets and that the intra-class variations between images of the 3D targets do not degrade matching accuracy (at 0.01% false accept rate). We evaluate several commercially available single-finger and slap contact-based and contactless optical readers as well as capacitive readers using the generated 3D targets.

To all my loved ones.

ACKNOWLEDGMENTS

As I sit down to write this dissertation, I would like to take the opportunity to thank all my teachers, including my parents, primary, middle school and high school teachers, university professors and peers, who have taught me wonderful things, and from whom I have assimilated a majority of my life learnings. I will always remain indebted to all of you for not only sharing your knowledge but also fueling my curiosity to explore and learn.

I am grateful to my advisor, Dr. Anil K. Jain for his encouragement and support at both professional and personal level. He backed me to the hilt while I was trying to stand on my own feet as a researcher. Once I did, he let me take my own flight and explore. I am also thankful to Dr. Xiaoming Liu, Dr. Arun Ross and Dr. Selin Aviyente for serving on my Ph.D. committee.

The PRIP lab provided me the right kind of environment for learning. Interactions with peers in the lab during the last four years have not only advanced my knowledge but helped me appreciate the nuances of research. Specifically, I would like to mention a few who have left a lasting impression on me due to their sincerity, hard work, and tenacity: Soweon, Serhat, Radha, Alessandra, Scott, Lacey, Tarang, Keyur, Charles, Inci, Josh, Debayan, Kai, Hu, and Eryun. I would especially like to thank Kai for all his help during my formative years. A few special mentions: Scott for being the one I could exchange ideas with for the first couple of years, Charles and Inci for being really good friends and for listening to my day-to-day graduate life issues patiently over lunch, and Lacey for being the frequent flyer companion to attend various conferences together around the world.

I would like to acknowledge the following organizations and individuals for generously supporting the research projects I worked on: Nicholas G. Paulter Jr. from the National Institute of Standards and Technology (NIST), NIST Measurement Science program grant 60NANB11D155, the National Science Foundation (NSF) Center for Identification Technology Research (CITeR) grant 1066197, Ken Warman from the Bill and Melinda Gates Foundation, Mark Thomas and Shawn Sarwar from VaxTrac, and Captain Gregory Michaud from the Forensic Science Division at

Michigan State Police. I am also grateful to Brian Wright, Michigan State University and Matthew Staymates, National Institute of Standards and Technology (NIST) for their assistance with 3D printing fingerprint models, and Anna Song, Michigan State University for her help in cleaning the 3D printed models. I would also like to thank Brian Wright, Chris Traverse and Lars Haubold, Michigan State University for their help in sputter coating various materials on 3D fingerprint targets.

I also want to thank the administrative staff of the Computer Science Department at MSU, including Norma, Linda, Cathy, Debbie, Katy and Courtney for their help with various things such as course registration, conference travel and reimbursements during the course of my study.

I would like to express my sincere gratitude to Dr. Salil Prabhakar for giving me the opportunity to intern at Delta ID and extending all possible help to make my stay comfortable in the bay area. It was a wonderful experience working at Delta ID, particularly with Alex Ivanisov and Dr. Yi Chen.

I owe a lot to my parents and brother for being by my side while I was going through the ups and downs of my journey as a graduate student. Without their moral support, writing this dissertation would not have been possible.

Last but not the least, I would like to mention some special friends I made during my time here in East Lansing. They provided me immense support in different ways to make my stay worthwhile, Tridip Das, Girish Kasat, Shantanu Kelkar, Abhishek Santra, Sabyasachi Halder, Siddhartha Dutta, Shailendra, Rahul Deshpande, Prajakta Deshpande Kulkarni, Maya Patel, Tias Maiti, Rajib Mandal, Shreya Nad, Soumen Ghosh, Chetan Tambe, Oishi Sanyal, Saptarshi Das, Saptarshi Mukherjee, Portia Banerjee, Piku Mandal, Arkaprabha Konar, Preetam Giri, and Aritra Chakroborty. I also thank my friends back home, particularly, Vidushi Chaudhary and Kajal Joneja for keeping me motivated when the chips were down.

TABLE OF CONTENTS

List of Tables

LIST OF FIGURES

Chapter 1

Introduction

"Perhaps the most beautiful and characteristic of all superficial marks are the small furrows with the intervening ridges and their pores that are disposed in a singularly complex yet even order on the under surfaces of the hands and the feet."

- Francis Galton, 1889 [97]

The epidermal ridge patterns found on the palms and fingers of our hands and the soles of our feet (Figure 1.1) have long captivated the imagination of the layman and intrigued scientists and fingerprint experts alike. It is these ridge patterns present on our fingers that are commonly called *fingerprints*. Fingerprints differ from person to person (even identical twins have different prints [141]) and do not change over time. Hence, they are a reliable source for uniquely identifying individuals. From being used in ancient Babylon and China as a proof of identification in business and legal transactions to being deployed in the 21st century for personal identification in large-scale criminal, civilian and governmental applications [141], the utility of fingerprints as a personal identifier has manifested ubiquitously. Advances in both the science and technology of fingerprinting over the last few decades have resulted in widespread applications of fingerprint-based person recognition, including device unlock mechanisms in modern day smartphones [36] and online financial transactions [1] [26] (see Figure 1.7).

(a) (b)

Figure 1.1 Illustrating the friction ridge patterns present on (a) the palms and fingers of our hand and (b) our feet. Images reproduced from [110].

In this chapter, we first describe the fingerprint formation process and highlight the two fundamental properties which purportedly make fingerprints useful for person recognition: uniqueness and permanence. We then enumerate the key milestones in the progression of the use of fingerprints. Subsequently, we describe the design of modern day automated fingerprint identification systems (AFIS), and the existing evaluation methods for these systems. Although the fingerprint research community has made significant advances over the last few decades, there are still certain challenging avenues in fingerprint recognition where further advances are required. We identify and discuss some of these problems in fingerprint recognition. Finally, we conclude the chapter by detailing the contributions of this dissertation in solving two of the aforementioned problems.

1.1 Fingerprint Formation

It is typically presumed that the outer morphology of the friction ridge skin present on our fingers is a direct reflection of its function: to provide appropriate friction for assistance in grasping or holding objects and help in sensing fine texture [139]. The generally believed notion is that friction ridge skin is created from many small localized *ridge units* [57]. These ridge units first appear at 1 or 2 focal points on the fingertip. At approximately 10.5 weeks of gestational age, the ridge

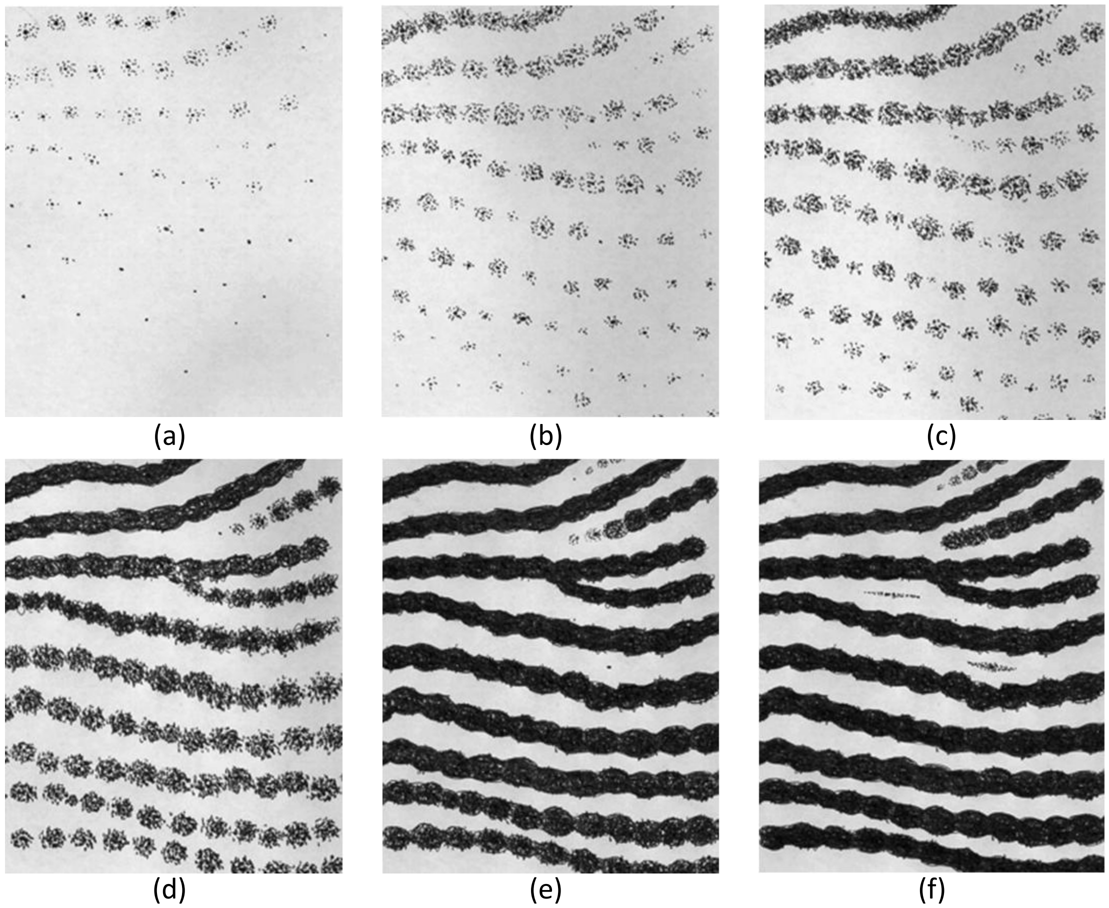

Figure 1.2 Simulation of the fingerprint formation process. (a)-(b) Localized ridge units appear, and (c)-(f) ridge units merge to form ridges with unique characteristics. Image adapted from [110].

units merge together under random forces to form definitive ridge characteristics, such as ridge bifurcations and endings [57] (see Figure 1.2). Due to the random nature of forces acting on the ridge units, these characteristics are believed to be unique. The fingerprint formation process presumably starts deep beneath the skin in the secondary dermal layers, where skin cells are produced and move upwards to the epidermis [71]. In their study on microcirculation of human fingers, Sangiorgi et al. [170] noted that the *"regular disposition of capillaries beneath the dermis sharply followed the fingerprint pattern, reproducing an identical vascular fingerprint with the same individual architecture"*. These observations suggest the permanence of fingerprints; minor cuts and bruises on the fingers do not change fingerprint patterns because new skin cells are generated beneath the epidermis and facilitate the reformulation of fingerprint patterns on the epidermis.

(a) (b) (c)

Figure 1.3 Fingerprints of William Herschel's son at ages (a) 7, (b) 17, and (c) 40 years. Images reproduced from [102].

1.2 Fundamental Tenets: Uniqueness and Permanence

There are two fundamental tenets of fingerprints that underlie their use for recognizing individuals.

1. *Uniqueness:* Fingerprints are able to uniquely identify each individual, i.e., no two fingers, even of the same individual, have identical ridge structure.

2. *Permanence:* Fingerprints do not change over the lifetime of an individual.

To this date, only a few studies have attempted to validate these two tenets. Several of them have attempted to show that every individual fingerprint is unique [164] [193] [174] [173] [174]. It is also believed that individuals sharing the same DNA have different fingerprints. For example, Jain et al. [123] analyzed fingerprints collected from 94 pairs of identical twins and demonstrated that identical twins can be distinguished using fingerprints. However, all of the aforementioned studies are either based on relatively simple statistical models of fingerprint features or based on empirical studies involving only a small number of subjects.

William Herschel was the first to demonstrate the permanence of fingerprints. He captured fingerprints of his son at three different ages 7, 17 and 40 years old and concluded that the ridge details present do not change over time [102]. However, Herschel's conclusions were based on fingerprints collected from just one subject. Recently, Yoon and Jain [189] conducted a formal study involving longitudinal fingerprint records of 15,597 subjects. They used multilevel statistical

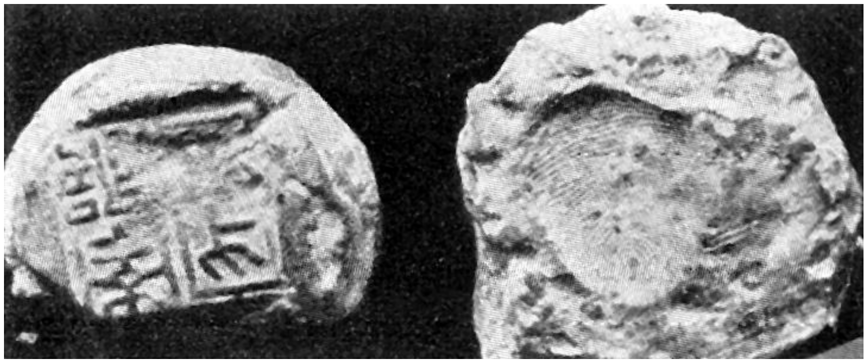

Figure 1.4 Clay seals with fingerprint impressions from ancient China. Image reproduced from [141].

models and a state-of-the-art AFIS to show that fingerprint recognition accuracy of an AFIS does not degrade with time.

In summary, while anecdotally we have been lead to believe that fingerprints exhibit the two essential tenets for person recognition, *uniqueness* and *permanence*, it is not yet supported by sound scientific studies. This was one of the critical issues pointed out by the National Research Council (NRC) in its report on strengthening forensic science in the United States [78]. It is also extensively discussed in the recently released report on ensuring scientific validity of feature-comparison methods by the Presidents Council of Advisors on Science and Technology (PCAST) [45].

1.3 Fingerprint Milestones

The earliest record of the use of friction ridge impressions dates back to 1955-1913 BC when clay tablets with fingerprints were used for conducting business transactions in ancient Babylon [141]. Clay seals with fingerprint impressions that were being used for legal transactions in ancient China between 600-700 AD have also been discovered [141] (see Figure 1.4). A prehistoric picture of a hand with friction ridge patterns was found in Nova Scotia [149]. Historical evidence, clearly, seems to suggest that human fingerprints were used in ancient times as a means for person iden-

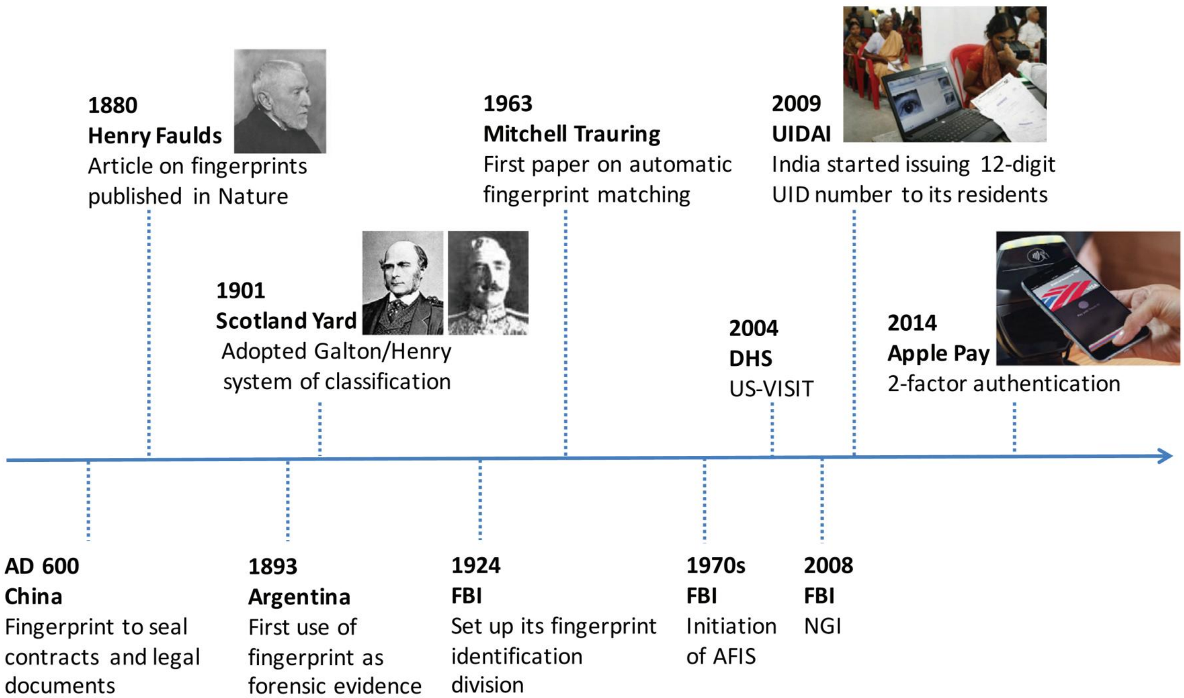

Figure 1.5 Major milestones in fingerprint recognition. Image reproduced from [122].

tification. However, there is no evidence that any systematic methods were being used for person identification using fingerprints.

1.3.1 Major Scientific Studies

Despite the evident use of fingerprints as a "seal" for the purpose of person identification since the ancient era, records of scientific work on fingerprinting are comparatively recent and only began to emerge in the late 19th century. In the year 1858, Sir William Herschel in his capacity as a British administrator in the state of West Bengal in India, made it mandatory to use fingerprints on civil contracts for payroll purposes [98]. In 1880, Henry Faulds first used printer ink to capture fingerprints [90]. In 1892, Francis Galton wrote the landmark book titled *Finger Prints* [96], where he identified features which purportedly make each fingerprint unique, such as ridge endings and bifurcations, and proposed that fingerprints could be used for person identification. In 1899, Edward Henry introduced a fingerprint classification system, which later became popular as the

"Henry System of Classification" [98]. Over 60 years hence, the first scientific paper on automatic comparison of fingerprints by Mitchell Trauring appeared in the journal Nature [179].

1.3.2 Applications in Law Enforcement

In the late 19th century, fingerprints began to be used by law enforcement agencies for establishing the identity of crime suspects. In the year 1893, fingerprints were supposedly used for the first time as an official evidence to convict a mother who had murdered her two children in Argentina [101]. The Scotland Yard started recording fingerprints of criminals around 1900 [76]. Post these developments, the use of fingerprints for identifying and apprehending criminals became widespread. The United States Congress made it mandatory to collect fingerprints of criminals in 1924 [98]. Consequently, the Federal Bureau of Investigation (FBI) established its identification division and began collecting fingerprints of criminals [159].

Manual comparison and maintenance of a large number of prints became increasingly difficult. As a result, there was a compelling need to automate the manual processes. Following this, research and development of Automated Fingerprint Identification Systems (AFIS) was initiated by the FBI in the 1970s [130]. Law enforcement agencies at the state and local level also began installing such systems. In 1999, FBI's Integrated AFIS (IAFIS) started allowing electronic record submissions from state and local law enforcement agencies to the national repository as well as introduced capabilities for these agencies to directly search records in the national repository [130]. The FBI's repository has over 70 million criminal and 34 million civilian sets of tenprints (Figure 1.6) currently on file [91]. In 2011, the FBI introduced the Next Generation Identification (NGI) system with enhanced fingerprint (as well as face, palmprint, and iris) recognition capabilities with reported fingerprint matching accuracy as high as 99.6% [160]. According to their estimates, the introduction of this system has reduced the need for manual reviews by fingerprint examiners by as much as 90% [160]. At present, fingerprints are being used for two main purposes by law enforcement agencies: (i) identifying repeat offenders (tenprint-to-tenprint matching), and (ii) determining who left latent fingerprints or fingermarks at a crime scene [124].

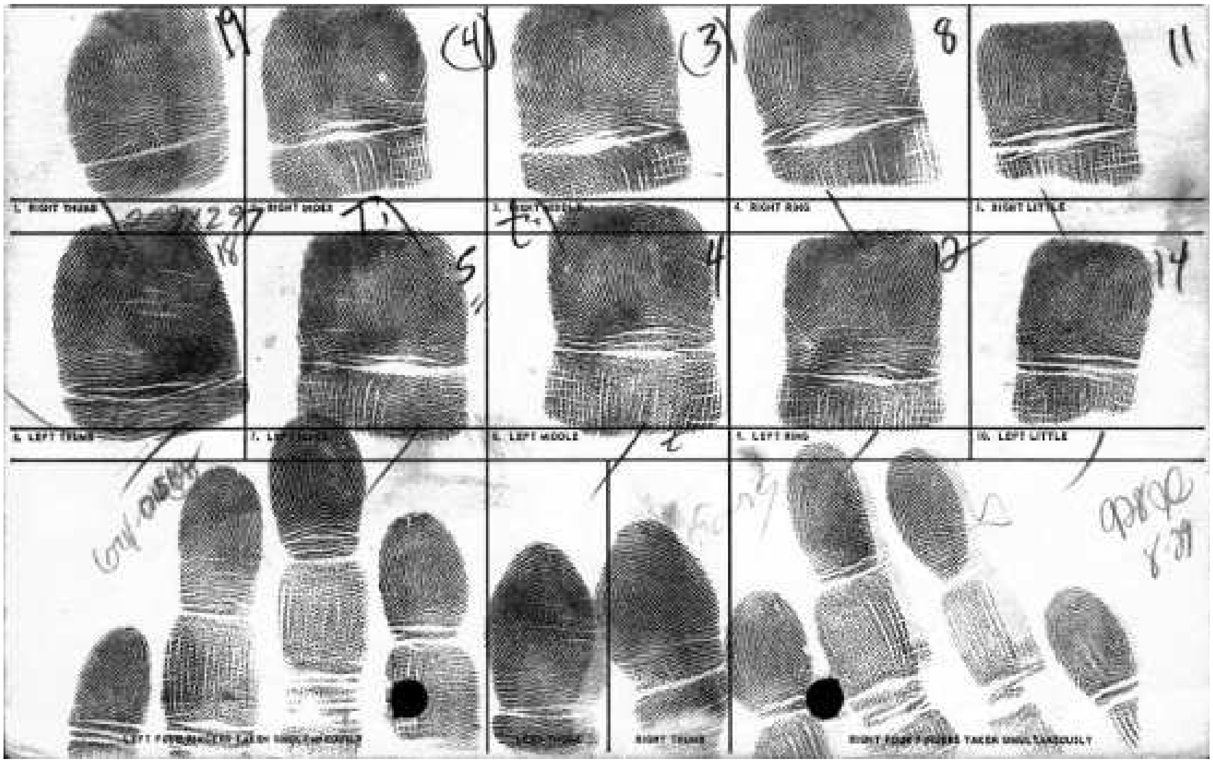

Figure 1.6 Tenprint card used by the FBI for collecting all ten fingerprints. Image reproduced from [189]. The top two rows show the rolled fingerprints, and the bottom row shows the four-finger slap impressions and the plain impressions of the two thumbs.

1.3.3 Other Applications

The last two decades have seen growing use of fingerprints in border control, access control, civil registry and a host of other applications (see Figure 1.7). Examples include the following: (i) India's Aadhaar program initiated by the Unique Identification Authority of India (UIDAI) that aims to assign a unique 12-digit identification number to every resident of India, and has already enrolled over one billion Indian residents [38]. (ii) the system to prevent criminals and immigration violators from crossing the United States border by the Office of Biometric Identity Management Identification Services (formerly the US-VISIT program) [20], (iii) the finger scan system deployed at Walt Disney World Theme Parks since 2005 to help prevent the use of stolen or fraudulent tickets for entering their premises [40], and (iv) fingerprints in mobile devices for authenticating users (e.g. the TouchID system introduced in 2013 in the Apple iPhones [36] and the fingerprint system in

Figure 1.7 Example applications of fingerprint recognition. (a) India’s Aadhar Program [38], (b) Apple Pay [1], (c) U.S. Visit (OBIM) [20], and (d) Access Control.

Samsung phones [25]) and conducting online financial transactions (e.g. Apple Pay [1] introduced in 2014 and Samsung Pay [26] in 2015). Figure 1.5 summarizes the major milestones in fingerprint recognition.

Emergence of important societal applications in the last few years, e.g., vaccination tracking of children, preventing newborn swapping in hospitals and identifying missing children (see Figure 1.8), has ignited the interest of national and international health organizations, as well as non-governmental organizations, in exploring methods to recognize children (age range: 0-5 years) using their physical traits. Compared to other physical traits, fingerprint-based recognition of children appears promising [114] because fingerprints (i) can be captured with relative ease, in contrast to iris, for example, which requires the child to be steady and stare directly into the iris capture device, and (ii) are known to be persistent compared to facial characteristics, for instance, which can change drastically as the child grows. Research efforts are being made to actively explore the use of fingerprints for infant and toddler recognition [114] [112] [113].

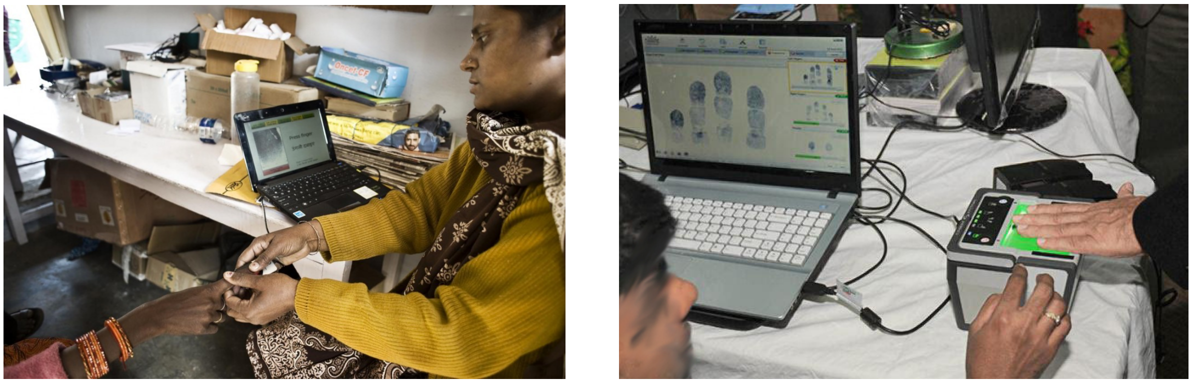

(a) (b)

Figure 1.8 Potential applications requiring biometric recognition of children (age range: 0-5 years). (a) Operation ASHA's mobile healthcare e-compliance biometric system [22], and (b) Aadhaar civil registry project in India [38].

Table 1.1 Qualitative comparison of fingerprints with face and iris.

Trait	**Uniqueness**	**Permanence**	**Ease of Capture**	**Recognition Performance**	**Legacy databases**
Fingerprint	High	High	Medium (obtrusive)	High	Yes
Face	Medium (identical twins)	Medium (facial aging)	High (unobtrusive)	Medium	Yes
Iris	High	High	Low (most obtrusive)	High	No

1.4 Comparison with Other Traits

Fingerprints are arguably the most commonly used physical trait for person recognition. However, besides fingerprints, there are other physical and behavioral traits, e.g, face, iris, voice and gait, that are useful for person recognition [118]. Face and iris, in particular, have been used for person recognition in a variety of applications. Law enforcement agencies, such as the FBI, use face recognition to identify suspects from still photos and videos recorded at crime scenes, and the Department of Motor Vehicles (DMV) in the United States uses face recognition technology to prevent driver's license fraud [120]. India's Aadhaar program [38] uses iris in addition to finger-

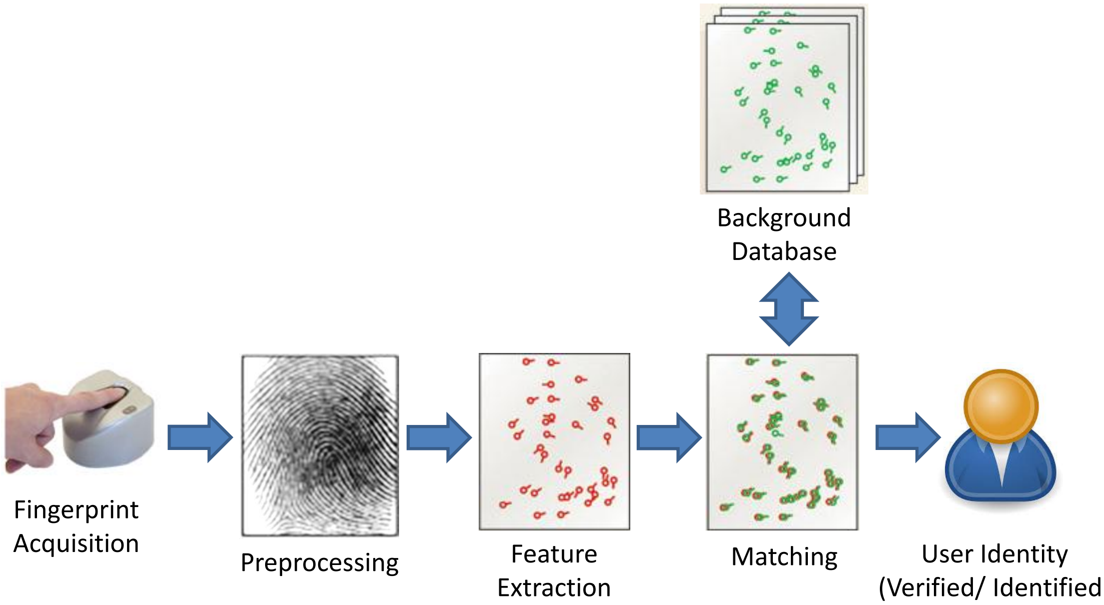

Figure 1.9 Design of a fingerprint recognition system. The major steps involved are: (a) Fingerprint acquisition, (b) preprocessing, (c) feature extraction, (d) comparison of the generated template against the reference database, and (e) depending on the recognition scenario, verification of the claimed identity (1:1 comparison) or establishment of the identity (1:N comparisons). Image adapted from [111].

prints for assigning a unique identity to every Indian resident. Iris recognition is also being used for smartphone unlock and payments [81].

Table 1.1 shows a qualitative comparison of fingerprints with face and iris. Fingerprints are more distinctive and permanent and typically provide a higher recognition performance relative to face. They are easier to capture and have legacy law enforcement databases in contrast to iris. Due to these reasons, fingerprints are often preferred over face and iris in large scale person recognition applications.

1.5 Design of Fingerprint Recognition Systems

With fingerprint recognition being used in a wide variety of applications, fingerprint recognition methods have evolved rapidly over the years. Advancements in both fingerprint sensing technology and fingerprint recognition algorithms have resulted in extremely efficient and accurate Automated Fingerprint Identification Systems (AFIS). Automated fingerprint recognition process consists of the following two stages:

1. *Enrolment:* During enrolment, fingerprint of a user is acquired and salient features are extracted from the resulting image to generate a *fingerprint template*. The template is then stored with the user ID in a database which is generally called the *reference*, *background*, or *enrolment* database.

2. *Recognition:* In the recognition phase, the goal is to either verify the claimed identity of a person (*verification*) or establish the identity of a person (*identification*). In both these scenarios, fingerprint is acquired and features are extracted to generate a template which is often called the *probe* or the *query* template. For verification, the query template is compared to the enrolled templates of the claimed identity (1:1 comparison) in the reference database. On the other hand, for identification where no explicit identity claim is made, the query template is matched against each enrolled template in the reference database (1:N search) to establish the identity.

Below, we explain in detail, the major steps involved in a typical fingerprint recognition system: fingerprint acquisition, feature extraction and matching[1] (see Figure 1.9):

1.5.1 Fingerprint Acquisition

Broadly categorizing, there are two main methods for controlled capture of fingerprint impressions: (i) *off-line* methods using, e.g., ink-on-paper, which acquire fingerprints on a physical media, and (ii) *live-scan* methods, using fingerprint readers which sense fingerprints electronically (see Figure 1.10). Off-line acquisition methods were primarily used by law enforcement agencies to record fingerprints of crime perpetrators. However, in the last few years, live-scan methods have largely

[1] The term *matching* here refers to the comparison of two fingerprint feature sets to ascertain whether they belong to the same or different source finger.

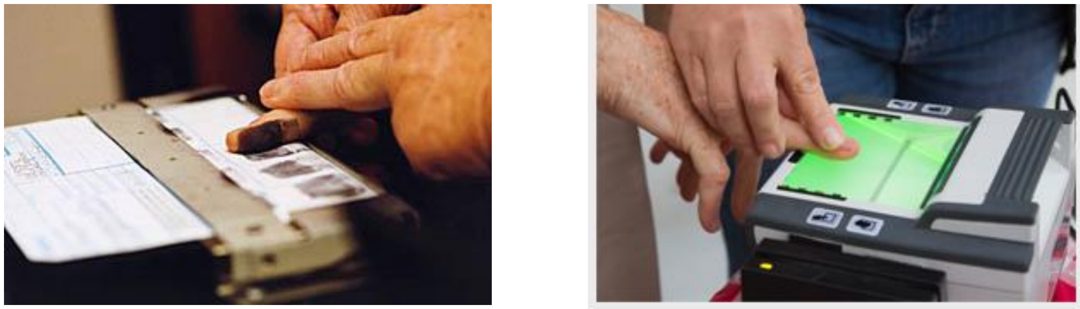

(a) (b)

Figure 1.10 Off-line v. live-scan fingerprint acquisition methods. (a) Traditional ink-on-paper based fingerprint acquisition (off-line) [79], and (b) fingerprint capture using fingerprint reader (live-scan) [142]. For acquiring rolled prints, operator holds the finger of the subject and guides it to "roll" the finger on paper or reader platen.

replaced off-line methods. Live-scan methods are also used in most modern day applications, e.g., civilian, governmental, and access control. Depending on the application scenario, one or more of the following three major fingerprint types are usually acquired, (i) *rolled* impressions, (ii) *plain/slap* impressions, (iii) *latents* (see Figure 1.11). Whereas rolled or slap impressions are acquired in a controlled manner, latent impressions are lifted from surfaces of objects. Rolled and slap prints, stored in the reference database, are often referred to as *exemplar* or *reference* fingerprints.

1. *Rolled*: Rolled impressions are acquired by rolling a finger from "nail-to-nail" on the sensing surface. Expert assistance is generally required for rolling the finger in the correct manner. Rolled impressions capture the complete ridge detail present on a finger from the tip of the finger to the first joint. Therefore, they provide higher recognition accuracies compared to plain impressions. One disadvantage, however, is the presence of greater distortion in rolled impressions than plain impressions due to the acquisition dynamics (pressure, shear, slippage).

2. *Plain/Slap*: Plain/slap impressions are captured by pressing one or more fingers against a flat surface which could either be a paper in case of ink-based acquisition or the platen of a live-scan reader. A single finger capture is termed a *plain* impression (typical in civilian

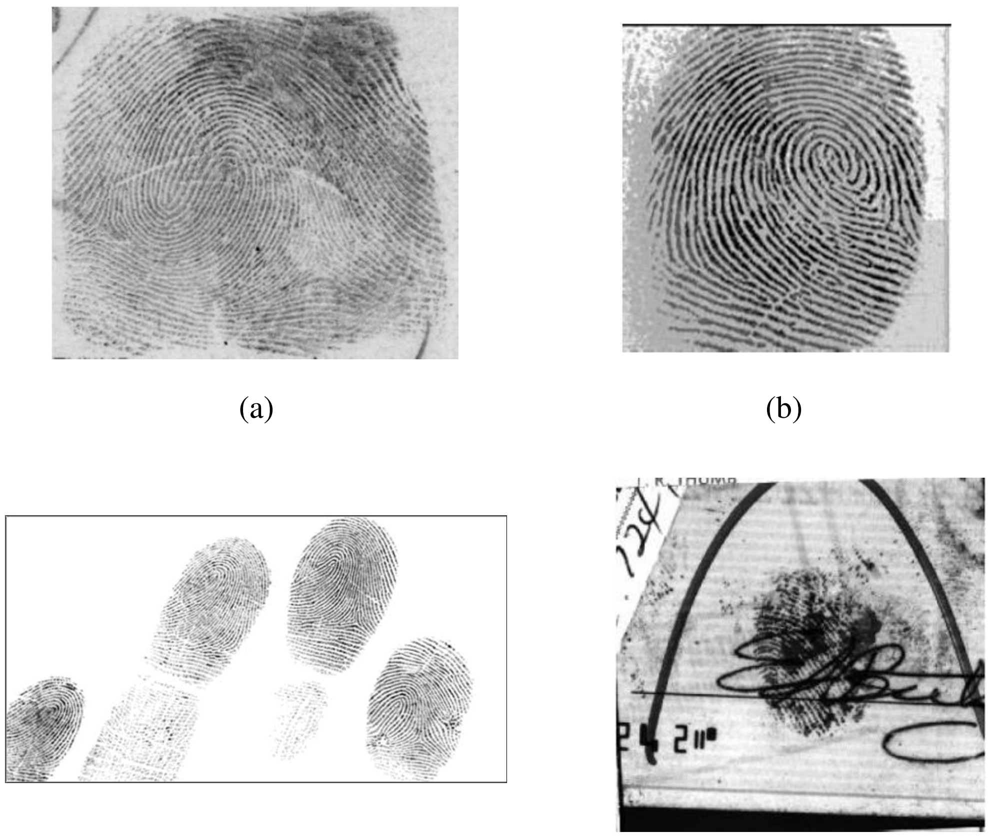

(a) (b) (c) (d)

Figure 1.11 Different types of fingerprint impressions: (a) rolled, (b) plain, (c) slap, and (d) latent.

and access control applications), whereas a four-finger simultaneous capture (index, middle, ring and little fingers altogether) is called a *slap* impression (mostly used in law enforcement applications). Individual plain impressions of the four fingers are segmented out from a slap capture before matching. A popular way of acquiring all ten fingerprints (tenprints) is the 4-4-2 capture where two slap impressions of the four fingers of the left and right hand are captured, followed by simultaneous capture of the two thumbprints.

3. *Latent*: Latent prints, also known as fingermarks, in the forensics community, are the fingerprint impressions inadvertently left behind on the surfaces of objects when they are touched or handled [116]. Latents are poor quality partial impressions with incomplete ridge details impressed against a complex surface background, and can be significantly distorted due to the uncontrolled manner of deposition on the surface. Proper imaging of such impressions is

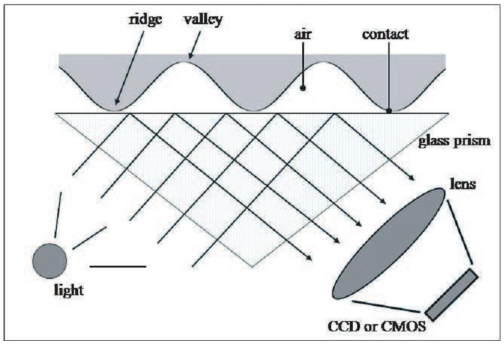

(a)

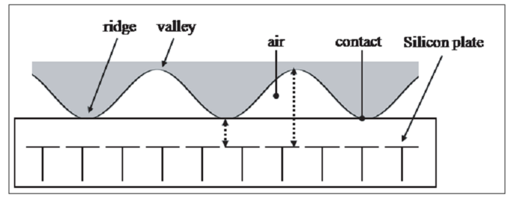

(b)

Figure 1.12 Acquisition principles of optical and solid state sensing technologies. Images reproduced from [50].

very important for law enforcement agencies because they can be a vital evidence to identify crime suspects. Depending on the characteristics of the surface from which latents have to be acquired, forensic experts use physical (e.g. dust with powder), chemical (e.g. ninhydrin treatment), and/or photographical (e.g. ultraviolet imaging) methods for latent acquisition.

1.5.1.1 Fingerprint Sensing Technologies

Ink-on-paper based acquisition methods have been traditionally used by law enforcement agencies to capture plain, slap and/or rolled fingerprints of criminals. However, the spread of fingerprint recognition to many consumer and government applications, has resulted in the development of compact, high resolution and low-cost fingerprint sensing technologies. Some of the popular sensing technologies in use today are described below.

- *Optical*: Fingerprint readers based on optical imaging technology are the most prevalent in the commercial sector. The acquisition principle of most optical readers is based on Frustrated Total Internal Reflection (FTIR) (see Figure 1.12 (a)). The major components in the reader assembly typically are a combination of visible spectrum or infrared LEDs, a glass prism and a CCD or a CMOS sensor array. Fingerprint acquisition involves the following steps: (i) placement of the finger on one face of the glass prism (called the glass

(a)

(b)

(c)

(d)

Figure 1.13 Examples of commercial touchless fingerprint readers. (a) TBS contactless 3D fingerprint reader [32], FlashScan3D's 3D touchless reader [10], (b) IDair's OnePrint [21], and (c) Morpho's Finger on the Fly [17].

platen), (ii) illumination of the finger using LEDs, (iii) absorption of the light incident at the ridges and reflection of the light from the valleys, and (iv) deflection of the reflected light onto the CCD or CMOS array by the glass prism for imaging the fingerprint. Optical readers, in general, provide good fingerprint image quality, and therefore, are the preferred choice over other kinds of readers in most applications. One limitation of optical readers, however, is their bigger form factor compared to, e.g., solid state readers. As a result, so far it has not been easy to embed them into small electronic devices such as mobile phones. On the other hand, almost all the slap fingerprint readers are optical.

- *Solid State*: Solid state readers typically consist of a silicon plate, where each element of the plate is a mini-sensor in itself (see Figure 1.12 (b)). Depending on the type of solid state sensor, fingerprint acquisition is based on one of the following physical characteristics of the finger, (i) capacitance difference between ridges and valleys, (ii) thermal behavior of the friction ridge skin upon contact with the silicon plate, or (iii) pressure variations due to interaction of the finger with the sensing elements. Out of these three, capacitive solid state readers are the most commonly used. Solid state readers generally have a small sensing array, typically 5-8 cm^2, to keep the reader cost low. Because of their low cost and small form factor, they are easy to embed in laptops, PDAs and mobile phones. Fingerprint readers embedded in personal devices, e.g, laptops and smartphones, have a small sensing area which only captures a part of the finger. To capture the entire fingerprint surface area, these readers use two different methods: (i) a swipe of the finger from top to bottom, or (ii) multiple partial captures by aligning the finger in different orientations with respect to the sensing area.

- *Ultrasound*: The ultrasound sensing technology uses ”active” sensing by transmitting acoustic signals of a specific wavelength (e.g., 100 μm) for fingerprint imaging [138]. Ultrasound signals sent to the finger surface are deflected back and captured to form the fingerprint image. This technology is believed to be robust to dirt, oil and other factors which can potentially degrade fingerprint image quality. Yet the commercial application of this technology was, until recently, limited. This was due to ultrasound sensors being bulky and expensive, and fingerprint capture requiring at least a few seconds. However, Qualcomm introduced a major breakthrough with the release of the Snapdragon Sense [46] which is a real time authentication technology for mobile devices based on ultrasound fingerprint sensing.

- *Multi-Spectral*: The multi-spectral fingerprint scanning technology was developed in 2005 by Lumidigm [169], and can be considered as an extension of the optical imaging method described earlier. The main idea in multi-spectral imaging is to illuminate the finger with LEDs of different wavelengths (visible and near infrared). Some of the wavelengths get reflected from the epidermal layer, whereas other wavelengths are reflected by the underlying secondary dermal layers. The response obtained from different wavelengths is combined to produce the final fingerprint image. Because secondary skin layers can be imaged using this method, an advantage of the method is that the resulting fingerprint image is robust to noise due to dirt, sweat, and oil often present on the outer finger skin layer.

- *Touchless*: One major issue with traditional touch-based live scan methods is the inherent distortion induced in the captured fingerprint image when the finger is pressed against the reader platen. To alleviate this issue, touchless live-scan technology was proposed [165]. One of the following two imaging techniques is used in touchless fingerprint readers (see Figure 1.13): *structured lighting* where a fixed light pattern is used to illuminate the finger to estimate the finger depth and generate a 3D representation of the finger, or the *multi-view* imaging technique where multiple cameras are used to image the finger from different viewpoints to construct a 3D fingerprint representation.

To sum up, the last few decades has seen the development and adoption of a variety of live-scan technologies for fingerprint sensing. Easy to use real-time fingerprint acquisition methods have enabled the spread of fingerprint recognition systems to different applications.

1.5.2 Feature Extraction

Fingerprint features are usually categorized into three different levels based on their granularity (see Figure 1.14).

- *Level-1*: Prominent features such as type of the fingerprint pattern (loop, whorl, arch), direction of the ridge flow (*ridge orientation*), discontinuities (singularities) in the ridge flow (cores, deltas), and measurement of the spacing between ridges (*ridge frequency*) are categorized as level-1 features. Note, however, that these features are not unique to each fingerprint.

- *Level-2*: Salient points where a ridge exhibits special characteristics, e.g, endings and bifurcations (also called minutiae), are classified as level-2 features. The recommended scanning

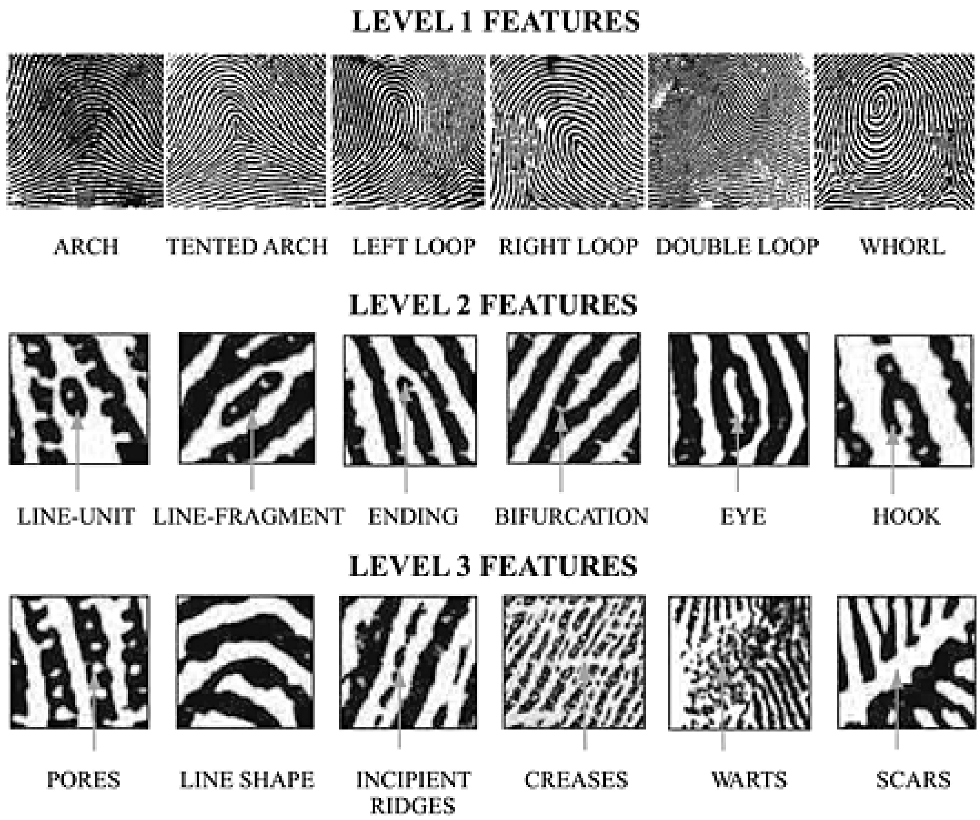

Figure 1.14 The three different levels of fingerprint features. Image reproduced from [115].

resolution to clearly capture level-2 features is 500 ppi. These features are considered to be unique to each fingerprint, and hence, are most commonly used in fingerprint matching.

- *Level-3*: Features at a finer level of granularity such as sweat pores present inside the ridges, dots between the ridges, incipient ridges, and peculiar features such as creases and warts are termed level-3 features. Level-3 features can provide additional distinctiveness, but are only visible in fingerprints acquired at a scanning resolution of 1000 ppi or more. Further, the available algorithms for level-3 feature extraction are not very accurate and robust. However, they appear to be implicitly used by forensic examiners for "exclusion"[2].

Law enforcement agencies generally acquire fingerprints at a scanning resolution of 500 ppi, although, the 1000 ppi resolution is being considered for adoption. State-of-the-art feature extraction algorithms typically extract only level-1 and level-2 features (e.g., ridge orientation, ridge

[2]Exclusion refers to excluding the possibility of match when manually comparing two fingerprints.

frequency, and minutiae) and their derivatives. The derived meta-features from level-1 or level-2 features are also called *descriptors*. Most popular ones are (i) ridge orientation descriptors based on orientation values in the minutiae neighborhood (e.g. [178]) and (ii) neighborhood minutiae based descriptors (e.g. [68]).

All fingerprint images undergo a preprocessing step (foreground extraction and enhancement) prior to fingerprint extraction. This step is particularly crucial, in case of latent fingerprints, where image quality is a major issue. Techniques developed in machine learning and computer vision such as dictionary learning [66] and convolutional neural networks [64] have been proposed for this purpose. State-of-the-art commercial feature extraction algorithms designed specifically for latents are believed to extract multiple feature representations (e.g. at different scales) from a latent with the goal of improving the overall matching accuracy.

1.5.3 Fingerprint Matching

There are two different matching scenarios typically encountered in most fingerprint recognition applications: (i) matching rolled/plain (exemplar) prints to exemplars, and (ii) matching latent to exemplar prints.

1.5.3.1 Exemplar-to-Exemplar matching

This is the most commonly encountered scenario in applications ranging from mobile phone unlock and border control to criminal background check and national registry. For example, in national identification systems such as Aadhaar [38], exemplar-to-exemplar (tenprint) matching is used for "de-duplicating identities" i.e. to prevent enrolment of duplicate identities. Exemplar (rolled/plain) fingerprints are, in general, good quality prints with clear ridge detail. This allows accurate and robust feature extraction from exemplar prints. Minutiae are the most commonly used features in exemplar fingerprint matching. Matching minutiae sets extracted from two different fingerprints is a classic application of the point pattern matching problem [140]. As an example, one simple approach for matching two different minutiae sets is to generate an initial set of correspondences

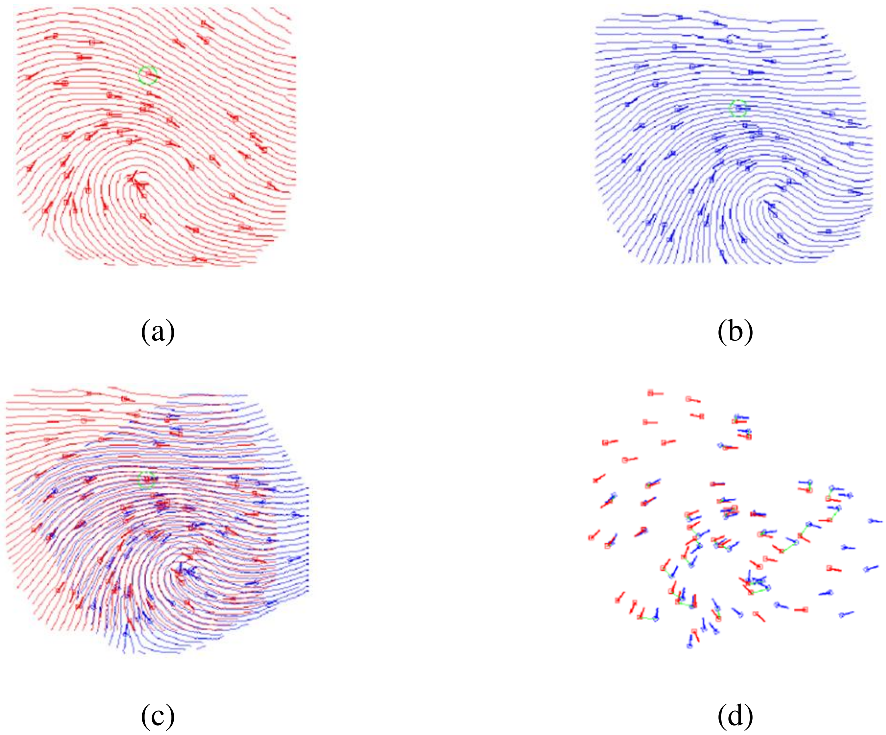

Figure 1.15 A simple method for minutiae matching. (a) and (b) The enrolled and probe fingerprint templates marked with minutiae sets, (c) alignment of the two templates based on an initial corresponding minutiae pair marked in green, and (d) corresponding minutiae points generated based on the alignment in (c). Image reproduced from [119].

between the two minutiae sets, and then iteratively (i) generate alignment hypothesis based on the current set of corresponding minutiae pairs (measure of similarity between the minutiae sets), and (ii) update minutiae correspondences based on the current alignment hypothesis [125] (Figure 1.15). Descriptor-based fingerprint matching methods [178] [68], on the other hand, establish minutiae correspondence either in a (i) top-down manner by generating minutiae correspondences from high similarity descriptor pairs and then eliminating false correspondences using local structural constraints, or (ii) bottom-up manner where typically, the top n (e.g., $n = 5$) highest similarity descriptor pairs are used; each of the n descriptor pairs is used to establish minutiae correspondences by aligning the fingerprint pair or growing the corresponding region, and the pairing that results in the maximum number of minutiae correspondences is selected as the final result.

The goal of fingerprint matching is to compute the similarity between the two fingerprint impressions. Once minutiae correspondences between the two fingerprints are generated, similarity is computed based on the number as well as the strength of these correspondences. Proprietary fingerprint matching algorithms commonly use additional features, e.g., ridge flow and ridge spacing, besides minutiae.

1.5.3.2 Latent-to-Exemplar matching

For law enforcement agencies and forensic crime labs, matching latent prints lifted from crime locations to exemplar prints in legacy law enforcement databases is important to establish possible crime suspects. Latent images typically have incomplete ridge detail and possibly severe background noise leading to difficulty in automatic extraction of reliable features for matching. In the absence of robust automatic matching methods, a semi-automatic matching method based on the *Analysis*, *Comparison*, *Evaluation* and *Verification* (ACE-V) protocol [57] is practised in most crime labs. Under the purview of this protocol, a fingerprint examiner determines the quality of the latent, and if the latent has sufficient quality, marks features, such as region of interest and minutiae on the latent image. The latent with marked features is then submitted to a latent matcher for comparing the latent to exemplars in the reference database. A candidate list of top-K matching exemplars from the reference database is returned by the latent matcher[3]. The examiner then compares the latent to each exemplar image in the candidate list to determine the corresponding features. Based on the strength of the correspondences obtained for different latent-exemplar pairs, the evaluation of whether a candidate exemplar mates with the latent (hit is found) is made. Following this, a second fingerprint examiner then independently inspects the latent-exemplar pairs and verifies the authenticity of the decision made by the first examiner.

[3]State-of-the-art latent matchers match multiple feature representations and fuse the results to improve the likelihood of obtaining a hit in the candidate list.

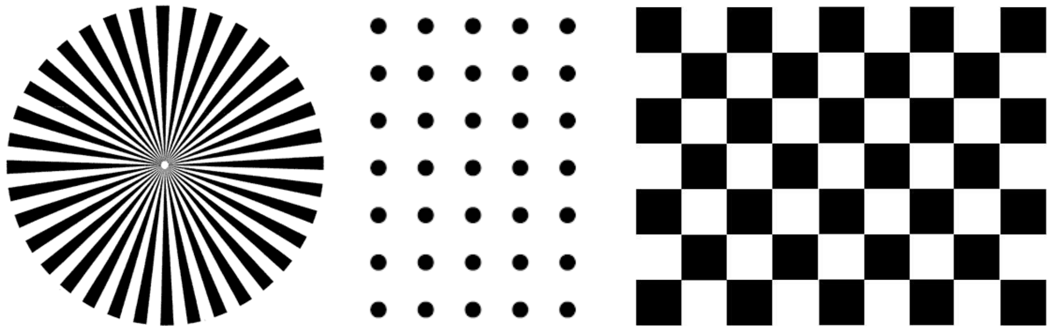

Figure 1.16 Example targets used for calibrating imaging systems. Images adapted from [107] [137] [163].

1.6 Evaluation of Fingerprint Recognition Systems

Performance evaluation is a critical step during the design and development of a fingerprint recognition system before its actual deployment. For system evaluation, a two-step evaluation procedure is usually followed: internal testing to ensure desired accuracy, followed by field testing to validate the laboratory testing results in field operations. Before deployment, each module of the fingerprint system (sensing, feature extraction and matching) needs to be thoroughly evaluated. In the following sections, we briefly describe the standard testing procedures for certification of fingerprint readers, as well as the evaluation studies conducted to benchmark existing feature extraction and matching algorithms.

1.6.1 Sensing Technology Certification

In the United States, fingerprint readers are certified by the Technology Evaluation Standards Test Unit, part of the FBIs Biometric Center of Excellence (BCOE) led by the Criminal Justice Information (CJI) Services Division [9]. Two different standards have been established by the FBI for the certification of fingerprint readers. The *PIV* standard [155] caters to single-finger readers designed for the verification scenario. Fingerprint readers built for use in applications involving large-scale identification are certified under the *Appendix F* standard [156] which enforces stricter fingerprint quality requirements compared to the *PIV* standard. These standards contain the desired reader specifications for different aspects of the reader, such as geometric accuracy, resolution and spatial frequency response. The fingerprint reader certification process requires fingerprint vendors to show that images captured by their readers exceed the minimum specifications prescribed in the relevant standard [8]. As a first step, fingerprint vendors internally test their readers using calibration targets (see, e.g., Figure 1.16) to ensure that the target images captured using the reader are of sufficient quality to meet the prescribed specifications in the standard. Once they are satisfied with the captured image quality, they submit test images to the certification agency. The agency independently verifies that the test images meet the standard specifications and certifies the reader under the relevant standard.

The testing and certification of biometric devices (fingerprints, iris and face) for use by the Unique Identification Authority of India (UIDAI) in the Aadhaar project is performed by the Standardization Testing and Quality Certification (STQC) Directorate, Government of India [37]. UIDAI is one of the largest consumers of biometric readers in the world with 36,000 enrolment stations deploying 11 different certified biometric readers (5 fingerprint slap sensors, 4 iris sensors, and 2 face cameras) [80]. Image acquisition requirements equivalent to the *Appendix F* standard are mandated for fingerprint readers used for enrolment in Aadhaar [42]. For getting their readers certified, fingerprint vendors submit a certification agreement to the certification agency, the STQC Directorate. The certification agency evaluates the evidence of conformity of the submitted agreement to the certification procedure guidelines. Thereafter, provided that the testing procedure results are satisfactory, the fingerprint reader is certified by the agency for use in Aadhaar [43].

1.6.2 Feature Extraction and Matching Evaluation

Fingerprint feature extraction and matching algorithms are typically evaluated together as a single component where fingerprint images are fed as input and similarity scores are generated as output. Different measures are used to evaluate their performance in the two matching scenarios commonly encountered, verification (1:1 comparison) and identification (1:N comparison).

To evaluate fingerprint verification performance, two different metrics are frequently used, (i) *true accept rate (TAR)*, i.e. proportion of subjects, amongst those previously enrolled, that can be successfully verified, and (ii) *false accept rate (FAR)*, i.e. proportion of subjects, amongst those not previously enrolled, that are incorrectly determined to have been previously enrolled [141]. These two quantities, TAR and FAR, are not independent of each other, so there is a trade-off between TAR and FAR. Receiver Operating Characteristic (ROC) curve, a plot of TAR v. FAR at different operating thresholds, is often used to indicate the verification performance. Some studies prefer to use the *false Reject Rate (FRR)* instead of TAR. FRR indicates the proportion of subjects, amongst those previously enrolled, that cannot be successfully verified. In this case, a Detection Error Trade-off (DET) curve that plots FRR v. FAR is used to report verification performance.

There are two distinct types of identification scenarios: (i) *closed set* where the probe or the query is known to have a mate in the reference database, and (ii) *open set* where the probe may or may not have a mate in the reference database. For closed set identification, typically, a candidate list of the top-K matches is retrieved, and the retrieval rank of the true mate in the candidate list is used as an evaluation metric [141]. Cumulative Match Characteristics (CMC) curve, where each point on the curve denotes whether the true mate was retrieved at rank $\leq i$ in the candidate list, is plotted to indicate the closed set identification performance. In case of open set identification, the two most commonly used performance evaluation metrics are: *false positive identification rate* (FPIR) which measures the proportion of queries which do not have a mate in the reference database but were falsely identified to have a mate, and false negative identification rate (FNIR) which measures the proportion of queries which have a mate in the reference database, but could not be successfully identified to have a mate.

Since the early 2000s, NIST has conducted several evaluations of fingerprint feature extraction and matching algorithms. The FpVTE 2003 evaluation [185], performed on a database of 10,000 plain fingerprints, found that the best performing algorithm had a TAR of 99.4% at FAR of 0.01%. In the most recent evaluation FpVTE 2012 [184], plain fingerprints of 30,000 subjects (10,000 mates and 20,000 non-mates) were searched against plain fingerprints of 100,000 subjects and the

FNIR of the best performing algorithm, at FPIR of 0.1%, was reported to be 1.9% for single index finger captures and 0.27% for two index fingers.

To evaluate the state-of-the-art latent matching algorithms, NIST performed ELFT-EFS evaluation in two phases [109] [108]. In Phase I, 1,114 latents were matched against exemplars (rolled + plain) obtained from 100,000 subjects. The rank-1 identification accuracy of the best algorithm was reported to be 62.2%. In Phase II, 1,066 latents were compared against reference database of exemplars of 100,000 subjects, and the rank-1 identification accuracy of the best performing method was 67.2%.

1.7 Challenges in Fingerprint Recognition

Although the design of automatic fingerprint recognition systems and the methods to evaluate these systems have evolved over the past 50 years, there remain a number of open research issues and challenges. We provide this list of problems from our perspective and then address two of them that constitute the contributions of this dissertation.

1.7.1 Open Research Issues and Challenges

1.7.1.1 Automatic latent fingerprint matching

Latent fingerprints are important for law enforcement agencies and forensic crime labs to identify fugitives and to assess if they are guilty or innocent. However, despite recent developments, fully automatic and accurate matching of latents to reference fingerprints remains an open challenge for fingerprint researchers.

1.7.1.2 Interoperability of fingerprint readers

Large-scale fingerprint system deployments e.g., Aadhaar [38] have multiple enrolment stations equipped with different fingerprint readers. Compatibility of fingerprints acquired by the different

Figure 1.17 Example procedure to create an artificial fingerprint directly from a live finger. Plastic is used to create the mold and gelatin is used as the casting material. Image reproduced from [143].

readers is essential for successful operation of such a large-scale system. Furthermore, with the advent of new sensing technologies, such as contact-less 3D fingerprint sensing [165], it is important to develop methods to match fingerprints acquired by these readers with reference prints in legacy databases.

1.7.1.3 Operational evaluation of fingerprint systems

Evaluation standards have been developed for certification of fingerprint readers. However, test results obtained in a controlled environment do not generalize to the operational settings. There is a need to develop methods for evaluating fingerprint readers in the functional environment. Furthermore, there is a lack of standard procedures for end-to-end evaluation of fingerprint systems, from fingerprint acquisition to feature extraction and matching.

1.7.1.4 Fingerprint liveness detection

Fingerprint readers embedded in consumer devices, e.g., mobile phones and tablets, and that are being used for conducting financial transactions, have been shown to be vulnerable to spoof attacks [144] [145] [65] [143]. Figure 1.17 illustrates a simple procedure to create an artificial finger

(a) (b)

Figure 1.18 Examples of non-ideal fingerprint images. (a) A fingerprint with worn-out ridge details, and (b) a fingerprint with altered patterns (image reproduced from [188]).

directly from a live finger that can be used for spoofing fingerprint readers. Several fingerprint anti-spoofing algorithms have been developed by academic researchers [47] [95] [99]. However, there is a need to develop commercial-grade liveness detection methods to prevent impostors from misusing fingerprint recognition technology.

1.7.1.5 Fingerprint template security

In most operational fingerprint systems, fingerprint templates are typically secured by using standard encryption techniques, e.g., AES. The security of the template, therefore, depends on the lack of adversary's knowledge about the decryption key. Further, template matching is usually not performed in the encrypted domain. As a result, templates are decrypted at the time of authentication, and this leaves them vulnerable to possible attacks during authentication [154]. To overcome this limitation, one common approach is to store the encrypted templates and decryption keys in a secure module (e.g., A10 chip on Apple iPhone7[4]) and perform template matching in a trustworthy environment. However, this requires the user to carry an additional device that stores the encrypted templates. Although numerous fingerprint template protection techniques that aim to

[4]http://support.apple.com/en-sg/HT5949

ensure non-invertibility, revocability and non-linkability of templates while maintaining the recognition performance have been proposed over the years (e.g. [182], [153], [152], [126]), there is still a wide gap between the theoretical claims and the practical applicability of these methods [154].

1.7.1.6 Matching non-ideal fingerprint images

It has been observed that fingerprints of older people and those in certain professions, e.g., farming and welding, are of poor quality [172] [183]. This is because with repeated use of fingers or because of the fingers coming in contact with certain chemicals, ridges present on their fingers wear out over time (see Figure 1.18 (a)). Some people have genetically poor quality fingerprints. Besides, there have been cases where criminals and those guilty of other significant felonies have intentionally obliterated or altered their fingerprints to evade identification by the authorities [188] (see Figure 1.18 (b)). Matching these non-ideal prints is a challenging task.

1.7.2 Automatic Latent Fingerprint Matching

In its 2009 report on strengthening forensic science in the United States [78], the National Research Council emphasized the need to address the following two major issues facing forensic science: (i) "lack of mandatory and enforceable standards" for ready reference by crime labs around the world and (ii) "unacceptable case backlogs in state and local crime labs which likely make it difficult for laboratories to provide strong evidence for prosecutions and avoid errors that could lead to imperfect justice". Following this, efforts were made to understand in depth the different factors which impact the latent fingerprint examination workflow and to standardize the processes [44].

As an example, to improve the odds of obtaining a match, a common practice used by several law enforcement and forensic agencies is to involve a fingerprint examiner to (i) mark features on a latent image before submitting it to an AFIS, and (ii) inspect the list of top-K candidates returned by the AFIS to verify that a hit has been made. Although this manual intervention process is supposed to be beneficial for increasing the overall matching accuracy, studies on human factors have shown that it induces bias and subjectivity in the latent matching process [85] [86]. Further, it has also been demonstrated that examiners often have a low degree of agreement with their own decisions, as well as the decisions made by other examiners, reducing the repeatability of the identification outcome [181]. Another impending issue is the objective determination of the evidential value of a latent print [75].

The 2016 report by the Presidents Council of Advisors on Science and Technology (PCAST) [45] states that “latent fingerprint analysis is a foundationally valid subjective methodology albeit with a false positive rate that is substantial and is likely to be higher than expected by many jurors based on longstanding claims about the infallibility of fingerprint analysis” and that “in reporting results of latent fingerprint examination, it is important to state the false positive rates based on properly designed validation studies”. This necessitates the need for fully automatic latent matching to eliminate human bias and subjectivity.

The evaluation of latent matching technologies (ELFT-EFS II [108]) conducted by the National Institute of Standards and Technology (NIST) in 2012, reported the identification accuracy of the best automatic latent matching algorithm to be mere 67.2%. In contrast, the results of the fingerprint vendor technology evaluation performed by NIST in 2012 [184] reported identification accuracy numbers as high as 99% for automatic matching of rolled/plain impressions. This indicates that in spite of developments in fingerprint recognition technology during the past 40 years, improvements to the automatic latent print matching procedure are urgently needed.

For this reason, we pursued this problem in this dissertation. We developed a top-down matching paradigm that takes feedback from reference prints and re-sorts the candidate list generated by a bottom-up latent matcher to improve its accuracy. We also developed a latent markup crowdsourcing framework where fingerprint examiners and the latent matcher work in conjunction with each other to boost the latent matching accuracy.

1.7.3 Operational Evaluation of Fingerprint Systems

In deploying a large-scale fingerprint recognition system, one of the critical factors is to have a reasonable estimate of the matching performance of the system in the operational settings. For

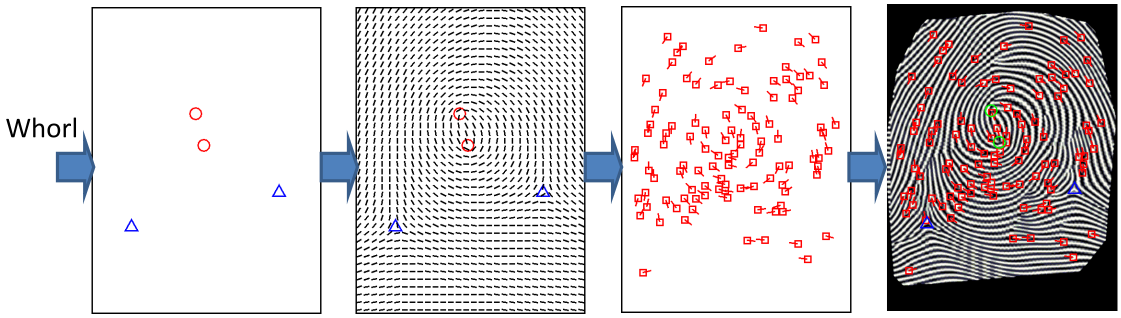

Figure 1.19 2D synthetic fingerprint generation process using the method in [192]. (a) Fingerprint type is specified, (b) ridge flow map is generated from a learned statistical model, (c) minutiae are generated based on the ridge flow in (b) and a learned statistical minutiae model, an (d) 2D synthetic fingerprint is synthesized using (b) and (c).

this purpose, typically, pilot studies are first conducted on a large number of fingerprints of many subjects to ascertain the operational thresholds on comparison scores to achieve the desired false accept rate (FAR). This is a tedious process both in terms of time and resource commitment. Besides, the resulting performance estimate is limited in the confidence of its accuracy by the amount and nature of data which is available. One possible solution to alleviate this shortcoming of small sample size is to synthetically generate very large amounts of realistic looking fingerprint images which can then be used for system performance evaluation. This would entail generating, say, millions of synthetic fingerprints for evaluating large-scale fingerprint recognition systems [69] [192].

State-of-the-art fingerprint generation methods [67] [192] output 2D synthetic fingerprints using mathematical or statistical models of fingerprint features (e.g. fingerprint type, orientation field and minutiae). The 2D synthetic fingerprint generator proposed in [67] generates ridge flow map using a mathematical model and ridge density map based on heuristics learned from several fingerprint images. Directional filters tuned to local ridge orientation and frequency values are then iteratively applied starting from a few seed locations to generate fingerprint ridge patterns. Note, however, that minutiae placement cannot be controlled during the 2D synthetic fingerprint

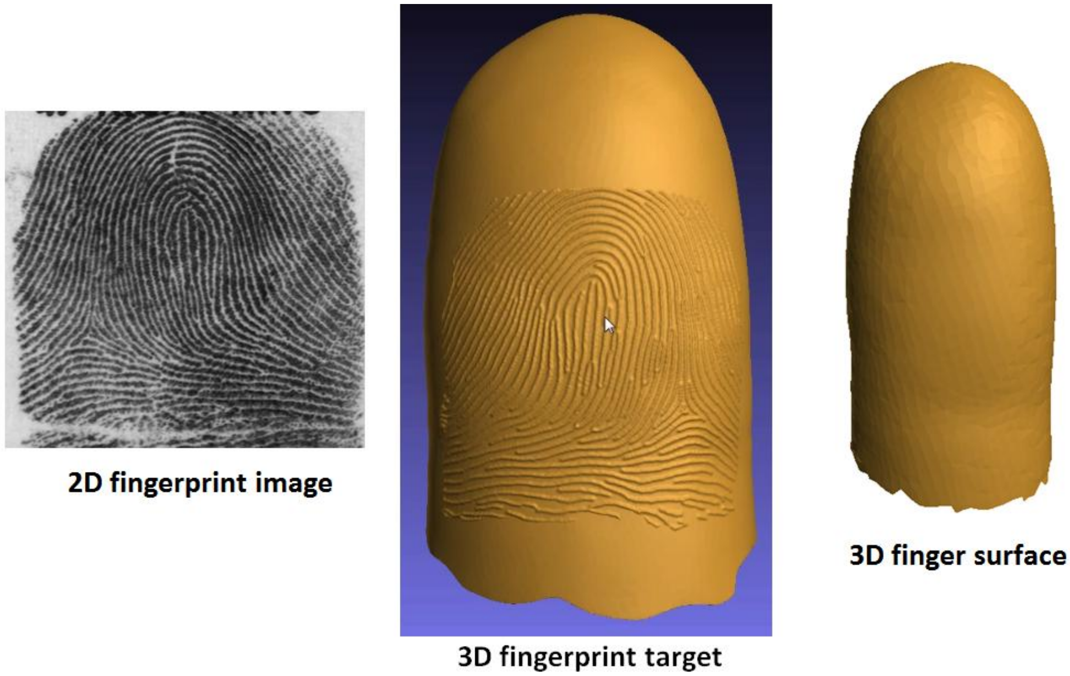

Figure 1.20 Example of a generated 3D fingerprint target. Shown on the left is the 2D fingerprint image and on the right is the 3D finger surface used to create the 3D fingerprint target.

generation process. On the other hand, the 2D synthetic fingerprint generation method in [192] outputs 2D synthetic fingerprints using statistical models of fingerprint features (fingerprint type, orientation field and minutiae). The features are first sampled from their respective statistical distributions, followed by a fingerprint reconstruction method (described in [92]) to generate visually realistic synthetic fingerprints (see Figure 1.19).

The aforementioned methods can generate synthetic fingerprints to evaluate fingerprint feature extraction and matching. However, there is a lack of an approach to evaluate fingerprint readers in operational settings (e.g. placement of human finger on the reader platen) , and consequently an "end-to-end" fingerprint biometric system, from sensing a physical finger and acquiring its impression (image) to extracting the template and establishing or verifying an identity. Operational evaluation of fingerprint systems, therefore, still remains a challenge.

To address the aforementioned limitations, we generated single-finger 3D fingerprint targets (see Figure 1.20). We projected 2D calibration patterns with known features (e.g. sine gratings of known orientation and frequency, 2D fingerprints with known singularities and minutiae) onto

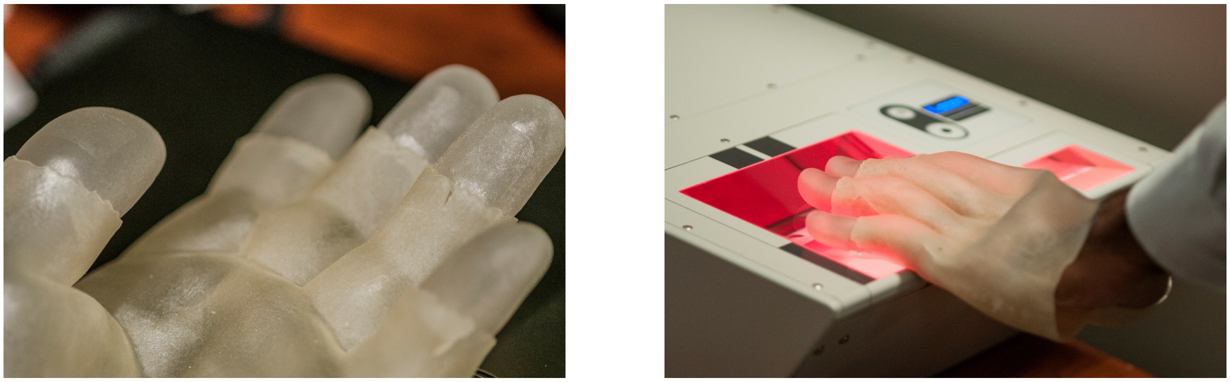

(a) (b)

Figure 1.21 Sample 3D printed whole hand target (a), and (b) evaluating a slap fingerprint reader using the 3D whole hand target shown in (a).

a 3D finger surface to create electronic 3D fingerprint targets. We then used a state-of-the-art 3D printer to fabricate these targets with materials having similar hardness and elasticity to the human skin. We showed the utility of 3D targets in evaluating three different single-finger 500/1000 ppi optical fingerprint readers.

For evaluating contact-based and contactless slap fingerprint readers, we created 3D whole hand targets complete with all four fingerprints and the thumbprint (see Figure 1.21). Given an electronic 3D hand model, 3D finger surfaces corresponding to each of the fingers and the middle portion of the hand were first segmented. 2D calibration patterns were then projected and etched on the segmented 3D finger surfaces. Following this, wearable electronic 3D targets for all fingers and the thumb as well as fingerless glove were fabricated with a state-of-the-art 3D printer. The generated 3D whole hand targets were used for evaluating three different 500/1000 ppi contact-based slap readers and a 500 ppi contactless slap reader.

The 3D targets fabricated with the 3D printer, although similar in hardness and elasticity to the human skin, were non-conductive. Consequently, they could not be used for evaluating capacitive fingerprint readers such as those embedded in modern day smartphones. To impart conductivity to 3D printed targets, we coated their surface with thin layers of conductive materials (titanium + gold) via DC sputtering (see, e.g, Figure 1.22). The generated conductive targets were used for evaluating a 500 ppi capacitive fingerprint reader. It is important to note that besides fingerprint

(a) (b)

Figure 1.22 Sample conductive 3D target (goldfinger) created by depositing thin layers of titanium and gold on 3D printed single-finger targets shown in (a), and (b) an impression of the goldfinger in (a) captured using a capacitive reader.

reader evaluation, our targets can also be used for end-to-end evaluation of fingerprint recognition systems.

1.8 Dissertation Contributions

The contributions (including the organization) of this dissertation are as follows:

- Design of a framework to improve latent matching accuracy by incorporating top-down information or feedback from an exemplar print to refine the features extracted from a latent (Chapter 2). The refined set of latent features (e.g. ridge orientation and frequency), after feedback, are compared again to the top-K candidate exemplars returned by the baseline matcher and to generate a new ranked candidate list. Our contributions are: we (i) devise systemic ways to use information in exemplars for latent feature refinement, (ii) develop a feedback paradigm which can be wrapped around any latent matcher for improving its matching performance, and (iii) determine when feedback is actually necessary to improve latent matching accuracy.

- Design of a crowd powered latent matching framework where multiple latent examiners and an automatic latent matcher work in a synergistic manner to boost the overall identification accuracy (Chapter 3). Given a latent, the candidate list output by the latent matcher is used to determine the likelihood of a hit at rank-1. A latent for which this likelihood is low is crowdsourced to a pool of latent examiners for additional feature markup. The manual markups are then input to the automatic latent matcher to increase the likelihood of finding a hit in the reference database. Furthermore, a greedy paradigm where markups are obtained from the examiners in an incremental manner when required, is also proposed. This is shown to reduce the examiner workload by only requiring a maximum of three examiners to provide markup for a latent.

- Design and fabrication of 3D fingerprint targets for repeatable behavioral evaluation of single-finger optical readers (Chapter 4). 2D calibration patterns with known characteristics (e.g. sinusoidal gratings of pre-specified orientation and frequency, fingerprints with known singular points and minutiae) are projected onto a generic 3D finger surface to create electronic 3D targets. A state-of-the-art 3D printer is used to fabricate wearable 3D targets with material similar in hardness and elasticity to the human finger skin. The generated 3D targets are suitable for behavioral evaluation of three different (500/1000 ppi) PIV/Appendix F certified single-finger optical readers.

- Generation of 3D whole hand targets complete with four fingerprints, the thumbprint and the middle portion of the hand for repeatable evaluation of slap and contactless fingerprint readers (Chapter 5). 2D calibration patterns with known characteristics are projected onto 3D finger surfaces corresponding to each of the four fingers and the thumb to create electronic whole hand 3D target. Physical 3D whole hand targets are subsequently fabricated using a state-of-the-art 3D printer with materials that are similar in hardness and elasticity to the human skin as well as optically compatible with a variety of optical fingerprint readers.

Generated whole hand 3D targets are used for evaluating three Appendix F certified contact-based slap readers and a PIV certified contactless slap reader.

- Fabrication of conductive 3D targets for evaluation of capacitive fingerprint readers (Chapter 6). 3D printed targets are coated with thin layers of conductive materials (titanium + gold) via DC sputtering to impart conductivity to their surface. We show that the coating procedure does not impact the fidelity of the calibration patterns etched on the 3D targets. The conductive 3D targets are used for evaluating a PIV certified single-finger capacitive reader. Furthermore, a simple procedure to create 3D spoofs for performing presentation attacks on capacitive readers is described. The generated 3D spoofs are successfully used for spoofing the single-finger capacitive reader and an embedded reader in an access control terminal.

- A brief summary of the contributions of this dissertation and possible future research directions are discussed in Chapter 7.

Chapter 2

Latent Fingerprint Matching: Performance Gain via Feedback from Exemplar Prints

2.1 Introduction

Latent fingerprints[1] are partial impressions of the finger with relatively smaller area containing friction ridge patterns. Automatic matching of latent fingerprints to exemplars is significantly challenging because latents (i) generally exhibit poor quality in terms of ridge clarity, (ii) have complex background noise (Figure 2.1), and (iii) have large non-linear distortions due to variations in finger pressure when an object is touched, resulting in the deposition of latent print on its surface. In the Evaluation of Latent Fingerprint Technologies (ELFT) [109] conducted by NIST, the Phase-I results showed that the best rank-1 latent matching accuracy was 80% in identifying 100 latent images from amongst a set of 10,000 rolled prints [157]. More recently, in the NIST Evaluation of Latent Fingerprint Technologies: Extended Feature Sets (ELFT EFS) Phase II [108], the rank-1 identification accuracy of the best performing latent matcher was only 67.2% in the "lights-out" (fully automatic) identification mode [2]. So, while Automated Fingerprint Identification Systems

[1] The term *fingermark* is also used in the forensic science community to refer to the finger impressions accidentally left behind on the surface of objects. We use the term *latent* because it is more popular in the biometrics community.

[2] The latent matching accuracy is significantly higher in the ELFT Phase-I as compared to Phase-II because the quality of latents used in Phase-I evaluation was comparatively better.

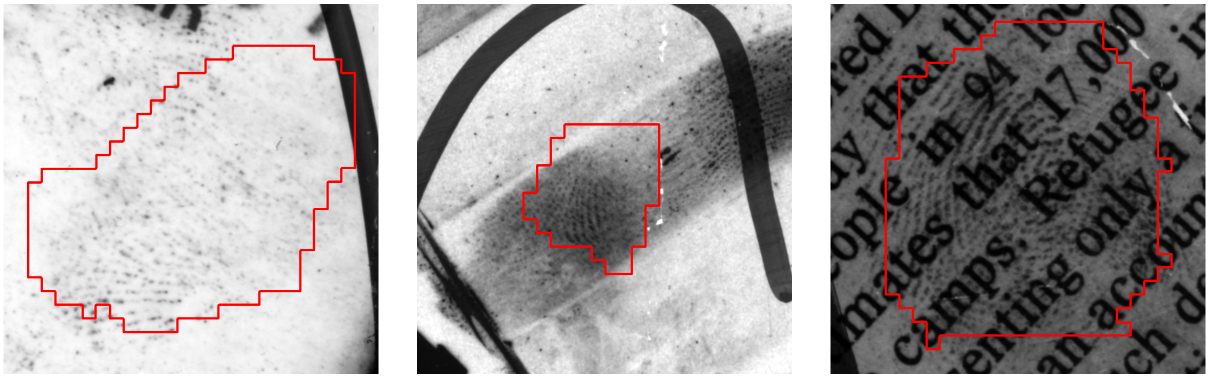

(a) (b) (c)

Figure 2.1 Sample images from the NIST SD27 database shown here to elucidate some of the challenges in latent fingerprint matching: (a) poor ridge clarity, (b) insufficient amount of usable ridge valley patterns and (c) presence of complex background noise. The red curves are manually marked foreground area in the image.

(AFIS) work extremely well in matching exemplar fingerprints to each other, there is a considerable performance drop when matching latent fingerprint images to exemplar images. It is generally agreed that latent fingerprint matching is a challenging problem whose performance needs to be significantly improved to reduce the backlog of operational cases in law enforcement agencies. The FBI's Next Generation Identification (NGI) program [160] lists "lights-out" capability for latent matching as one of its major objectives.

2.1.1 Manual Latent Matching

In manual matching of latent prints, latent fingerprint examiners usually follow the *Analysis, Comparison, Evaluation and Verification* (ACE-V) methodology [57]. This basically, is a four step process:

1. *Analysis*: The preliminary step involves analyzing the latent image to ascertain if the latent is of sufficient value for processing and manually marking features such as minutiae, orientation field and ridge frequency. This is usually done by observing the latent image in isolation.

2. *Comparison*: This consists of comparing the latent image to the exemplar image in terms of their features, and assessing the degree of similarity/dissimilarity between latent and exemplar.

3. *Evaluation*: The latent examiner determines the strength of the evidence between the latent and exemplar based on the assessed degree of similarity/dissimilarity between the latent and exemplar in the comparison step.

4. *Verification*: A second latent examiner independently evaluates the latent-exemplar pair to validate the results of the first latent examiner.

The ACE-V procedure is a tedious and time consuming process for the latent examiner as it may involve a large number of fingerprint comparisons between different exemplar fingerprint pairs. For this reason, AFIS is used in the comparison step. Typically, a list of top K matching candidates (with K generally being 50) is retrieved from the exemplar fingerprint database using a latent matcher, which are then visually inspected by the latent examiner to ascertain the best match. This results in one of the following five outcomes:

1. The latent examiner correctly matches the latent fingerprint to its true mated exemplar from the candidate list.

2. The examiner erroneously matches the latent fingerprint to an exemplar fingerprint from the candidate list (which is not the true mate).

3. The examiner correctly excludes an exemplar fingerprint from the candidate list (which is not the true mate) to be the possible mate of the latent fingerprint.

4. The examiner erroneously excludes the true mated exemplar fingerprint of the latent fingerprint from the candidate list to be the possible mate of the latent.

5. The examiner deems the matching result to be inconclusive because he is unable to find any candidate exemplar that is sufficiently similar to the latent print.

Note that while outcome 2) is an erroneous match and outcome 4) an erroneous exclusion, outcome 5) is a reject in the sense that the true mate does not exist in the reference database. The proposed feedback based methodology is designed to minimize the occurrence of outcomes 2), 4) and 5) by initially retrieving a much larger candidate list (e.g. $N = 200$) using the AFIS. Each of these candidates is then viewed as the output of a coarse level match which can be used to refine the features extracted from the latent images. The similarities of these N candidates to the query latent are then recomputed based on the refined latent features to re-rank the candidate list. The latent examiner can then examine the top K candidates ($K < N$) from this re-ranked list for determining the strength of evidence between the latent and candidate exemplars during the evaluation step.

2.1.2 Bottom-up Latent Matching Systems

State-of-the-art latent matching systems [117], [93], [187], [166] are based on the classical bottom-up matching strategy [87]. The bottom-up approach basically builds a system from several sub-systems or components. In essence, there is a sequential "bottom-up" data flow from preprocessing and feature extraction to matching and match score computation. However, the basic assumption in bottom-up systems is that if all the individual sub-systems are functioning well, the system as a whole would function well too [77]. In our opinion, this assumption does not hold good for latent matching systems because the feature extraction sub-system does not work sufficiently well for extracting features from operational latents due to the presence of different kinds of structural noise in the latent image [74].

2.1.3 Proposed Top-Down Latent Matching Framework

On the other hand, the importance of a feedback mechanism between components or the "top-down" data flow is well known [87]. Bottom-up and top-down approaches have been widely used to model human perception system in cognitive science [103]. Oliver et. al [162] used these strategies to develop a computer vision system for recognizing and modeling human interactions. Top-down approaches or feedback mechanisms have been used for object detection and

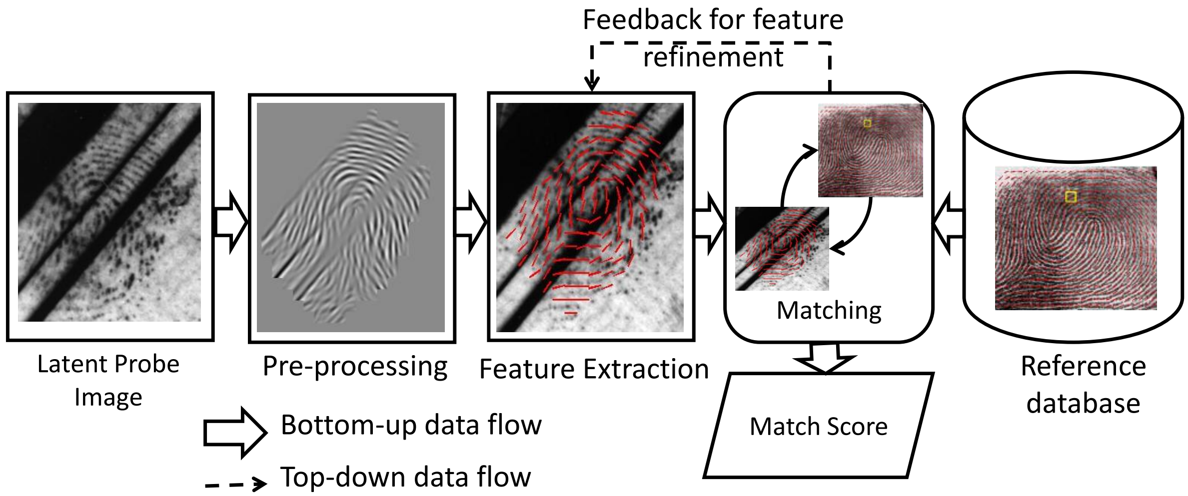

Figure 2.2 Illustrating the typical bottom-up data flow used in latent to exemplar matching systems. The dotted line shows the feedback path (top-down data flow) in the proposed matching paradigm.

segmentation [161], [63] and for improving the decision making capabilities of artificial neural networks [61].

In this chapter, we extend this idea of feedback to latent fingerprint matching by incorporating a top-down data flow between the matching module and feature extraction module (see the dotted line in Figure 2.2)[3]. We devise systemic ways to use information in exemplars for refining latent features, e.g., ridge orientation and frequency, and use them to develop a feedback paradigm which could be integrated into a latent matcher to improve its matching accuracy. Note that there is a difference between the feedback approach used in manual latent matching [85] and the idea of using feedback from exemplars for refining latent features proposed in this chapter. In manual latent matching, the top-down information usually refers to the prior training, bias and the state of mind of latent examiners which may influence the outcome of latent examination. The proposed paradigm, however, uses feedback in the matching stage to refine the features extracted from the latent images. This feedback is particularly useful because features extracted from the latent are often unreliable due to their poor quality. In our opinion, matching latent images based on the

[3]Preliminary results of this research were published in proceedings of the International Conference on Biometrics (ICB), 2013 [135]. Extended version with detailed analysis was published in IEEE Transactions on Pattern Analysis and Machine Intelligence (TPAMI), 2014 [56].

initially extracted set of features without any prior information (bottom-up mode) is prone to error. Additional top-down information flow provided by feedback allows the matching system to use the hypothesized exemplar mate to refine initially extracted features from the latent and improve the matching accuracy.

Nevertheless, there are cases when the latent image is of good quality and reliable features can be extracted in the bottom-up mode, making feedback unnecessary. To determine if feedback is indeed needed for a latent query, we devise a global criterion based on the match score probability distribution obtained by matching the latent to the top K candidate exemplars. For determining the regions within the latent image which need feedback as well the regions of the exemplar which are of sufficiently good quality to provide feedback, we use a local fingerprint quality metric.

To demonstrate the effectiveness of the proposed feedback based latent matching strategy, we integrate the feedback paradigm with a state-of-the-art latent matcher [166] and conduct experiments on two different latent databases (NIST SD27 [148] and WVU [150]). A marked improvement in matching accuracies is observed when using feedback from exemplars in the latent matching process. Besides, there is only one latent query for which feedback is not provided when it could have been useful. This demonstrates the efficacy of the proposed criterion to decide if feedback is needed for a latent query.

2.2 Feedback Paradigm for Latent Matching

Let I^L be the latent probe image and I^R be an exemplar image from the reference database. Let Θ be the set of features extracted from the fingerprint image. Here we denote the feature set corresponding to the latent by Θ^L and that of the exemplar image by Θ^R. Typically, feature set Θ^R is pre-computed for each exemplar image. The bottom-up matching process involves matching the two representations Θ^L and Θ^R and assigning the initial match score Sim_I (see Figure 2.2):

$$Sim_I = S_I(\Theta^L, \Theta^R). \tag{2.1}$$

Here S_I is the similarity function used to generate the match score between the latent fingerprint feature set Θ^L and the exemplar feature set Θ^R.

The top K candidate exemplars based on these similarities are retrieved from the reference database. Feedback is then provided from the feature set Θ^R of the candidate exemplar image to refine the feature set Θ^L initially computed from the latent image. The refined feature set denoted by $\hat{\Theta}^L$ is computed using a function f of the initial feature set Θ^L and the feedback information F as follows:

$$\hat{\Theta}^L = f(\Theta^L, F). \tag{2.2}$$

The feedback feature similarity Sim_F between $\hat{\Theta}^L$ and Θ^R is then computed using the similarity function S_F as follows:

$$Sim_F = S_F(\hat{\Theta}^L, \Theta^R). \tag{2.3}$$

Finally, the updated match score Sim_U is calculated from Sim_I and Sim_F using a match score fusion operator $\otimes$:

$$Sim_U = Sim_I \otimes Sim_F. \tag{2.4}$$

2.3 Re-sorting Candidate List based on Feedback

The feedback based paradigm is applied for re-sorting the candidate list of top K candidate exemplars retrieved by a state-of-the-art latent matcher [166] (see Figure 2.3). The matcher in [166] is

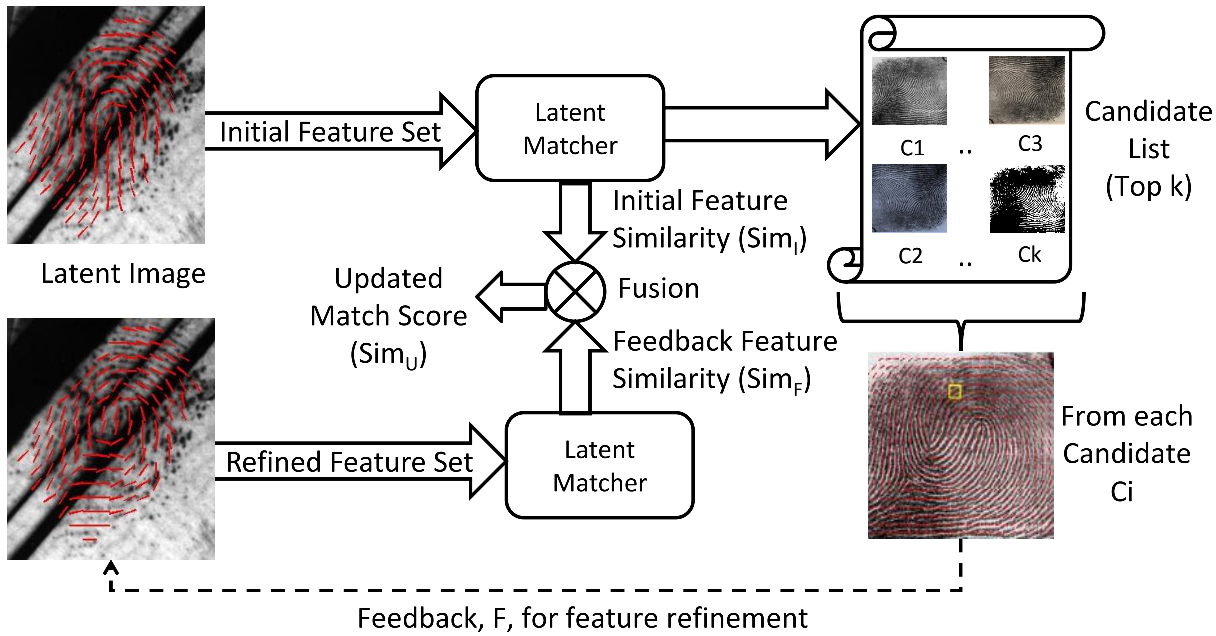

Figure 2.3 Re-sorting the candidate list using feedback. Note the refinement of latent features due to feedback.

chosen because it is one of the best performing available latent matchers[4] using minimal human input (requires only marked minutiae for latents). This matcher is referred to as the *baseline matcher* henceforth because it is used to match a latent to the reference database to generate the candidate list.

The feedback implementation broadly consists of the following four steps (see Figures 2.4 and 2.5):

1. *Initial Matching and Alignment*: The baseline matcher is used to obtain the initial match score, and to generate the minutiae correspondences between an input latent and an exemplar image. The latent is then aligned to the exemplar image using the scaling, rotation and translation parameters estimated based on the minutiae correspondences.

[4]While we have access to a commercial latent SDK, we were not able to use it in our experiments because the SDK does not output minutiae correspondences between latent and exemplar. While some of the commercial tenprint SDKs, such as Verifinger by Neurotechnology (http://www.neurotechnology.com/verifinger.html), provide minutiae correspondence, they do not perform well for latent to exemplar matching since they were not designed for this scenario.

2. *Exemplar Feature Extraction*: Exemplar image is divided into blocks of size 16 by 16. Ridge orientation and frequency features are extracted within each block of the exemplar.

3. *Latent Feature Extraction and Refinement*: Latent image is divided into blocks of size 16 by 16. For each block in the latent, ridge orientation and frequency features corresponding to peak points in the magnitude spectrum of the frequency domain are extracted. The extracted features within each block are then refined based on the feedback from features extracted in the corresponding exemplar block. Feedback consists of orientation differences between each extracted ridge orientation in the latent block and the ridge orientation in the corresponding exemplar block.

4. *Match Score Computation*: The similarity between the refined latent features and the exemplar features is used to compute an updated match score between the latent and the exemplar.

The candidate list is re-sorted based on the updated match scores between the latent and the retrieved exemplars returned by the baseline matcher.

2.3.1 Initial Matching and Alignment

Manually marked minutiae in the latent image and automatically extracted minutiae from the exemplar image (using a commercial off-the-shelf (COTS) matcher) are fed as input to the baseline matcher to obtain the initial match score Sim_I and a list of matched minutiae.[5] Let $M^L = \{(x_i^L, y_i^L, \theta_i^L)|i = 1, 2, \cdots, P\}$ represent the list of matched minutiae for the latent and $M^R = \{(x_i^R, y_i^R, \theta_i^R)|i = 1, 2, \cdots, P\}$ represent the list of corresponding matched minutiae for the exemplar, where (x, y) are the coordinate values, θ is the direction of minutia and P is the number of matched minutiae pairs.

[5]Feeding the baseline matcher used in our experiment with automatically extracted minutiae from latents either does not generate any minutiae correspondences or generates a number of false minutiae correspondences. This degrades the alignment of the latent-exemplar pair and results in improper feedback. However, this paradigm can be used in the “lights-out” identification mode, provided the baseline matcher does not produce many false minutiae correspondences and the latent-exemplar pair can be well aligned.

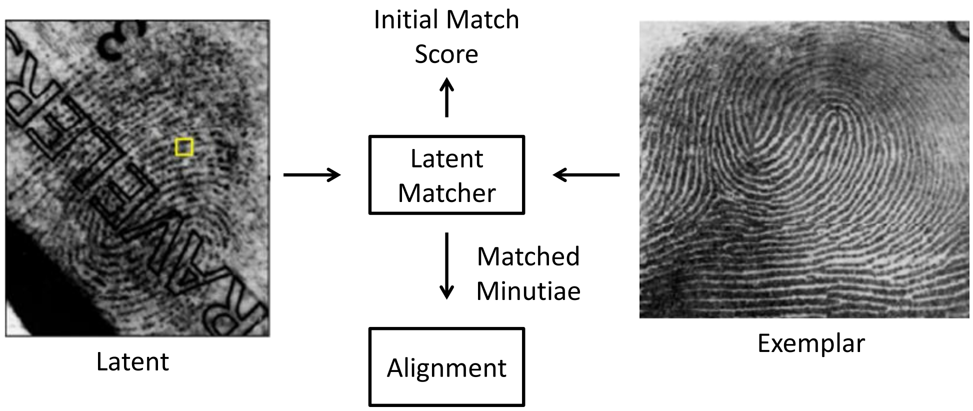

(a) Initial Matching and Alignment

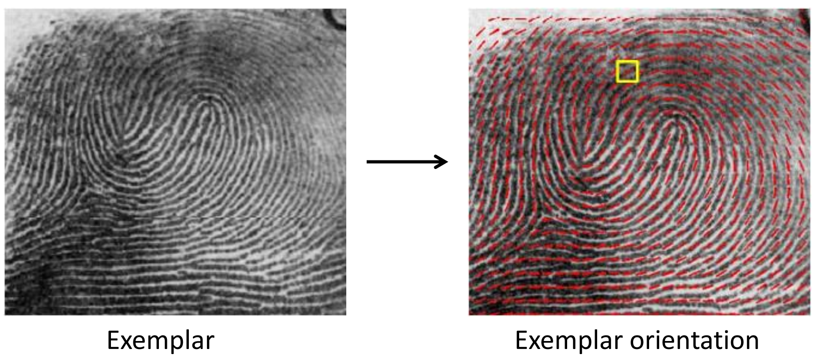

(b) Exemplar Feature Extraction

Figure 2.4 Major steps involved in latent fingerprint matching using feedback from exemplar. Shown in yellow is a pair of corresponding latent and exemplar blocks.

Depending on the number of matched minutiae pairs P, the transformation T for aligning the latent to the exemplar is estimated differently:

Case I ($P \geq 2$): The transformation $T(x, y; a, b, t_x, t_y)$ is estimated by solving the following set of equations:

$$\begin{bmatrix} x_i^R \\ y_i^R \end{bmatrix} = \begin{bmatrix} a & -b \\ b & a \end{bmatrix} \begin{bmatrix} x_i^L \\ y_i^L \end{bmatrix} + \begin{bmatrix} t_x \\ t_y \end{bmatrix}, i = 1, 2, \cdots, P. \tag{2.5}$$

Here, $a = s\cos\Delta\theta$ and $b = s\sin\Delta\theta$, where s is the scale parameter and $\Delta\theta$ is the rotation angle, and t_x and t_y are the translation parameters. This system of linear equations can be solved by minimizing the least square error.

Now, given the coordinates (x^L, y^L) of any point in the latent image, its transformed coordinates (x^R, y^R) in the exemplar coordinate system can be obtained by using the transformation T:

$$\begin{bmatrix} x^R \\ y^R \end{bmatrix} = \begin{bmatrix} a & -b \\ b & a \end{bmatrix} \begin{bmatrix} x^L \\ y^L \end{bmatrix} + \begin{bmatrix} t_x \\ t_y \end{bmatrix}. \tag{2.6}$$

Case II (P = 1): If only one pair of matched minutiae is available, the transformation function is estimated by utilizing both the minutiae location and direction. Let $(x_1^L, y_1^L, \theta_1^L)$ and $(x_1^R, y_1^R, \theta_1^R)$ be the matching pair of minutiae in the latent and exemplar, respectively. The rotation angle from latent to exemplar is then estimated by:

$$\Delta\theta = \theta_1^R - \theta_1^L. \tag{2.7}$$

Given a point (x^L, y^L) in the latent, its transformed coordinates (x^R, y^R) in the exemplar coordinate system can be calculated by using the transformation T:

$$\begin{bmatrix} x^R \\ y^R \end{bmatrix} = \begin{bmatrix} \cos\Delta\theta & -\sin\Delta\theta \\ \sin\Delta\theta & \cos\Delta\theta \end{bmatrix} \begin{bmatrix} x^L - x_1^L \\ y^L - y_1^L \end{bmatrix} + \begin{bmatrix} x_1^R \\ y_1^R \end{bmatrix}. \tag{2.8}$$

Note that this transformation does not include any scaling factor because it cannot be estimated based on just a single pair of matched minutiae.

To summarize, translation, scaling and rotation parameters for aligning the latent and the exemplar are estimated based on the matched minutiae pairs. The transformation is then used to align the two images.

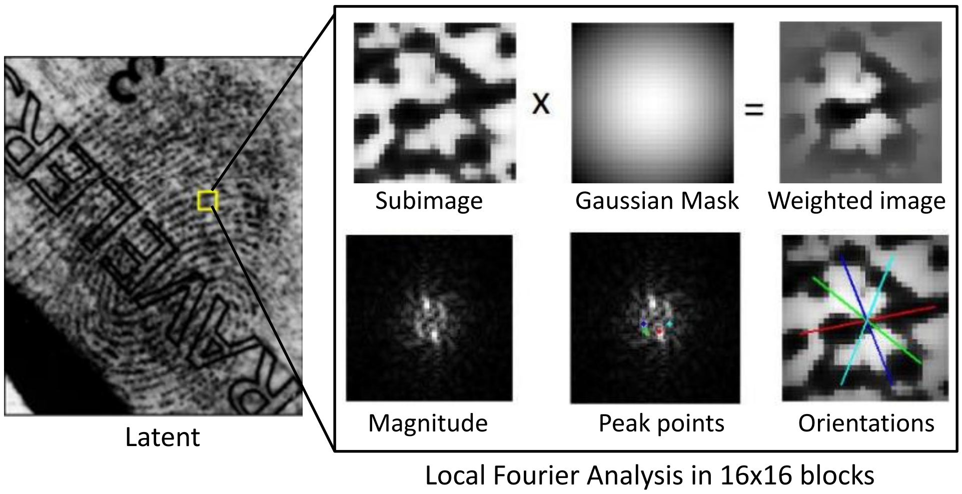

(a) Latent Feature Extraction

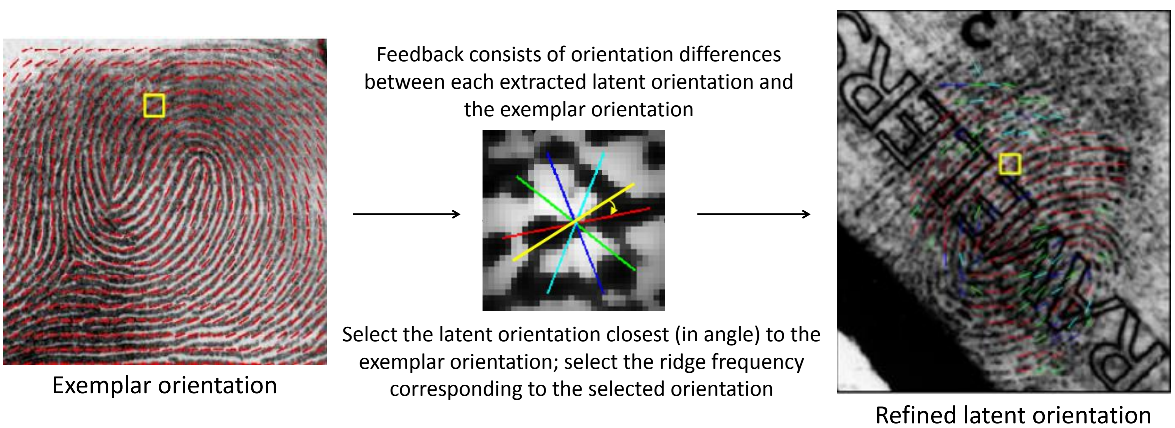

(b) Latent Feature Refinement

Figure 2.5 Major steps involved in latent fingerprint matching using feedback from exemplar. The refined latent features illustrated in (b) are used to rematch the latent to the exemplar and re-sort the candidate list. Shown in yellow is a pair of corresponding latent and exemplar blocks.

2.3.2 Exemplar Feature Extraction

Two different types of local features are computed for the exemplar image, namely ridge orientation and ridge frequency. Given an exemplar image I^R, its ridge skeleton image I^R_{sk} is first extracted using a COTS matcher. The skeleton image is then divided into 16 by 16 pixel blocks. Ridge orientation and ridge frequency are then computed for each block I^R_B in the skeleton image I^R_{sk}.

2.3.3 Latent Feature Extraction and Refinement

The level one features (e.g. ridge orientation and ridge frequency) in the latent image are difficult to extract because of the presence of structured noise in the background. Local Fourier analysis is used for this purpose because it has been shown to be resilient to complex background noise [116], [187].

Similar to the exemplar image, the latent image I^L is first divided into 16 by 16 blocks. For each block I^L_B in the region of interest (ROI) of the latent, the local ridge orientation and ridge frequency features are obtained as follows:

1. A 32×32 sub-image $I^L_{B'}$ centered at the block I^L_B is extracted and convolved with a Gaussian filter of the same size with σ = 16.

2. The sub-image $I^L_{B'}$ is padded with zeros on the borders to get a 64×64 image $I^L_{B''}$. This is done to increase the number of sampling points in the discrete Fourier domain.

3. Fast Fourier Transform (FFT) is applied to the padded sub-image $I^L_{B''}$. For each peak (u, v) in the magnitude spectrum image, the corresponding orientation α and frequency f is computed by:

$$\alpha^L = \arctan\left(\frac{u}{v}\right), \tag{2.9}$$

$$f^L = \sqrt{(u^2 + v^2)}/64. \tag{2.10}$$

4. A set of L peak points $H = \{(u_i, v_i)|i = 1, 2, \cdots, L\}$ of highest magnitude values, and with frequency value satisfying $\frac{1}{16} < f < \frac{13}{64}$, is selected. Note that L is set to 4 in our implementation.

5. The (x, y) coordinates of the central pixel in the block I_B^L are then transformed to the exemplar coordinate system using the transformation function T estimated previously. Let the transformed coordinates of that pixel be represented as (x', y').

6. Let α^R be the corresponding ridge orientation of the block containing the pixel (x', y') in the exemplar image. The peak point l (from the set H) corresponding to the closest ridge orientation to α^R from amongst the ridge orientations α_i^L, is then selected as follows:

$$l = \arg\min_i \varphi(\alpha_i^L + \Delta\theta, \alpha^R), \tag{2.11}$$

where $1 \leq i \leq L$ and

$$\varphi(\alpha, \beta) = \begin{cases} |\alpha - \beta|, \text{ if } |\alpha - \beta| < 90, \\ 180 - |\alpha - \beta|, \text{ otherwise }. \end{cases} \tag{2.12}$$

Here, $\varphi(\alpha, \beta)$ is the function to determine the difference between ridge orientations α and β and $\Delta\theta$ is the rotation angle used to align the two ridge orientations α and β.

7. The ridge orientation and ridge frequency values corresponding to the selected peak point (u_l, v_l) are then chosen as the refined ridge orientation and ridge frequency features for the block I_B^L in latent image.

Note that the refined ridge orientation and ridge frequency features are selected based on the exemplar features, and this essentially constitutes the top-down information flow or feedback from the exemplar.

2.3.4 Match Score Computation

The functions to compute the similarity between the exemplar features and the refined latent features after feedback should result in improved similarity between mated latent-exemplar pairs. Thus, the similarity function should be based on the underlying distribution of feature differences obtained from genuine latent-exemplar matches. Assume that the orientation and frequency differences between the refined latent features and exemplar features within each block are independent and identically distributed. To learn the characteristics of the genuine distribution model, 50 mated latent-exemplar pairs from the NIST SD27 [148] and WVU database [150] are randomly sampled to estimate the distributions. We observe that the genuine distribution of orientation differences approximately follows a cosine curve whereas that of ridge frequency differences approximates an exponential curve; cosine and exponential functions are hence used for computing feedback orientation and frequency similarities, respectively.

For computing the feedback ridge orientation and frequency similarities, the overlapping region between the latent and exemplar is first determined using the transformation function T. Within the overlapping region, the ridge orientation and ridge frequency similarities Sim_α and Sim_f are then computed as:

$$Sim_\alpha = \frac{1}{Num}\sum_{i=1}^{Num}\cos\left(-\frac{\varphi(\alpha_i^L+\Delta\theta,\alpha_i^R)}{\mu_\alpha}\right), \tag{2.13}$$

$$Sim_f = \frac{1}{Num}\sum_{i=1}^{Num}\exp\left(-\frac{\left|\frac{1}{f_i^L}-\frac{1}{f_i^R}\right|}{\mu_f}\right), \tag{2.14}$$

$$Num \geq Num_{min},$$

where Num is the number of overlapping blocks; Num_{min} is a threshold on the minimum number of blocks needed in the overlapping region and is set to 10 in our experiments; α_i^L and α_i^R are the ridge orientations and f_i^L and f_i^R are the ridge frequencies of the i^{th} overlapping block from the latent and exemplar, respectively; μ_α and μ_f are two normalization parameters which are empirically set to 12 and 8, respectively. The initial match score Sim_I is first normalized using min-max score normalization [121], and the orientation and frequency similarities Sim_α and Sim_f are then combined with the normalized initial match score Sim_{NI} based on product fusion to obtain the updated match score Sim_U as follows:

$$Sim_U = Sim_{NI} \times Sim_\alpha \times Sim_f. \tag{2.15}$$

2.4 The Adequacy of Feedback

Although feedback from exemplars can be used to refine latent features, the feedback may not be necessary when the latent is of sufficient good quality such that its features can be reliably extracted. Bottom-up latent to exemplar matching may suffice for such cases and feedback may not add any value to the latent matching process. Clearly, it would be useful to have an objective criterion to ascertain if feedback can potentially improve the matching accuracy for each latent query. Besides, since feedback is applied within each block in the latent, decision to apply feedback can also be made locally at the block level. To determine the need for feedback, we design a *global criterion* based on the match score distribution (of the top K match scores returned by the baseline latent matcher), and a *local criterion* based on the local quality of the latent-exemplar pair being matched.

2.4.1 Global Criterion

We design a simple criterion to decide whether feedback is needed for a particular latent query based on the probability distribution of the top K match scores returned by the baseline matcher.

2.4.1.1 Modelling the Match Score Distribution

This distribution is based on the similarity function used in the baseline matcher. The latent matcher used in our experiments [166] uses an exponential similarity function, so we use the exponential distribution to model the probability distribution of match scores. Alternately, we could

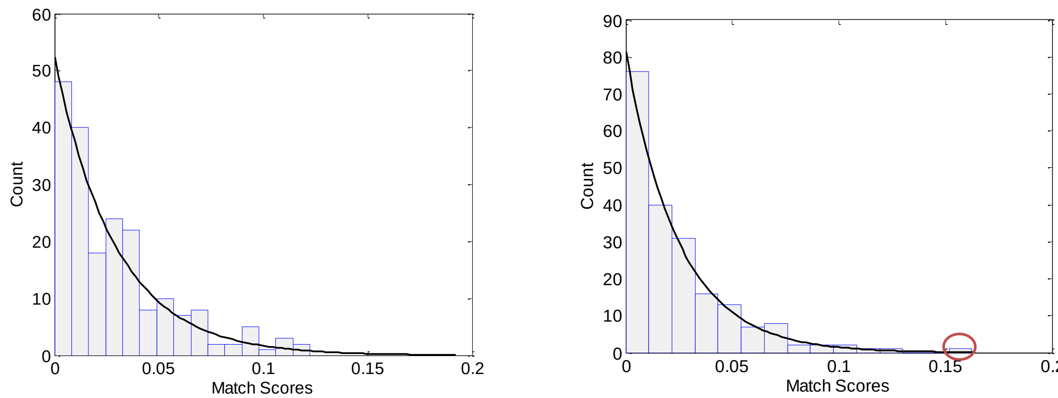

(a) (b)

Figure 2.6 Exemplifying the global criterion for feedback: (a) match score distribution for a particular latent query without an upper outlier, and (b) with an upper outlier present (marked in red). Feedback is needed in case (a), but not needed in (b).

estimate the probability densities using the match score histogram, and then fit a parametric distribution to the histogram. To measure the goodness of fit of the exponential distribution model in our case, we used the chi-square goodness of fit test [133]. For this, we randomly sampled 40 latent images from the NIST SD27 database [148], and then tested the goodness of fit of the exponential distribution on the set of top K match scores generated by the matcher for each latent.

2.4.1.2 Test for the presence of an upper outlier

We observe that if the true mated exemplar print is indeed retrieved at rank-1 by the baseline latent matcher operating in bottom-up mode, then there is a sizeable difference between the rank-1 and other match scores. In other words, the rank-1 match score is an upper outlier in the probability distribution of the top K match scores. Thus, the problem of determining whether feedback is needed or not becomes equivalent to the problem of detecting whether an upper outlier exists in the match score distribution (see Figure 2.6).

We now describe a hypothesis test for detecting the presence of an upper outlier for exponential density used here [132] and its usage in determining the need for feedback.

The pdf of the exponential distribution with scale parameter λ is given by

$$f(x) = \frac{1}{\lambda} e^{-\frac{x}{\lambda}};\ x > 0;\ \lambda > 0. \tag{2.16}$$

Let $X = \{X_1, X_2, ..., X_n\}$ be an independent and identically distributed (i.i.d) random sample of size n generated from an exponential distribution given by Eqn. (2.16), and $X_{(1)}, X_{(2)}, ..., X_{(n)}$ be the corresponding order statistics. Order statistics are the sample values in the order of their magnitude with $X_{(1)} < X_{(2)} \cdots < X_{(n)}$. In our case, X pertains to the set of top K match scores, $X_{(1)}$ is the match score obtained by matching the latent to the K^{th} candidate exemplar, and $X_{(n)}$ is the match score generated on matching the latent to the 1^{st} candidate exemplar.

To test for the upper outlier, the null hypothesis H_0 and the alternative hypothesis H_1 are defined as:

H_0: All observations in the set X are i.i.d from the exponential distribution.

H_1: Maximum match score is an upper outlier of the match score distribution.

The test statistic Z for testing the hypothesis is defined as:

$$Z = \frac{X_{(n)} - X_{(n-1)}}{S_n};\ S_n = \sum_{i=1}^{n} X_i. \tag{2.17}$$

To determine the critical value for the test, we obtain the distribution of the test statistic Z under the null hypothesis H_0. The sum S_n of n i.i.d. exponential random variables in the set X with a fixed scale parameter λ defined in Eqn. (2.18) follows a gamma distribution with shape parameter n and scale parameter λ [70]:

$$g(s, n, \lambda) = \frac{1}{\lambda^n} \frac{1}{\tau(n)} s^{n-1} e^{-\frac{s}{\lambda}}. \tag{2.18}$$

Here, $\tau(n)$ is the gamma function. The test statistic Z can be viewed as the difference of two random variables Z_1 and Z_2 where $Z_1 = X_{(n)}/S_n$ and $Z_2 = X_{(n-1)}/S_n$. Each of these random variables Z_1 and Z_2 follows a beta distribution with shape parameters 1 and $n-1$; the joint distribution of Z_1 and Z_2 [134] is then given by:

$$
\begin{aligned}
h(z_1, z_2) = n(n-1)(n-2)^2 \big\{ &(1 - z_1 - z_2)^{n-3} \\
&- \binom{n-2}{1} (1 - z_1 - 2z_2)^{n-3} \\
&+ \binom{n-2}{2} (1 - z_1 - 3z_2)^{n-3} \\
- \cdots + (-1)^{t-1} &\binom{n-2}{t-1} (1 - z_1 - tz_2)^{n-3} \big\}.
\end{aligned}
\tag{2.19}
$$

Here $t = (1 - z_1)/z_2,\ (z_1 + z_2) < 1,\ z_1 + (n-1)z_2 > 1,\ z_1 > z_2$. Now, the density of Z can be computed using a bivariate transformation on the joint density of Z_1 and Z_2 [132] (Eqn. (2.19)):

$$
\begin{aligned}
m(z) = \frac{n(n-1)^2}{n^{n-2}} \bigg\{ &\frac{(n-2)^{n-2}}{2} - \binom{n-2}{1} \frac{(n-3)^{n-2}}{3} \\
&+ \cdots + (-1)^{n-3} \binom{n-2}{n-3} \frac{1}{n-1} \bigg\} (1 - z)^{n-2}.
\end{aligned}
\tag{2.20}
$$

Here $0 < z < 1$. The probability of the test statistic Z being greater than the critical value $z(\alpha)$ at significance level α can be obtained from Eqn. (2.20) as follows:

$$
P[Z > z(\alpha)|H_0] = \int\limits_{z(\alpha)}^{1} m(z) = (1 - z(\alpha))^{n-1} = \alpha. \tag{2.21}
$$

Thus, the critical value $z(\alpha)$ is:

$$
z(\alpha) = 1 - \alpha^{\frac{1}{n-1}}. \tag{2.22}
$$

For $X_{(n)}$ to be the outlier, the realized value of the test statistic $Z = z$ should be greater than the critical value $z(\alpha)$. For the *global criterion* for feedback, we define an indicator random variable I_F which takes the value 1 when feedback is needed and 0, if it is not needed:

$$I_F = \begin{cases} 0, & z > z(\alpha), \\ 1, & \text{otherwise} \end{cases} \tag{2.23}$$

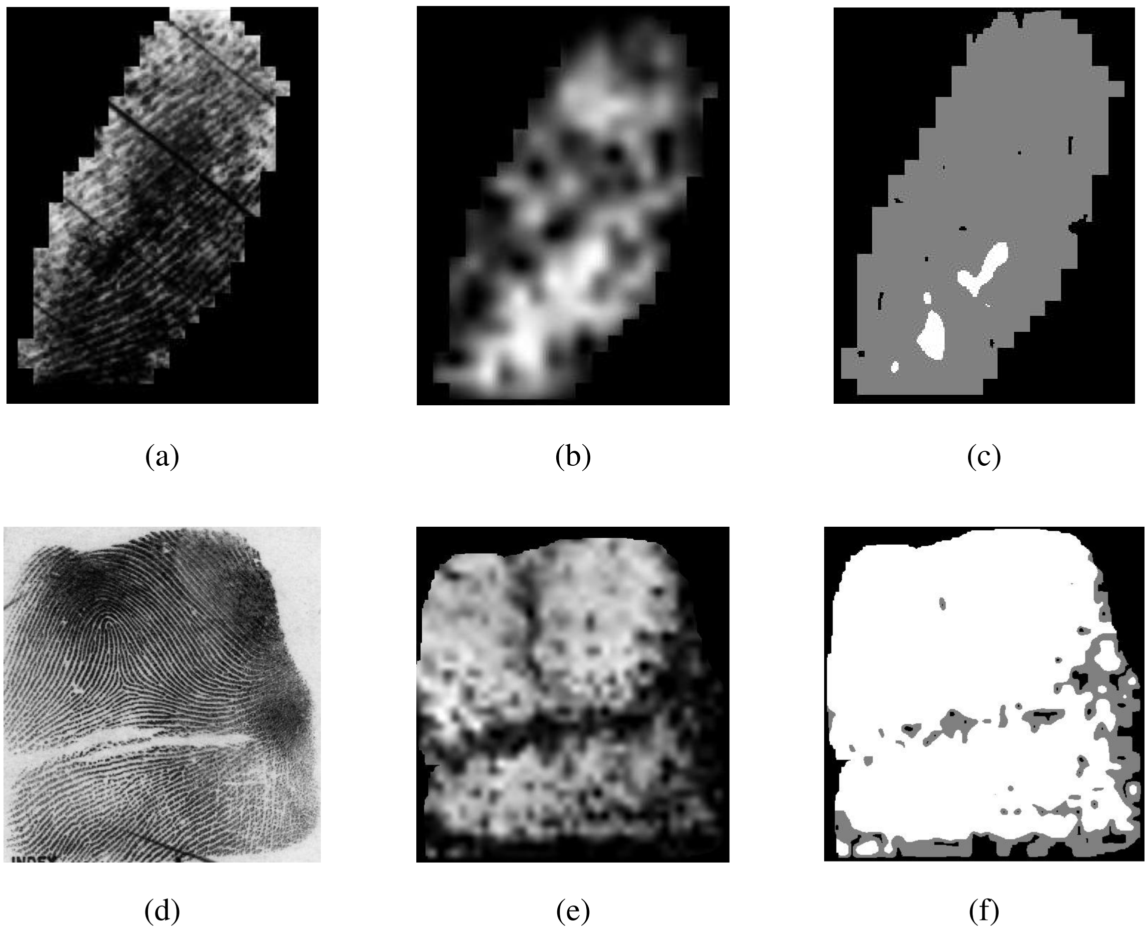

Figure 2.7 Exemplifying the local criterion for feedback: (a) a latent image, (b) its ridge clarity map and (c) regions which need feedback (shown in grey); (d) an exemplar image, (e) its ridge clarity map and (f) regions which are reliable for providing feedback (shown in white).

2.4.2 Local Criterion

Even though feedback may be potentially useful for a particular latent query, there may be some good quality regions within the latent image which do not require feedback. Besides, the exemplar print region from where feedback is being taken may be of poor quality which may not be reliable for feedback. For deciding whether feedback is needed locally, we use the local fingerprint quality metric proposed in [190] called the *Ridge Clarity*. While this metric was proposed for latent images, we find that it is appropriate for estimating the local quality of exemplar fingerprints (Figure 2.7).

The computation of ridge clarity for an image I involves the following four steps:

1. *Contrast Enhancement*: Obtain the contrast-enhanced image I_C [94]:

$$I_C = sign(I - I_S) \times \log(1 + |I - I_S|) \tag{2.24}$$

   Here, I_S is the image obtained using a 15 x 15 averaging filter on I, and $sign(x)$ is the signum function which outputs 1 if $x > 0$ and 0 otherwise.

2. *Frequency Domain Analysis*: The contrast-enhanced image I_C is divided into blocks of size 16 x 16, and a 32 x 32 subimage $I_C(x, y)$ is obtained around the center (x, y) of each block. $I_C(x, y)$ is then padded with zeros to obtain a 64 x 64 subimage $I_C^*(x, y)$. This subimage $I_C^*(x, y)$ is transformed into the frequency domain to obtain $F_C^*(s, t)$. Two peak points (s_1, t_1) and (s_2, t_2) corresponding to the two local amplitude maxima within frequency range $[0.0625, 0.2]$ in $F_C^*(s, t)$ are then selected [116]. The 2-D sine wave $w_i(p, q)$ at the i_{th} peak point in $F_C^*(s, t)$; $i = \{1, 2\}$ with amplitude a_i, frequency f_i, angle θ_i and phase ϕ_i is given by:

$$w_i(p, q) = a_i \sin(2\pi f_i(\cos(\theta_i)p + \sin(\theta_i)q) + \phi_i), \tag{2.25}$$

   where

$$a_i = |F_C^*(s_i, t_i)|, f_i = \frac{\sqrt{s_i^2 + t_i^2}}{64},$$

$$\theta_i = \arctan\left(\frac{s_i}{t_i}\right), \phi_i = \arctan\left[\frac{Im(F_C^*(s_i,t_i))}{Re(F_C^*(s_i,t_i))}\right].$$

3. *Ridge Continuity Map Computation*: Two neighbouring blocks b_1 and b_2 are said to be continuous if the following conditions hold for their corresponding sine waves bw_1 and bw_2:

$$\min\{|b\theta_1, b\theta_2|, \pi - |b\theta_1, b\theta_2|\} \leq T_{b\theta},$$

$$\left|\frac{1}{bf_1} - \frac{1}{bf_2}\right| \leq T_{bf},$$

$$\frac{1}{16}\sum_{\{p,q\in\psi\}}\left|\frac{bw_1(p,q)}{ba_1} - \frac{bw_2(p,q)}{ba_2}\right| \leq T_{bp}. \tag{2.26}$$

Here, $T_{b_\theta}, T_{bf}, T_{bp}$ are constants set to $\pi/10$, 3 and 0.6, respectively, and ψ refers to the set of 16 pixels which lie on the border of two neighbouring blocks. Define an indicator function I_{fc} for ridge continuity as:

$$I_{fc} = \begin{cases} 1, & sw_1 \text{ and } sw_2 \text{ are continuous,} \\ 0, & \text{otherwise.} \end{cases} \tag{2.27}$$

The ridge continuity map R_{cont} is then computed as:

$$\begin{aligned} R_{cont}[p,q] = \sum_{[p*,q*\in N]} \max\{&I_{fc}(w_1(p,q), w_1(p*,q*)), \\ &I_{fc}(w_2(p,q), w_2(p*,q*))\} \end{aligned} \tag{2.28}$$

4. *Ridge Clarity Map Computation*: Finally, the ridge clarity for each block centered at $[p, q]$ can be computed by taking the product of the amplitude with the ridge continuity map as follows:

$$R_{clar}[p, q] = a_1(p, q) \times R_{cont}[p, q]. \tag{2.29}$$

To determine the regions within each latent image I^L which need feedback, we apply a threshold th_1 on the local ridge clarity value. Let us define an indicator random variable I_F^L for each block centered at $[p, q]$ which equals 1 for latent regions which need feedback (Figure 2.7c):

$$I_F^L = \begin{cases} 1, & I^L(R_{clar}[p, q]) > th_1, \\ 0, & \text{otherwise.} \end{cases} \tag{2.30}$$

Similarly, to decide the regions within each exemplar I^R which can provide feedback we use a threshold th_2 on the local ridge clarity value. Let us define an indicator function I_F^R for each block centered at $[p, q]$ which takes the value 1 in exemplar regions which can provide feedback (Figure 2.7f):

$$I_F^R = \begin{cases} 1, & I^R(R_{clar}[p, q]) > th_2, \\ 0, & \text{otherwise.} \end{cases} \tag{2.31}$$

Different values of the thresholds th_1 and th_2 were tested, and they are empirically set to 0.1 and 0.9, respectively.

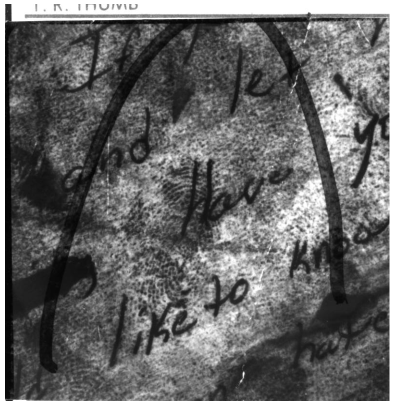

(a)

(b)

(c)

(d)

Figure 2.8 Sample latent images from (a) NIST SD27 and (c) WVU latent databases. Their mated exemplars are shown in (b) and (d), respectively.

2.5 Experimental Evaluation

2.5.1 Databases

The proposed feedback paradigm was evaluated on two different latent fingerprint databases, NIST SD27 [148] and WVU [150]. To increase the size of the reference database, we included 27,000 rolled fingerprint images from NIST SD14 [147] database and 68,002 rolled images provided by the Michigan State Police. So, the reference database consisted of 100,000 rolled fingerprints.

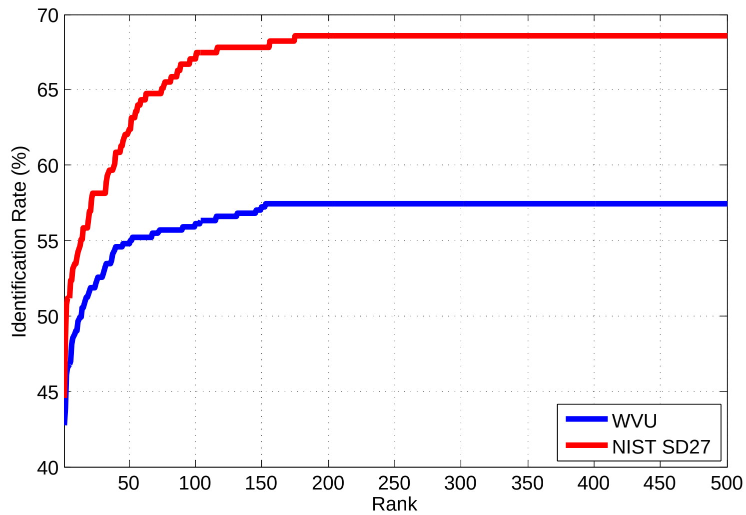

Figure 2.9 Performance of the baseline latent matcher on the two latent databases against a reference database of 100,000 exemplars.

2.5.1.1 NIST SD 27

NIST SD27 database contains 258 latent images as well as their corresponding exemplar images from operational cases. The latent images in NIST SD27 have good contrast but contain complex background noise (Figure 2.8 (a)). The resolution of each image is 500 ppi.

2.5.1.2 WVU

The WVU database was collected in a laboratory environment at West Virginia University. It includes 449 latent images and 4,740 exemplar images out of which 449 exemplars are the true mates of the latents. The original resolution of each fingerprint image in the WVU database is 1000ppi but it was downsampled to 500ppi for our experiments. The latent images in this database have relatively clean background, but poor image contrast as compared to latents in NIST SD27 (Figure 2.8 (c)).

Table 2.1 The total number of latents where (a) feedback is applied, (b) feedback is applied when it is not needed (mated examplar retrieved at rank-1 by the baseline matcher), and (c) feedback is not applied when it could have been useful (mated exemplar returned amongst the top 200 candidates but not at rank-1 by the baseline matcher) based on the global criterion for feedback (at significance level = 0.05).

Database	**# Latents for which feedback applied**	**# Latents where feedback applied but not needed**	**# Latents where feedback not applied but needed**
NIST SD27 (258 latents)	172	1	1
WVU (449 latents)	254	12	0

2.5.2 Size of the Candidate List (K)

One of the critical parameters while applying the paradigm is the length of the candidate list K. While choosing a large value of K would improve the odds of the mated exemplar being retrieved in the candidate list, it would also take more time to re-sort the candidate list. To find the optimal value of K, we plot the Cumulative Match Characteristics (CMC) curves of the baseline matchers used in our experiments (Figure 2.9). We can see that the performance gain stabilizes by rank 200. So, to optimize both accuracy and speed, the value of K is set to 200.

2.5.3 Effectiveness of the Global Criterion for Feedback

Applying feedback to a latent when it is not needed adds computational complexity without improving the accuracy. The global criterion for feedback obviates the need for feedback in about 86 out of 258 latent queries for the NIST SD27 database and in about 195 out of 449 cases for the WVU database at significance level of 0.05. Table 2.1 lists the number of latent queries for which (i) feedback is applied even when the mated exemplar is retrieved at rank-1 by the baseline matcher [166], and (ii) feedback is not applied when the mated exemplar is not retrieved at rank-1 (but is amongst the top 200 candidates returned by the baseline matcher [166]). The low number of such cases demonstrate the efficacy of the proposed criterion in determining the need for feedback.

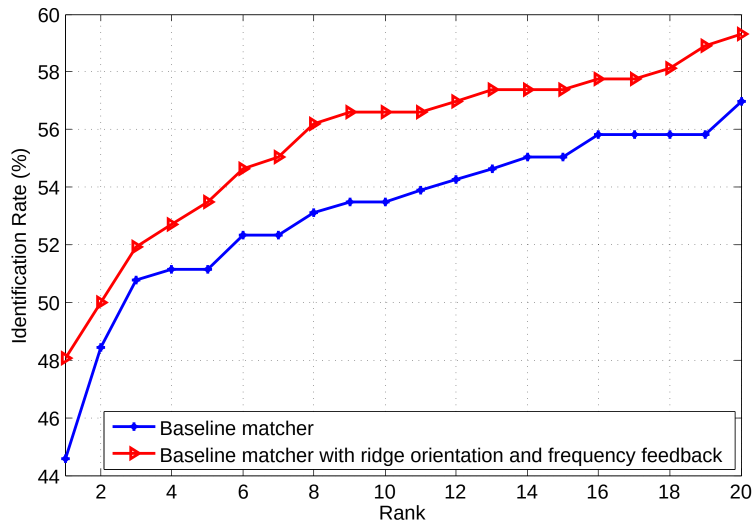

(a)

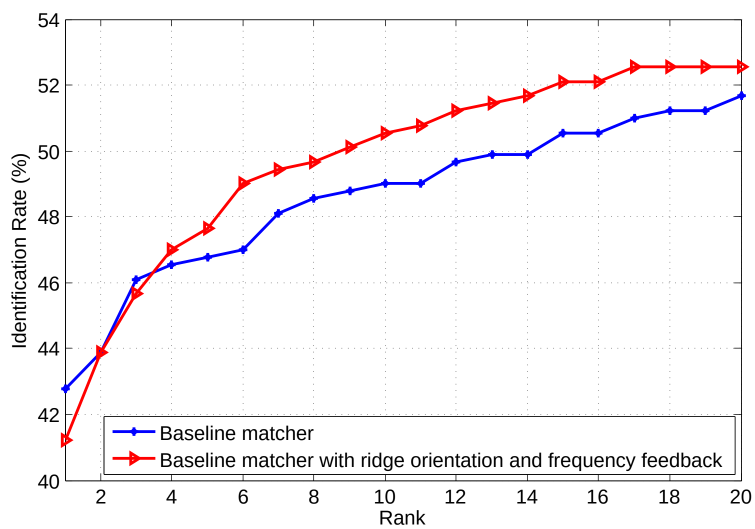

(b)

Figure 2.10 Performance of the baseline matcher with and without ridge orientation and frequency feedback on (a) NIST SD27 and (b) WVU latent database (against a reference database of 100,000 exemplars).

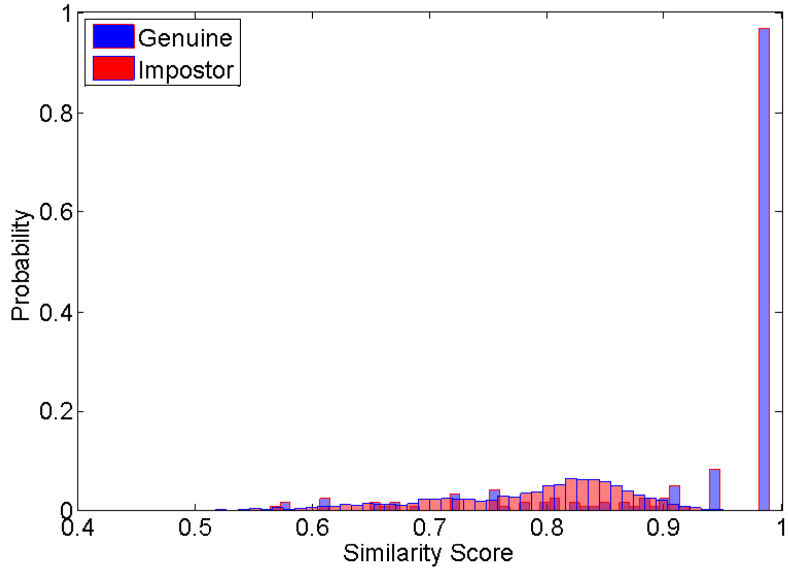

(a)

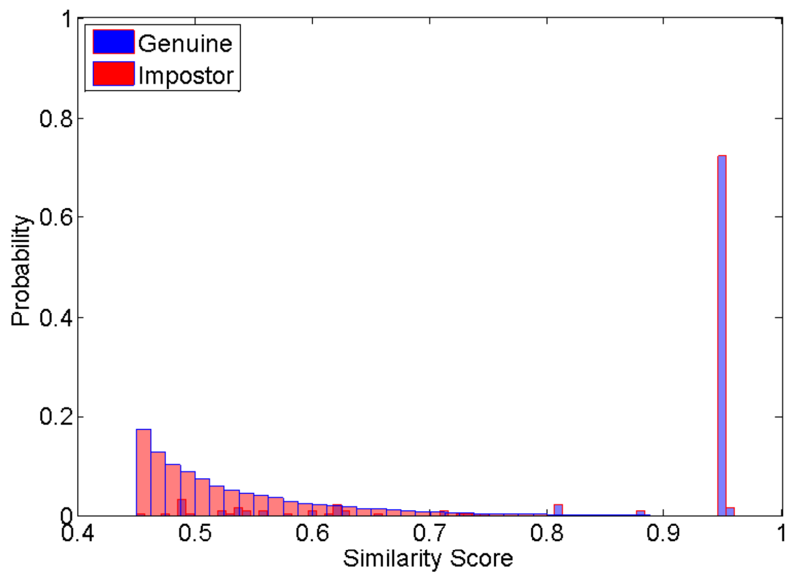

(b)

Figure 2.11 Genuine and impostor similarity score distributions (scaled to the same similarity score range) for the NIST SD27 database (a) before and (b) after applying feedback using the top 200 candidates retrieved by the baseline matcher (against a reference database of 100,000 exemplars). The overlap between the genuine and the impostor score distributions reduces by ˜25% after applying feedback.

(a) Latent 1 from NIST SD27 (b) Mated Exemplar of (a)

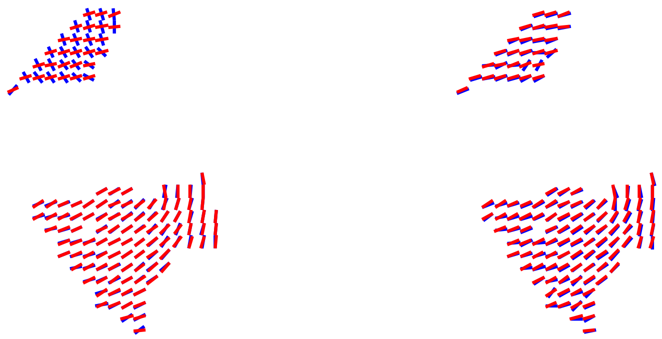

(c) Initial Orientation Field (d) Refined Orientation Field

Figure 2.12 Successful latent feature refinement via feedback for a latent in the NIST SD27 database. Shown in red is the exemplar orientation field and in blue is the initial and refined latent orientation field in (c) and (d), respectively. Note that the refined latent orientation field is closer to the exemplar orientation field compared to the initial latent orientation field. The rank of the mated exemplar of the latent in (a) improved from 49 to 16 amongst the 200 candidate exemplars returned by the baseline matcher after feedback.

2.5.4 Performance on NIST SD27 Database

The Cumulative Match Characteristics (CMC) curves shown in Figure 2.10a illustrate the performance of the baseline matcher [166] with and without feedback on the NIST SD27 database. Using the proposed ridge orientation and frequency feedback to refine the latent features improves the rank-1 identification accuracy improves by around 3.5%. Consistent accuracy improvement for all ranks is also observed. Figure 2.11 shows the genuine and impostor similarity score distributions before and after applying feedback. The overlap between the genuine and impostor distributions decreases by approx. 25% after applying feedback. Figures 2.12 and 2.13 shows two latents for

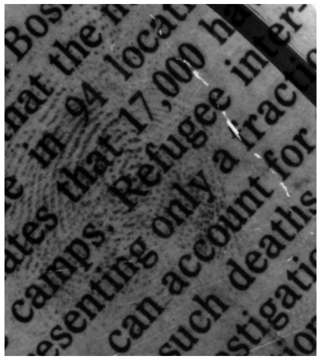

(a) Latent 2 from NIST SD27

(b) Mated Exemplar of (a)

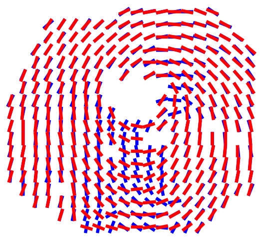

(c) Initial Orientation Field

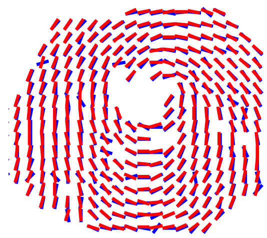

(d) Refined Orientation Field

Figure 2.13 Successful latent feature refinement via feedback for a latent in the NIST SD27 database. Shown in red is the exemplar orientation field and in blue is the initial and refined orientation field in (c) and (d), respectively. Note that the refined latent orientation field is closer to the exemplar orientation field compared to the initial latent orientation field. The rank of the mated exemplar of the latent (a) improved from 20 to 8 amongst the 200 candidate exemplars returned by the baseline matcher after feedback.

which the retrieval rank of the mated print is improved by applying ridge orientation and frequency feedback for the latent matcher in [166].

2.5.5 Performance on WVU Database

The Cumulative Match Characteristics curves (Figure 2.10b) for the WVU database also demonstrate the advantage of using the proposed feedback framework with the baseline matcher. Although there is a marginal decrease in the rank-1 identification accuracy, it is offset by the performance improvement of about 1-1.5% for the higher ranks. Note that the improvement is smaller


(a) Latent 1 from WVU


(b) Impostor Exemplar

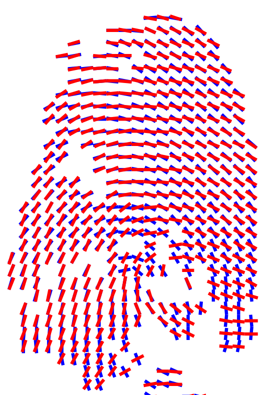
(c) Initial Orientation Field

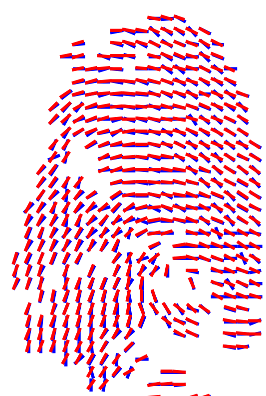
(d) Refined Orientation Field

Figure 2.14 Failure of feedback for a latent in the WVU database. Shown in red is the exemplar orientation field and in blue is the initial and refined orientation field in (c) and (d), respectively. The refined latent orientation field is closer to the exemplar orientation field compared to the initial latent orientation field. However, the retrieval rank of the mated exemplar degraded from 16 to 49 amongst the 200 candidate exemplars returned by the baseline matcher after feedback.

as compared to NIST SD27 because the contrast of latents in WVU is, in general, poor making it difficult to extract level one features in the frequency domain. Figure 2.14 shows an example where the retrieval rank of the mated print degrades after feedback for a latent.

The matching performance generally degrades when (i) the ridge structure of the impostor is similar to latent and (ii) the impostor exemplar is of better quality as compared to the true mate resulting in better quality features being extracted from the impostor.

2.5.6 Computational Complexity

The current implementation of the feedback paradigm uses local ridge orientation and ridge frequency features extracted at multiple peak points in the frequency representation of the latent image. To reduce the computational complexity, these features are computed only once for each query, and then used in matching against all exemplar candidates. Since the feedback mechanism does not involve the entire exemplar database but is used only to re-rank the top K candidates returned by the baseline matcher, the algorithmic complexity of the algorithm is $O(K)$.

The algorithm has been implemented in MATLAB and runs on a desktop system with Intel®Core$^{\text{TM}}$2 Duo CPU of 2.93 GHz and 4.00 GB of RAM with Windows 7 Operating system. For the NIST SD27 database, the average time to extract local orientation and frequency features for a latent is about 0.74 sec and the average time to match a latent against the top 200 candidates is about 4 sec. The extra computational cost incurred in matching the latent is worth the improvement in performance, especially in forensic applications which demand high latent matching accuracy.

2.6 Conclusions

Given the relatively poor quality of operational latent fingerprint images, feature extraction is one of the major challenges for a latent matching system. To deal with complex background noise in the latent, we propose incorporating feedback from exemplar (rolled or plain fingerprint) to refine feature extraction in latent with the eventual goal of improving the latent matching accuracy. We devise a method to use exemplar features (ridge orientation and frequency) for refining the latent features and then develop a feedback paradigm to use the refined latent features to re-sort the candidate list returned by a latent matcher. Experimental results show 0.5-3.5% improvement in the latent matching accuracy using the feedback mechanism. We also propose a global criterion to decide if feedback is needed for a latent query. A local quality based criterion is used to determine the regions in latent where it should be applied if needed and to identify reliable regions in exemplar for providing feedback.

Chapter 3

Crowd Powered Latent Fingerprint Matching: Fusing AFIS with Examiner Markups

3.1 Introduction

In the previous chapter, we presented a framework to improve the performance of automatic latent matching. Still, latent matching is an extremely difficult problem, particularly when the quality or information content of latents is inadequate. Most forensic agencies, therefore, follow a semi-automatic latent matching process, where a fingerprint examiner marks features on a latent, submits a query (image plus markup) to an AFIS, and subsequently reviews the top-K (usually K $= 20$ to 50) retrievals from the database to determine if the latent hit against a reference print. Although the practice of obtaining markups from fingerprint examiners increases the overall chances of obtaining a hit from the database [108], inaccurate feature markups can lead to mated reference prints being retrieved at a lower rank in the candidate list. This can, in turn, adversely impact the examiner decision process [86] [181]. The goal of this research is to harness the combined exper-

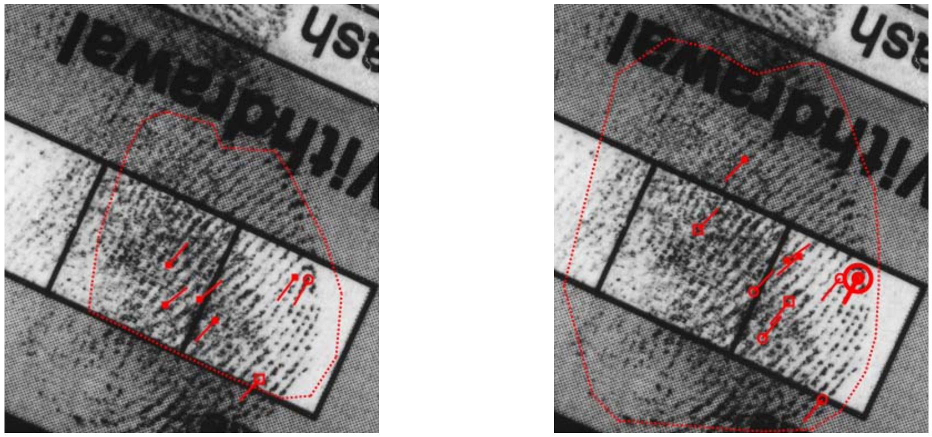

(a) (b)

Figure 3.1 Two markups (by two different examiners) for a latent image from 1000 ppi ELFT-EFS database. A state-of-the-art AFIS was unable to make a hit for the latent image in lights-out mode (score of 0 with the true mate in the reference database). However, feeding the AFIS with the markups shown in (a) and (b) resulted in the mated print being retrieved at rank-1 and rank-129, respectively.

tise of multiple fingerprint examiners and the AFIS to increase the likelihood of obtaining a hit at a higher rank from the reference database.

3.1.1 Semi-automatic Latent Matching: Advantages and Disadvantages

The NIST Evaluation of Latent Fingerprint Technologies, Extended Feature Sets (ELFT-EFS) 2 [108] reported that the likelihood of finding a hit in the reference database improves when an AFIS is provided with a markup[1](see Figure 3.1). The identification accuracy of the best AFIS operating in the lights-out mode[2] is reported to be 67.2% in identifying 1,066 latent prints against reference prints from 100,000 subjects. However, the above accuracy improves to 70.2% when the AFIS is fed with both the latent image and the extended feature set (EFS) markup provided by NIST.

The above performance gain, however, depends on the precision of the markup being fed to the AFIS [109]. Imprecise markups can result in the mated reference print being returned at a lower rank amongst the retrieved candidates [86] [181] compared to the image alone being fed to

[1]Markup, in this chapter, refers to the latent image with features marked by a fingerprint examiner.

[2]In the lights-out mode, AFIS automatically extracts features and compares the latent to the reference prints, without any human intervention.

the AFIS. Furthermore, markups for the same latent by different examiners can differ significantly and, consequently, different markups may lead to difference in identification performance of the AFIS (see Figure 3.1).

3.1.2 Proposed Crowd Powered Latent Matching Framework

To overcome the aforementioned limitations, we propose a latent matching framework where the AFIS and latent examiners[3] operate in synergy to improve the latent matching accuracy[4]. In this framework, a latent is first submitted to the AFIS to be matched in the lights-out mode. Based on the output of the AFIS, the likelihood that the AFIS hit against a reference print at rank-1 is determined using a variant of the criterion described in [56]. If the likelihood of the AFIS making a hit at rank-1 is low, the latent is crowdsourced to a pool of latent examiners for marking features. In this manner, the collective "wisdom" of several latent examiners is utilized to obtain multiple markups for a latent only when required. The manual markups are then used in conjunction with the AFIS for improving the latent matching accuracy.

The proposed framework is based on the conjecture that combining markups obtained from different examiners with the automated encoding of the AFIS can benefit the identification performance of the AFIS. The conjecture stems from the classic pattern recognition theory that a group of experts with diverse and complementary skills can collectively solve a difficult problem, on average, better than each individual expert [83] [100]. Each latent examiner, as well as the AFIS, can be viewed as an expert for latent markup. Because manual markups obtained from different latent examiners lead to different candidate lists being retrieved by the AFIS, their expertise is rather diverse. Thus, a combination of AFIS with examiner markups should boost the identification performance of the AFIS.

State-of-the-art AFIS typically generate multiple templates (encodings) from an input latent. These templates are then individually compared with the reference prints and the resulting compar-

[3]The term *latent examiner* is used to refer to a fingerprint examiner who is trained to analyze and compare latent prints.

[4]This work was published in the proceedings of the International Conference on Biometrics (ICB), 2015 [52].

ison scores are combined to generate a single candidate list. Our method can be viewed analogous to generating multiple templates, albeit based on feature markup by multiple latent examiners, and fusing them with the multiple templates internally generated by an AFIS.

To evaluate the proposed framework, we crowdsourced markups for the NIST Special Database 27 (NIST SD27) latents [18] to six certified latent print examiners affiliated to Michigan State Police. We also conduct experiments using two individual markups provided in the ELFT-EFS public challenge database [6] and one individual markup provided in the RS&A database [24]. We compute the efficacy of the proposed criterion to compute the likelihood that the AFIS makes a hit for the latent at rank-1. The proposed criterion is able to reduce the number of latents that need to be crowdsourced for manual markup from 258 to 151 for NIST SD27, from 255 to 151 for ELFT-EFS database, and from 200 to 35 for RS&A database without impacting the overall hit rate. Our experimental results on a reference database of 250,000 rolled prints show that by fusing the scores from lights-out comparison with the scores obtained using the examiner markups, the rank-1 identification accuracy of the AFIS improves by 7.75% on 500 ppi NIST SD27 (using six markups), by 11.37% on 1000 ppi ELFT-EFS database (using two markups), and by 2.5% on 1000 ppi RS&A database. Our experimental results indicate that markups obtained from different latent examiners contain complementary information which, in turn, helps to boost the identification performance of an AFIS.

The contributions of this chapter are:

- A systemic way to combine the AFIS with examiner markups to boost the latent hit rate,
- A crowd powered latent matching framework where a latent is crowdsourced to a pool of examiners for obtaining multiple markups,
- A criterion to automatically determine when crowdsourcing is required, and
- A method to dynamically determine how many crowd experts are needed.

3.2 Collective Wisdom of Multiple Examiners

Harnessing the "collective wisdom" of the crowd is a commonly used methodology for performing relatively simple tasks (e.g., image labeling, product recommendations). For instance, recommendation systems in Netflix[5] and Amazon[6] use the collective preferences of a large number of customers when recommending movies or products to a specific customer. Expert crowdsourcing is another concept which has recently gained prominence [168] [191]. This involves dynamically assembling a team of expert crowd workers for accomplishing specialized tasks. We extend these concepts to latent fingerprint matching in the following manner.

Given a latent, an AFIS operating in lights-out mode is first used to compare it to reference prints in the background database. Based on the score distribution of the top-K candidate matches output by the AFIS, we ascertain whether manual markup is needed to boost the identification performance. If it is determined that manual markup is needed, the latent markup is crowdsourced to a pool of latent examiners. The obtained markups are input to AFIS individually to generate multiple scores for each reference print in the database. These individual markup and lights-out scores are then fused to boost the identification accuracy of the AFIS[7] (see Figure 3.2).

3.2.1 Expert crowdsourcing framework

Let a query latent image be denoted by I_L, and the set of reference print images in the database be denoted by I_R. Let the total number of reference prints in the database be N, and the i^{th} reference print be denoted by $I_R(i)$. The latent I_L is compared against the set of reference prints I_R using an AFIS operating in lights-out mode to generate a set of similarity scores S_{LO}:

$$S_{LO}(i) = S(I_L, I_R(i)); \forall i = \{1, 2, \ldots N\}. \tag{3.1}$$

[5]http://www.netflix.com

[6]http://www.amazon.com/

[7]Rank-level fusion was also investigated for fusing the lights-out identification results with the identification results obtained for different markups. However, score-level fusion outperformed rank-level fusion in our experiments.

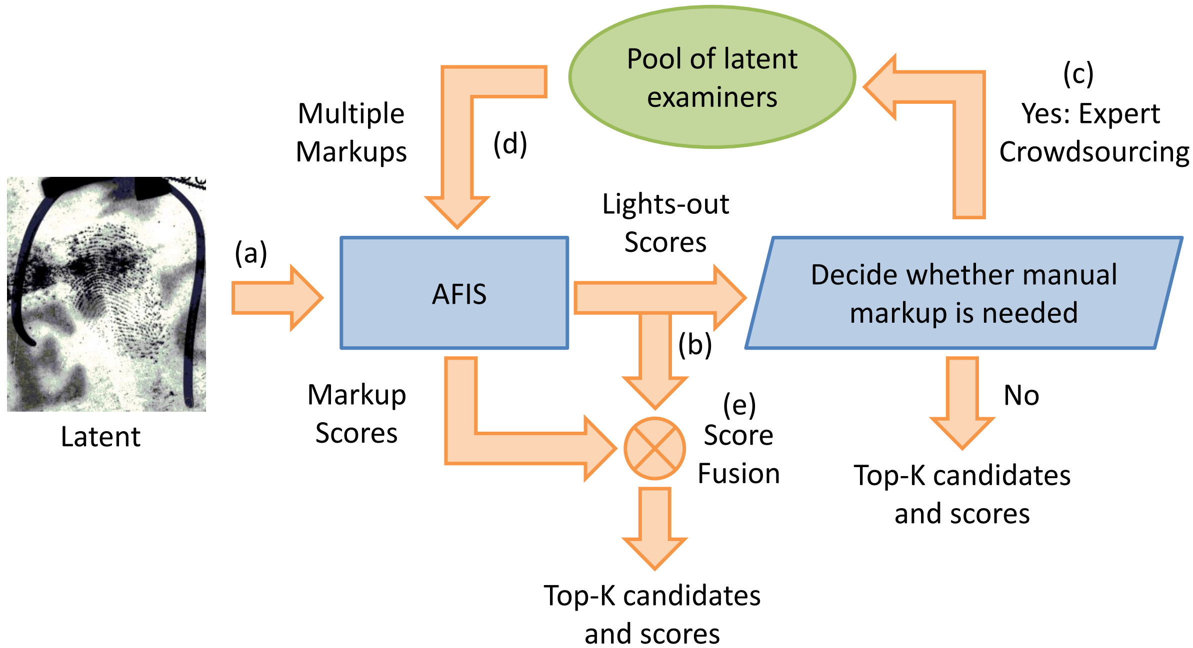

Figure 3.2 The proposed crowd powered latent fingerprint matching framework. (a) Latent is fed to an AFIS, (b) it is determined whether manual markup is needed, (c) markups are obtained via expert crowdsourcing, (d) multiple markups are fed to the AFIS, and (e) AFIS scores in (b) are fused with the multiple markup scores in (d).

where $S(I_L, I_R(i))$ is the similarity between I_L and $I_R(i)$ output by the AFIS.

A parametric probability distribution model is fit to the distribution of the top-K scores from the set S_{LO}, and a variant of the method described in [56] is used to ascertain whether manual markup is required (see Section 3.2.2). If it is determined that manual markup is not required, the set of top-K candidates and their corresponding scores are directly output for validation by a latent examiner. Otherwise, the latent image I_L is crowdsourced to a pool of latent examiners for providing manual markups.

Let P be the number of examiners that provide manual markups. Denote these markups as I_M, where the j^{th} markup is $I_M(j)$. Each of the P markups are individually input to the AFIS to obtain similarity scores against the set of reference prints I_R,

$$S_{Mj}(i) = S(I_M(j), I_R(i)); \quad (3.2)$$
$$\forall j = \{1, 2, \dots, P\}, \forall i = \{1, 2, \dots, N\}.$$

Here $S_{Mj}(i)$ denotes the similarity score by comparing the j^{th} latent markup to the i^{th} reference print. Finally, we fuse the lights-out scores S_{LO} with the similarity score of each markup S_{Mj} for every reference print to obtain a combined score S_F,

$$S_M(i) = \otimes\{S_{Mj}(i)\}, \quad (3.3)$$
$$\forall j = \{1, 2, \dots, P\}, \forall i = \{1, 2, \dots, N\};$$
$$S_F(i) = S_{LO}(i) \otimes S_M(i); \forall i = \{1, 2, \dots, N\}. \quad (3.4)$$

Here, $\otimes$ is the score fusion operator, and S_M denotes the score obtained by fusing the scores of the P different markups. The top-K fused scores from the set S_F, and the corresponding candidates based on the fused scores are then output to the latent examiner for evaluation.

3.2.2 When to crowdsource?

Although expert crowdsourcing has its advantages, crowdsourcing every latent to a pool of latent examiners is costly in terms of time and effort. If it can be established that the likelihood of AFIS making a hit at rank-1, for a given latent, is fairly high, then expert crowdsourcing is not utilized for that latent. While latent quality can be an indicator of this likelihood, to our knowledge, there is no existing satisfactory indicator of latent quality [186]. Therefore, we base our decision on the order statistic of the top-K candidate scores returned by the AFIS [56].

Let the set of top-K scores returned by the the AFIS be denoted as $X = \{X_{(1)}, X_{(2)}, \dots X_{(K)}\}$ where $X_{(i)}$ denotes the rank-i score. An exponential distribution model is fit to the set X. A hypothesis test is conducted to determine whether there is an upper outlier present in the distribution of the top-K scores. The null hypothesis (H_0) and the alternative hypothesis (H_1) are defined as follows:

H_0: All scores in the set X are i.i.d from an exponential distribution.

H_1: Rank-1 score $X_{(1)}$ is an upper outlier of the score distribution.

The test statistic Z for testing H_0 against H_1 is defined as:

$$Z = \frac{X_{(1)} - X_{(2)}}{S_K};\ S_K = \sum_{i=1}^{K} X_{(i)}. \tag{3.5}$$

The critical value of the test $z(\alpha)$ at significance level α is:

$$z(\alpha) = 1 - \alpha^{\frac{1}{K-1}}. \tag{3.6}$$

The value of the test statistic $Z = z$ should be greater than the critical value $z(\alpha)$ when rank-1 score $X_{(1)}$ is an outlier. Thus, we define an indicator random variable I_C which takes the value 1 when expert crowdsourcing is needed, and 0 when it is not needed:

$$I_C = \begin{cases} 0, & z > z(\alpha), \\ 1, & \text{otherwise} \end{cases} \tag{3.7}$$

In other words, if the rank-1 score is indeed an upper outlier, we are sufficiently confident that lights-out identification retrieved the mated reference print at rank-1. Therefore, the query latent does not need markups from latent examiners.

3.2.3 How many experts are enough?

A priori information about latent examiners (e.g., years of experience, the number of cases solved) is often known and can be utilized while crowdsourcing latent markup. Assume that the latent examiners can be rated based on such prior information. When additional markup is required for a latent, instead of crowdsourcing the latent to every examiner, it can be first sent to the best

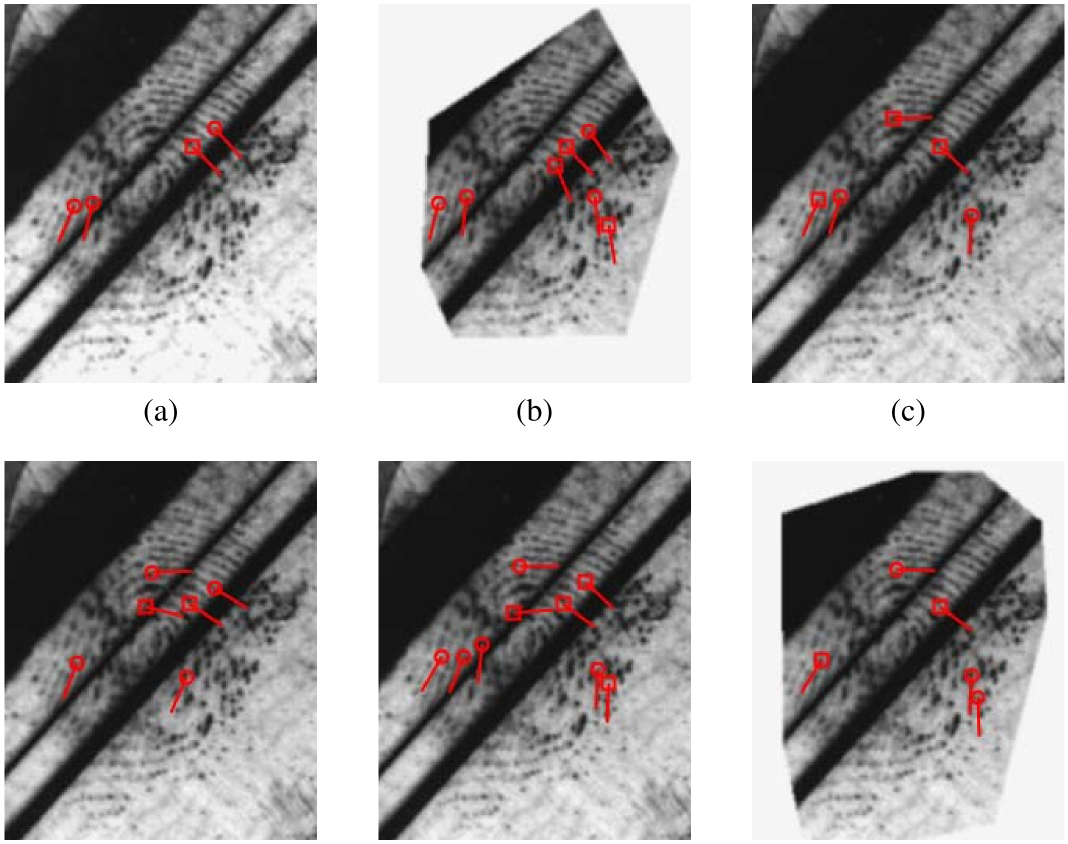

(a) (b) (c) (d) (e) (f)

Figure 3.3 Markups by six different latent examiners for a latent image in the 500 ppi NIST SD27.

examiner to obtain a markup. The best examiner's markup can then be fused with the lights-out AFIS, and the decision whether additional markup is needed made. Subsequently, the latent can be sent to the next best examiner, if required. Such a greedy (sequential) strategy can dynamically determine the number of examiners needed for providing markups, in turn, reducing the required cost and effort [125].

3.3 Experimental Details

A state-of-the-art AFIS, which was one of the top performing AFIS in the NIST ELFT-EFS 2 evaluation [108], is used for conducting all identification experiments.

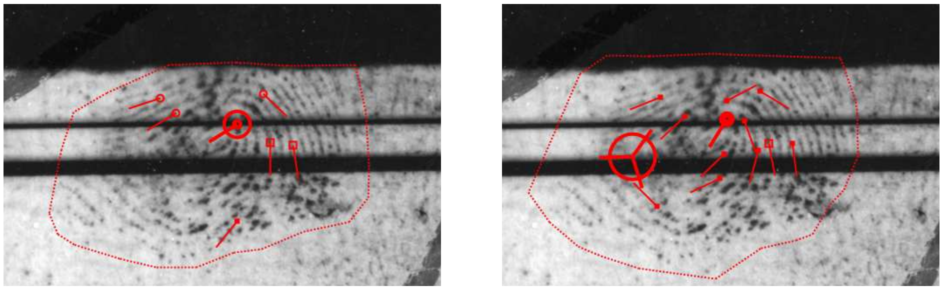

(a) (b)

Figure 3.4 Markups by two examiners for a latent in the 1000 ppi ELFT-EFS public challenge database.

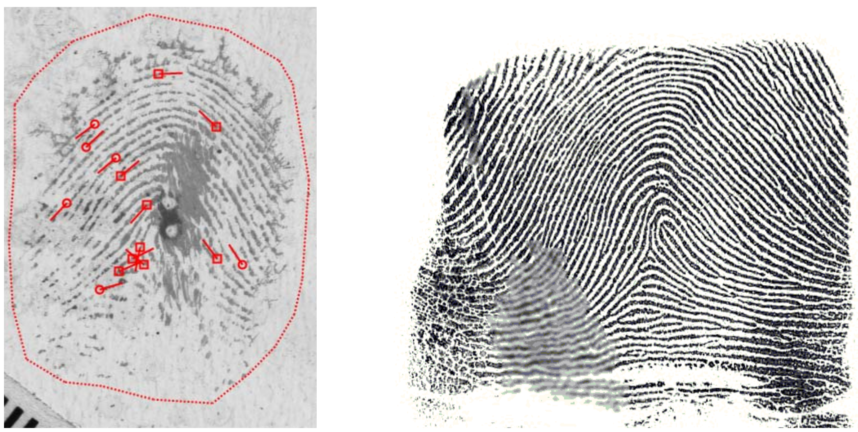

(a) (b)

Figure 3.5 Markup for a latent image (a) in the 1000 ppi RS&A database. The mated reference print of the latent is shown in (b).

3.3.1 Databases

The proposed latent markup crowdsourcing framework is evaluated on three different latent databases (summarized in Table 3.1), the NIST SD27 [18], ELFT-EFS [6] and the RS&A [24]. In addition to the mated reference prints of the latents available from these databases, we use rolled prints, provided by the Michigan State Police (MSP), to enlarge our reference database to 250,000 rolled prints for all the experiments reported here. The rolled prints provided by MSP have similar characteristics to the mated reference prints provided with the three latent databases.

Table 3.1 Summary of the latent databases used.

Database	#Latents	Resolution	Latent Type	#Markups
NIST SD27	258	500 ppi	operational	6*
ELFT-EFS**	255	1000 ppi	operational	2*
RS&A	200	1000 ppi	collected in lab	1

*The scope of this research is to investigate how best to combine independent markups. Therefore, juried markups, although available, are not used because they involve the expertise of multiple examiners. ** ELFT-EFS database contains 255 latents from NIST SD27 rescanned at 1000 ppi.

Table 3.2 Number of latents markups provided by each of the six examiners (out of 258) for the NIST SD27 latents.

Examiner	1	2	3	4	5	6
No. of markups	253	255	255	255	253	257

3.3.2 Latent Markup

Independent feature markups for NIST SD27 latents were obtained from six certified latent print examiners affiliated to Michigan State Police. The average feature markup time is about 5 min. per latent (around 20 hours for all 258 latents). Examiners were specifically asked to mark minutiae, ridge counts between minutiae and/or region of interest (ROI) on the latents. However, not all examiners marked all 258 latents (see Table 3.2). Figure 3.3 shows sample markups obtained from the six examiners for a latent in NIST SD27. Some examiners marked ROI while others did not. For each latent in the ELFT-EFS database, at least two independent feature markups are available with the database. Standard EFTS-LFFS feature markups (minutiae, ridge counts between minutiae, singular points and ROI) are used in our experiments. Note that latent examiners, in general, do not mark extended features on a latent because it is a challenging (ambiguous) and time consuming process. Hence, our experiments are in accordance with the general markup protocol being followed by examiners in law enforcement agencies. Figure 3.4 shows sample markups for a latent from the ELFT-EFS database. Only a single markup is available in the RS&A database [24] which is utilized in our experiments (Figure 3.5).

3.3.3 Experiments

To evaluate the efficacy of the proposed expert crowdsourcing framework, we perform the following set of experiments[8].

3.3.3.1 Lights-out Matching

The Cumulative Match Characteristic (CMC) curves of the AFIS in the lights-out mode on NIST SD27 are marked as Image only in Figure 3.6 (a). The rank-1 identification accuracy is 64.34%. Notice the reduction in identification performance of the AFIS on bad and ugly quality latents as compared to the good quality latents in the NIST SD27 (Figures 3.6 (b)-(d)).

Figure 3.7 (Image only) shows the CMC curves for lights-out identification on ELFT-EFS database. The rank-1 identification rate is 65.10%. Figure 3.8 (Image only) shows the CMC curve for lights-out identification on the RS&A database. The rank-1 identification accuracy obtained on the RS&A database is 87.50%. This is much higher than the accuracy obtained on the NIST SD27 and ELFT-EFS databases because the latents in the RS&A database were collected in a laboratory and are comparatively of better quality.

3.3.3.2 Matching Individual Examiner Markups

The Image plus Markup performance band in Figure 3.6 (a) indicates the identification accuracy of the AFIS on the NIST SD27 when fed with individual 500 ppi markups. The best rank-1 identification accuracy obtained using an individual markup is 66.67%. Note that the lights-out performance is within the performance band of the examiners. As expected, the identification accuracy is higher for good quality latents, compared to the bad and ugly quality latents (Figures 3.6 (b)-(d)).

Figure 3.7 shows the performance of the AFIS when fed with 1000 ppi markups available for the ELFT-EFS database. The best individual rank-1 identification accuracy obtained is 72.16%.

[8] Open set experiments are planned for subsequent studies

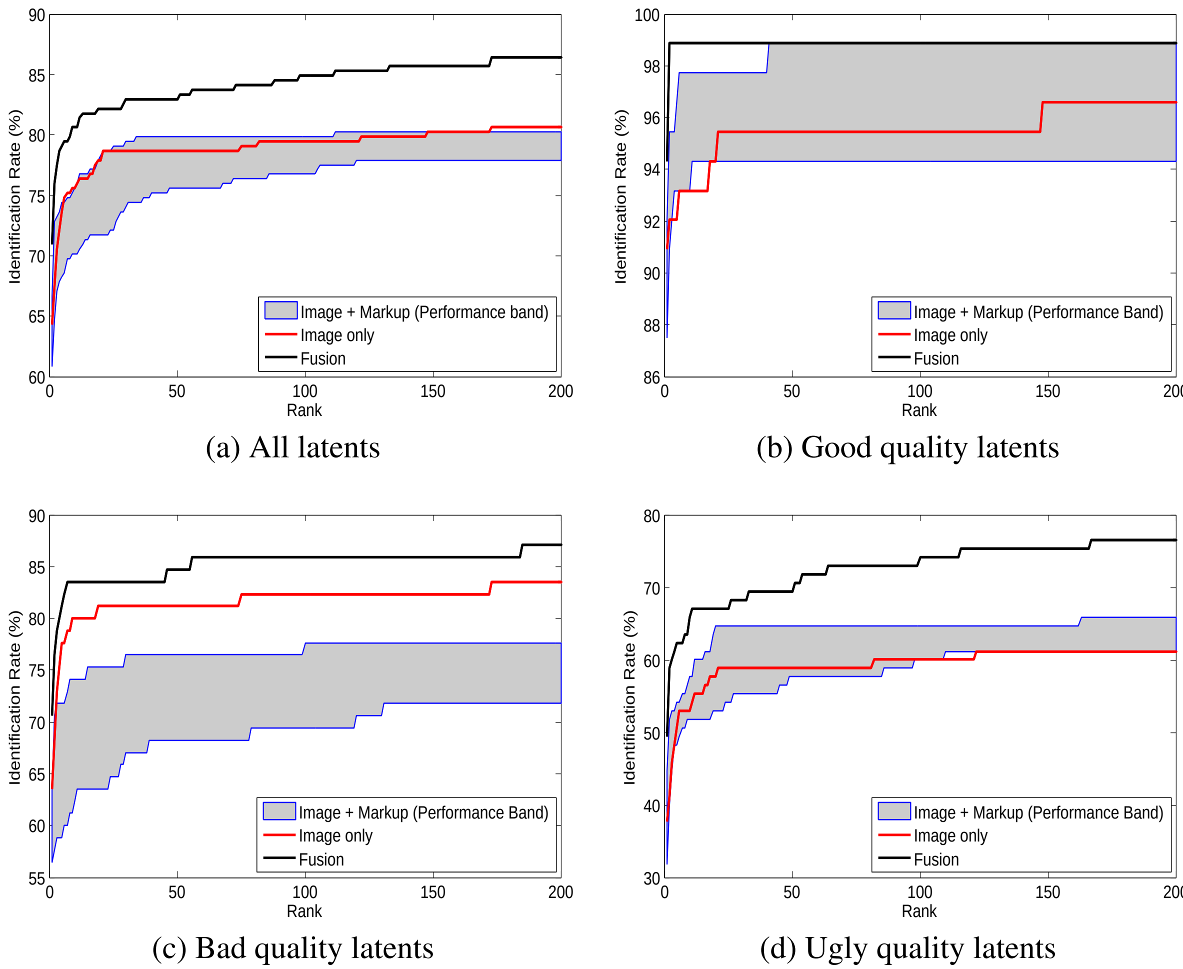

(a) All latents

(b) Good quality latents

(c) Bad quality latents

(d) Ugly quality latents

Figure 3.6 Identification performance (CMC curves) of the AFIS on NIST SD27 when (i) operating in lights-out mode (Image only), (ii) fed with markup from a single examiner (Image + Markup), and (iii) fusion of lights-out and 500 ppi markups from all six examiners (Fusion) for (a) all 258 latents, (b) 88 good quality latents, (c) 85 bad quality latents, and (d) 85 ugly quality latents. The size of the reference database is 250K rolled prints, including the true mates of latents from NIST SD27. The performance band of the latent examiners indicates the maximum and minimum accuracy obtained using an individual examiner markup at different ranks.

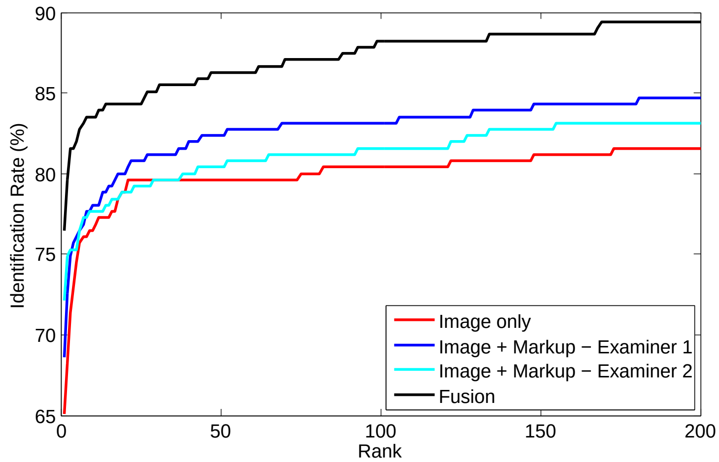

Figure 3.7 Identification performance (CMC curves) of the AFIS when (i) operating in lights-out mode (Image only), (ii) fed with an individual 1000 ppi markup (Image + Markup), and (iii) fusion of lights-out AFIS scores with the scores obtained using the two 1000 ppi markups (Fusion) for all 255 latents in the ELFT-EFS database against a reference database of 250K rolled prints.

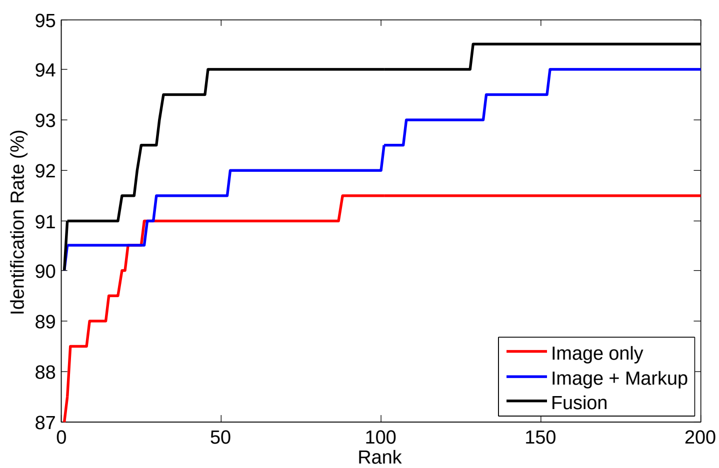

Figure 3.8 Identification Performance (CMC curves) of the AFIS when (i) operating in lights-out mode (Image only), (ii) fed with the single available markup (Image + Markup), and (iii) fusion of lights-out with examiner markup (Fusion) for the 200 latents in the RS&A database against a reference database of 250K rolled prints.

Table 3.3 Identification accuracy (%) of the AFIS, on average, on the NIST SD27 against 250K reference prints when fed with markups from different subsets of latent examiners.

Combination	Rank-1	Rank-50	Rank-100
One examiner	63.11	77.13	78.23
Two examiners	68.04	80.88	81.96
Three examiners	69.42	82.15	83.29
Four examiners	70.00	82.71	83.98
Five examiners	70.80	83.14	84.56
All six examiners	70.93	82.95	84.88

On the RS&A database, on the other hand, the rank-1 identification accuracy obtained using the single available markup is 90% (Figure 3.8).

3.3.3.3 Fusing Multiple Examiner Markups

Since we have six different markups available for the NIST SD27 latents, we fuse the scores obtained using different markup combinations, and then compute the average accuracy of the AFIS when fed with different subsets of examiner markups. Several different score level fusion strategies were investigated. Simple sum fusion rule provided the best performance. No score normalization is necessary here since all the scores are being generated by the same AFIS. Table 3.3 shows that while identification performance of the AFIS improves with additional markups, there is a saturation after 3 or 4 markups per latent. For the NIST SD27 with 258 latents, each 1% improvement in performance, say at rank-1, corresponds to roughly two or three latents being promoted to rank-1.

3.3.3.4 Fusing lights-out AFIS with Multiple Markups

The CMC curves plotted in Figure 3.6 show that the rank-1 identification accuracy of the AFIS increases by 7.75% on the NIST SD27 by fusing the scores obtained using the six markups with the scores obtained from lights-out identification. On the other hand, a performance improvement of 11.37% is observed when fusing the scores obtained from the two individual markups for the

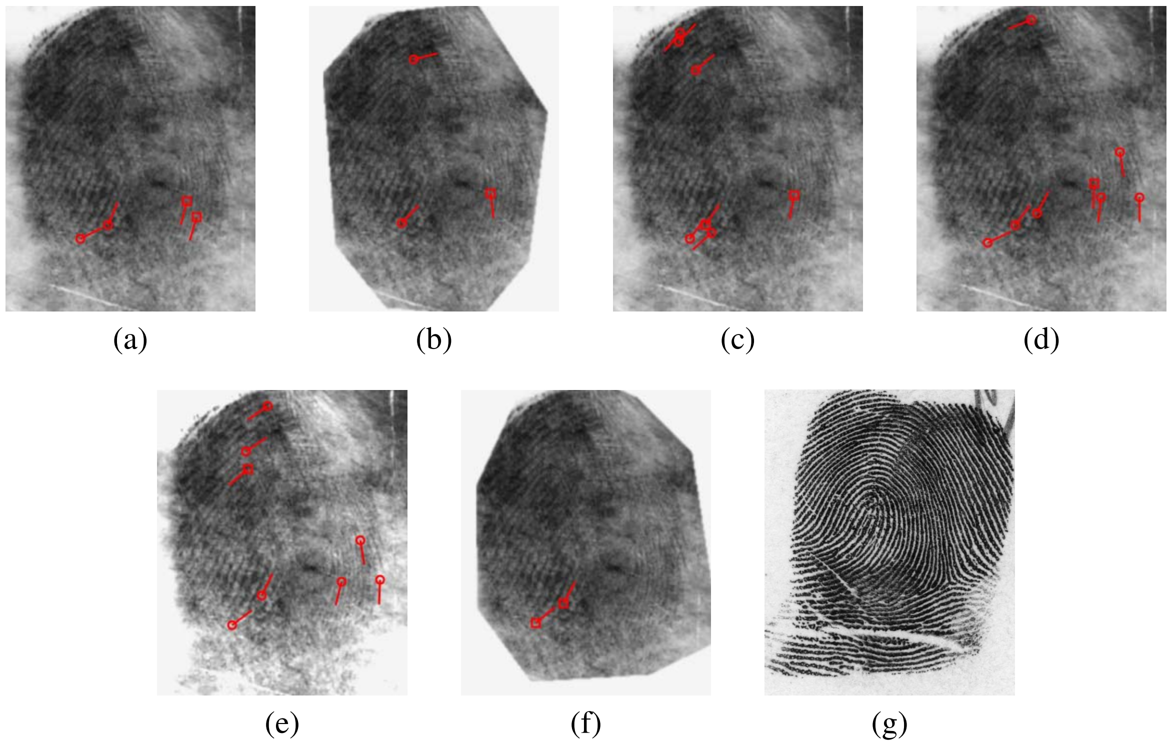

Figure 3.9 An example latent for which the mated reference print is retrieved at a higher rank after fusing the six crowdsourced markups with the AFIS. In the lights-out mode, the AFIS could not match the latent to the mated print shown in (g) (score=0). The rank of the mated print using the individual markups by the six examiners shown in (a)-(f) is 80, - (score=0), 45, 7, 57 and 12971, respectively. The mated print is retrieved at rank-2 using the combination of the AFIS with the six markups.

ELFT-EFS database with the lights-out scores. Figures 3.9 and 3.10, respectively, show an example of a successful and failure case using fusion of the AFIS with the examiner markups.

For the RS&A database, although fusion of lights-out match scores with markup scores does not seem to benefit in terms of the rank-1 identification accuracy in comparison to only using the manual markup, significant performance improvement is observed for higher ranks (see Figure 3.8).

3.3.3.5 Determining the need for crowdsourcing

To measure the efficiency of the test based on order statistic for determining the need for crowdsourcing manual markup, we compute the (i) number of latents where markup is not needed and

Table 3.4 Number of latents where markup is required, markup is not required when mated reference print is not at rank-1, and markup is required despite the mated reference print being retrieved at rank-1 for NIST SD27 (NIST27), ELFT-EFS (ELFT), and RS&A (RSA) databases. The number of latents in these three databases is 258, 255, and 200, respectively.

Significance level (α)	**#Latents requiring markup**			**#Latents not requiring markup when mated reference print is not at rank-1**			**#Latents requiring markup when mated reference print is at rank-1**		
	NIS27	ELFT	RSA	NIST27	ELFT	RSA	NIST27	ELFT	RSA
0.01	166	166	46	0	0	2*	74	74	22
0.05	151	151	35	0	0	2*	59	59	11
0.1	137	137	33	0	0	2*	45	45	9

*The mated reference prints are incorrectly labelled for these latents; does not impact the accuracy of the AFIS.

the mated print was not retrieved at rank-1, and (ii) number of latents where markup is ascertained but the mated print was retrieved at rank-1 (Table 3.4). The value of K used here is 200. For case (i) we found that the rank of the mated print did not decrease after fusion of lights-out with markup scores. This demonstrates the efficacy of the order statistic based test.

3.3.3.6 Greedy crowdsourcing

To test the benefit of using the greedy sequential strategy to dynamically determine the number of examiners required, we rated the individual examiners based on their skill set. This was estimated based on the AFIS performance obtained on the markups they provided. Figure 3.11 shows performance improvement when individual examiners are selected in decreasing order of their skill set. After fusing the three markups from the top three examiners, additional markups have negligible impact on the overall identification accuracy. Also, utilizing more number of markups does not necessarily improve the overall accuracy. Overall, 151 latents in the NIST SD27 require examiner markups based on the lights-out AFIS results (at a significance level of 0.05). 137, 131, 126, 126, 124, and 123 latents need markups after fusion of lights-out AFIS with best-1, best-2, best-3, best-4, best-5, and all six examiner markups, respectively.

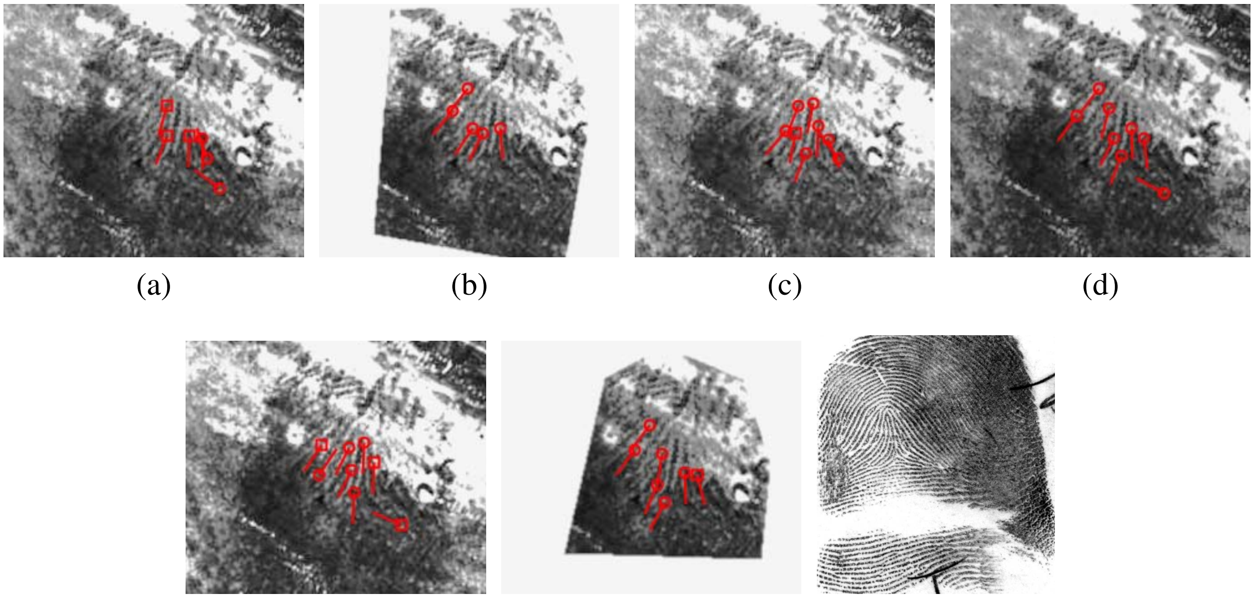

Figure 3.10 An example latent for which the mated reference print is retrieved at a lower rank after fusing the crowdsourced markups with the AFIS. In the lights-out mode, the AFIS retrieved the mated print shown in (g) at rank-1. The rank of the mated print in (g) using the individual markups by the six examiners shown in (a)-(f) is 54, 1171, 3426, 595, 22 and 8450, respectively. The mated print is retrieved at rank-26 using the combination of the AFIS with the six markups.

3.4 Conclusions

Matching poor quality latents to reference prints is one of the most challenging problems in fingerprint recognition. In order to match latents to reference prints with high accuracy, we propose a crowd powered latent matching paradigm which involves a symbiosis of fingerprint examiners with AFIS. Given a latent print, it is first compared against reference prints using an AFIS. Based on the output of the lights-out match, an automatic decision is made to determine if manual feature markups from latent experts would be beneficial. If it is determined that additional markup would help, the latent print is crowdsourced to a pool of latent examiners. The manual feature markups are fed to the AFIS and the comparison scores from lights-out AFIS and those from manual markups input to AFIS are combined to boost the identification accuracy. Experimental results obtained on three different latent databases (NIST SD27, ELFT-EFS and RS&A), against a reference database

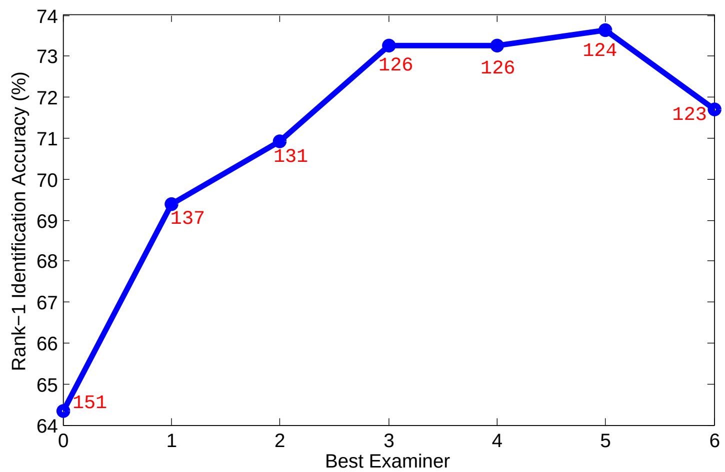

Figure 3.11 Identification accuracy of the AFIS using greedy crowdsourcing for the 258 NIST SD27 latents. Starting with the best examiner, a significance level of 0.05 is used to decide if markup from the next best examiner is needed. Numbers of latents given to the next best examiner are indicated in red. Due to the preponderance of low quality prints in NIST SD27, the rank-1 identification accuracy tapers off after three examiner markups.

of 250,000 rolled prints, demonstrate that a significant performance improvement can be obtained using the proposed crowd powered framework.

Chapter 4

Design and Fabrication of 3D Single-Finger Targets

4.1 Introduction

Until about 20 years ago, forensic labs and law enforcement agencies were the primary consumers of fingerprint recognition technology with fingerprints being utilized to identify repeat offenders and to associate a crime to criminal(s). In chapters 2 and 3, we developed methods to address one of the most important problems faced by these agencies, namely matching latent fingerprints commonly encountered in crime scenes to legacy rolled and slap fingerprint databases. However, the recent past has witnessed large scale deployments of fingerprint recognition technology in civilian, commercial and personal applications, e.g., the Aadhaar program to uniquely identify each resident of India [38], the United States' Office of Biometric Identity and Management's program (formerly US VISIT) to prevent illegal immigrants and criminals from entering the country [20], and the TouchID system to unlock Apple smartphones and make online payments [36]. Given this rapid growth in large scale deployments of fingerprint identification systems, it is essential to have a reasonable estimate of their matching performance and robustness in the operational settings.

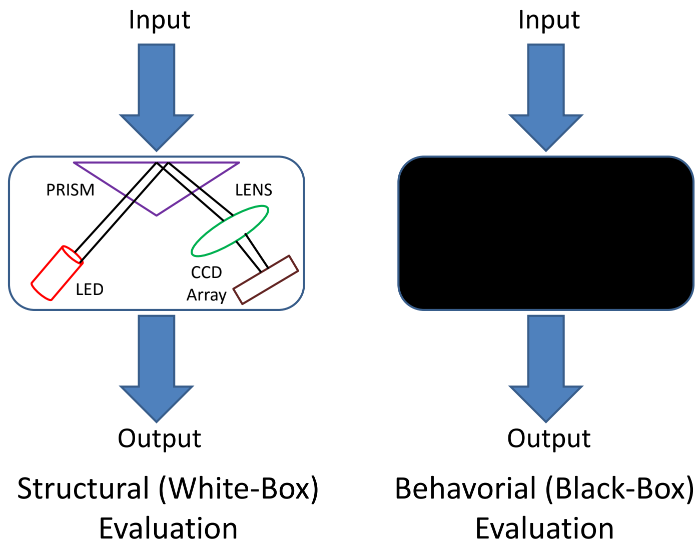

Figure 4.1 Structural (White-Box) v. Behavorial (Black-Box) evaluation of fingerprint readers. In structural evaluation, details of the internal setup of the reader are known and reader component assembly operation is tested. On the other hand, in behavorial evaluation, the internal details of the reader are not known and only functionality of the reader is tested based on its input and output.

For thorough evaluation of fingerprint systems, a large number of representative fingerprint images from the operational scenario are needed. Collecting such a large number of fingerprint images with different characteristics from human subjects is both expensive and tedious. Biometric synthesis provides a solution to this problem. A large number of 2D fingerprints can be generated using 2D synthetic fingerprint generators [67] [192] that can be utilized for evaluating fingerprint feature extractors and matchers. However, they cannot be used for assessment of fingerprint readers.

Standard calibration targets are typically used for structural evaluation[1] of fingerprint readers, e.g., measuring their geometric accuracy, distortion and resolution. One limitation of these targets though is that they cannot be used for behavorial evaluation[2] of the readers in the operational settings (see Figure 4.1). Furthermore, these targets are not suitable for "end-to-end" evaluation of fingerprint recognition systems from fingerprint acquisition to feature extraction and matching.

[1]Structural or white-box evaluation tests how internal system components and component sub-assemblies should operate, and requires technical knowledge of the system [59].

[2]Behavioral or black-box evaluation tests functions supported by the system in the operational or deployment scenario by focusing on the input and output of the system [59].

(a) (b) (c)

Figure 4.2 Examples of imaging phantoms used in medical imaging: (a) Phannie, a phantom to calibrate MRI machines developed at NIST [14], (b) a phantom hand used for evaluating X-ray machines [41], and (c) a torso phantom used to calibrate CT-Scan machines [34].

This is because the process of user interaction with the reader leading to fingerprint capture cannot be mimicked using these targets. In this chapter, we propose to generate 3D targets for behavioral evaluation of fingerprint readers in operational settings.

4.1.1 Structural Evaluation of Fingerprint Readers

As mentioned in the earlier section, structural (white-box) evaluation of imaging systems is generally done using specially designed objects with known properties, called *targets*. In the biomedical domain, for instance, such objects (called *phantoms*) are used for calibrating and testing optical measurement profiles of sensing instrumentation [180], [60] (Figure 4.2). Similarly, targets (Figure 4.3) have also been used for calibration of fingerprint readers.

There are two separate standards currently in use by the Federal Bureau of Investigation (FBI) for the certification of fingerprint readers, (i) the *PIV*, which caters to single-finger readers designed for applications involving person verification (one-to-one comparison), and (ii) the *Appendix F*, which applies to fingerprint readers designed for use in large scale applications involving person identification (one-to-many comparisons) [8]. To get their fingerprint readers certified, fingerprint vendors need to demonstrate that the images captured using their readers meet the image quality specifications laid out in the relevant standard [155] [156]. A typical procedure is (i) to use 2D/3D calibration targets to ascertain if the images of the targets captured using the reader meet the spec-

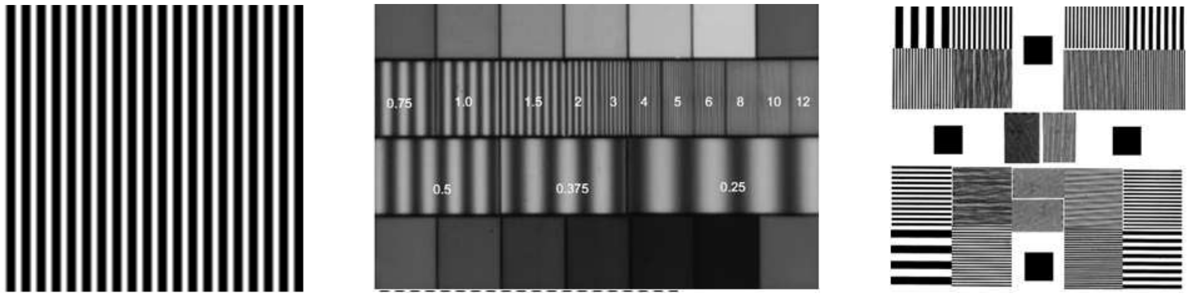

(a) (b) (c)

Figure 4.3 2D images of standard targets used for calibrating fingerprint readers, (a) ronchi (vertical bar) target for calibrating the geometric accuracy, (b) sine wave target for measuring the resolution, and (c) multiple bar target for estimating the spatial frequency response of a fingerprint reader (images taken from [155]).

ifications, (ii) modify the reader configuration, if needed, to ensure it captures images of sufficient quality to meet the specifications, and (iii) when satisfied with the reader configuration, submit test images to the testing agency for review[3] [8]. If the test data is found to meet the desired specifications, the testing agency certifies the fingerprint reader as being compliant with the specific standard.

4.1.2 Behavioral Evaluation of Fingerprint Readers

Standard calibration targets (see Figure 4.3) are used for structural evaluation of fingerprint readers. For example, the targets in [33] are utilized for testing frustrated total internal reflection (FTIR) components (LED, glass prism and platen assembly) of an optical fingerprint reader. However, these targets are not suitable for behavioral (black-box) evaluation of a fingerprint reader in the presence of operational variations (e.g., finger placement and pressure etc.) when users interact with the reader. This is because these targets are not specifically constructed using materials with properties (e.g., hardness and elasticity) similar to the human finger skin.

[3] Review of the submitted test data is conducted by the Technology Evaluation Standards Test Unit, a part of the FBI's Biometric Center of Excellence (BCOE) led by the Criminal Justice Information (CJI) Services Division [9].

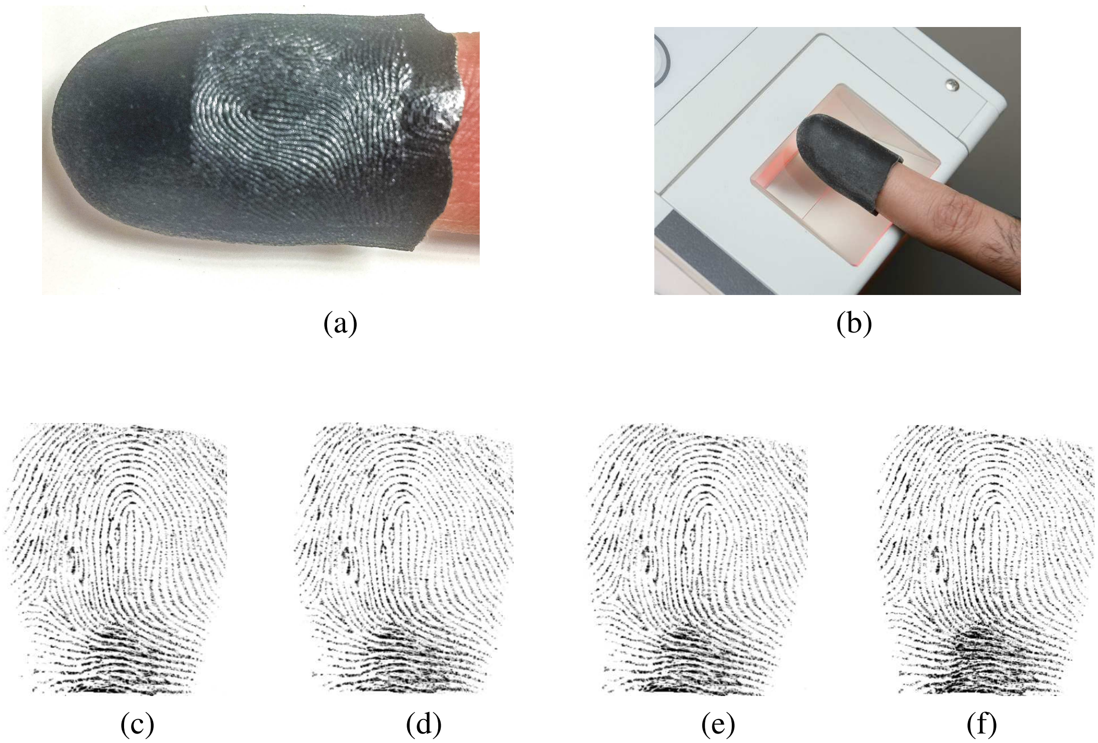

Figure 4.4 Evaluating a single-finger optical fingerprint reader using the 3D targets designed and fabricated by the authors. (a) The 3D target is worn on a finger, (b) the finger is placed on the fingerprint reader platen, and (c)-(f) multiple 2D impressions (four shown here) of the 3D target are captured to evaluate the reader.

4.1.3 3D Targets for Behavioral Evaluation

For behavioral evaluation of a fingerprint reader, one possibility is to conduct pilot studies involving human subjects in the field using the reader. This, however, is a tedious process both in terms of time and resource commitment, and is limited by the amount and possible variations in the fingerprint data that can be collected. Besides, such a procedure cannot be used for repeatable behavioral evaluation of the fingerprint reader because, in practice, the same set of subjects is typically not available for repeat testing. The goal of this research, therefore, is to fabricate standard 3D targets which can be used for repeatable behavioral evaluation of fingerprint readers. We fabricate 3D targets with material similar in hardness and elasticity to the human finger skin such that they can be worn on a finger and placed on the fingerprint reader platen in a natural manner (see Figure 4.4)[4].

[4]This work was published in IEEE Transactions on Information Forensics and Security (TIFS), 2016 [54].

Table 4.1 Comparison of prevailing 2D synthetic fingerprint based evaluation methods with the proposed 3D target generation method.

Method	**Artifacts***	**Fingerprint Features**	**Evaluation Use Cases**
SFinGe [67]	2D synthetic fingerprints (electronic)	Known fingerprint ridge flow and ridge density features; uncontrolled minutiae placement	Fingerprint feature extractors and matchers
IBG DHS SBIR [105]	2D synthetic fingerprints (electronic)	Known fingerprint ridge flow and ridge density features; partially controlled minutiae placement	Fingerprint feature extractors and matchers
Zhao et al. [192]	2D synthetic fingerprints (electronic)	Known fingerprint ridge flow, ridge density and minutiae placement	Fingerprint feature extractors and matchers
NIST**	3D targets (electronic and physical)	Known calibration pattern features	Contactless 3D fingerprint readers
Proposed	3D targets (electronic and physical)	Known fingerprint ridge flow, ridge density and minutiae placement	End-to-end fingerprint systems, including fingerprint readers, feature extractors and matchers

*The term *electronic* is used for digitally generated artifacts, whereas the term *physical* is used for physically fabricated artifacts from electronic artifacts. **This research is currently underway at NIST and has not been published yet.

The utility of the fabricated 3D targets extends beyond behavioral evaluation of fingerprint readers. 3D targets generated using 2D synthetic fingerprint images with known fingerprint features (e.g. fingerprint type (loop, whorl, arch), minutiae position and orientation, and core and delta count and locations) can be used to evaluate fingerprint feature extraction and matching algorithms. Such targets can, therefore, be used for end-to-end evaluation of a fingerprint recognition system from placing the finger on the reader and capturing the 2D impression to extracting features and comparing the captured image to the gallery templates. Further, since the fabricated 3D targets are similar in characteristics to the human finger skin, in our opinion, they can also be used to evaluate the next generation touchless fingerprint readers [21] [10] [17]. Hence the proposed 3D targets are better suited for fingerprint system evaluation purposes than the prevailing methods which only use 2D synthesized fingerprint images (see Table 4.1).

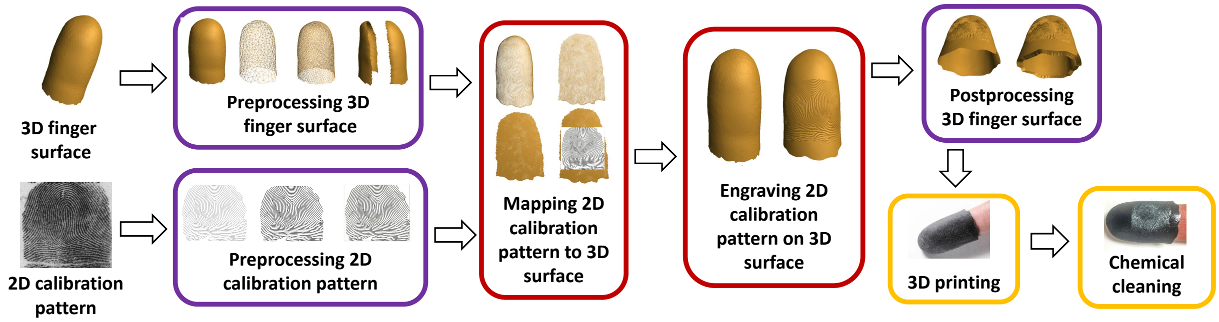

Figure 4.5 Generating a 3D single-finger target A, given a 2D calibration pattern I and a 3D finger surface S.

A physical 3D target is created by first projecting an electronic 2D calibration pattern onto a generic electronic 3D model of the finger surface[5]. The electronic 3D finger surface is aligned such that the finger length is along the y-axis, width along the x-axis and depth along the z-axis. The electronic 3D surface is then preprocessed to ensure sufficient fidelity for establishing the correspondence between the electronic 2D calibration pattern and the electronic 3D finger surface. The 2D calibration pattern is then mapped onto the front portion of the electronic 3D surface and correspondences between each vertex on the frontal electronic 3D surface and the pixel locations in the 2D calibration pattern are established. The 2D calibration pattern is engraved onto the frontal electronic 3D finger surface by displacing each vertex along the surface normal according to the texture values at the mapped pixel locations. Finally, the electronic 3D finger surface is post-processed to create an electronic model of a wearable 3D target ready for 3D printing. The physical 3D targets are fabricated using a state-of-the-art 3D printer (Stratasys Objet350 Connex[6]) with material similar in hardness and elasticity to the human finger skin. The 3D printed targets are cleaned using a 2M NaOH solution to generate evaluation-ready physical 3D targets. The complete process is illustrated in Figure 4.5.

[5]The 3D finger surface could either be the shape of the finger sensed using a 3D scanner or a synthetically generated surface describing the shape of the finger. In our case, the finger surface was scanned using the Artec Eva 3D scanner [2].

[6]The naming of companies and products here does not imply endorsement or recommendation of those companies or products by the authors or the organizations they represent.

There are two kinds of errors that can be introduced during 3D target creation from 2D image, (i) the 2D to 3D projection error of the mapping algorithm used in electronic 3D target creation, and (ii) the fabrication error introduced by the 3D printer when fabricating the physical 3D target from the electronic 3D target. To assess the fidelity[7] of the 3D target generation process, we estimate the 2D to 3D projection error, and the 3D printing fabrication error by observing the targets under a digital optical microscope (Keyence Digital Microscope VHX 600 [11]), (iii) matching 2D calibration pattern features used for 3D target creation to both the electronic and physical 3D target images, and (iv) evaluating similarity between different images of physical 3D targets. We show that (i) features present in the 2D calibration pattern are preserved during the creation of electronic 3D target, (ii) features engraved on the electronic 3D target are preserved during physical 3D target fabrication, and (iii) intra-class variability between multiple impressions of the same physical 3D target is sufficiently small for matching at false accept rate (FAR) of 0.01%. We also show that the generated 3D targets are suitable for behavioral evaluation of three different (500/1000 ppi) PIV/Appendix F certified single-finger optical readers in the operational settings.

In summary, the contributions of this chapter are as follows:

- Design of wearable 3D targets using a 2D to 3D projection algorithm that preserves distances on the 2D calibration pattern while mapping it to 3D finger surface. In our preliminary work [53], we used an angle-preserving 2D to 3D mapping [82] which did not preserve point-to-point spacing in the 2D calibration pattern during 3D projection, especially near the periphery of the 3D finger surface. Because it is important to preserve distances on the 2D calibration pattern after 3D projection, here we use a distance preserving mapping [177].

- Fabrication of 3D targets using a state-of-the-art 3D printer with materials having similar hardness and elasticity to the human finger skin. These targets can be imaged by three different commercial (500/1000 ppi) single-finger optical readers. The 3D printer used to fabri-

[7]Fidelity refers to the degree of exactness with which the 2D calibration image is reproduced in the generated 3D target.

cate targets in [53] only printed hard plastic targets that could not be imaged by commercial fingerprint readers.

- Procedure to chemically clean the 3D printed targets without impacting the engraved target patterns.

- Estimation of (i) 2D to 3D projection and (ii) 3D printing fabrication errors; these errors are accounted for during fingerprint reader evaluations.

- Comprehensive experimentation to show the fidelity of 2D calibration pattern features during 3D target generation.

- Preliminary experimentation for behavorial evaluation of fingerprint readers using the generated 3D targets.

4.2 Generating 3D Targets

A 3D target A is generated using an arbitrary 2D calibration pattern I with pre-specified features, and a generic 3D finger surface S. Let the grayscale value in the 2D calibration pattern I at spatial coordinates (u, v) be denoted by $I(u, v)$. Also, assume that the 3D finger surface S is a triangular mesh with a set V of vertices and a set T of triangles. Each vertex, v, in V has (x, y, z) coordinates corresponding to its spatial location in S, and a triangle in T connects a unique set of three vertices. Generating the 3D target A using I and S then consists of the following main steps (Figure 4.5).

1. **Preprocessing 3D finger surface**: Align S such that the finger length is along the y-axis in S. Sample vertices from the set V based on the curvature of S. This sampling process reduces the density of S, therefore, subdivide S (as explained in Section 2.1) to ensure sufficient fidelity during projection of the 2D calibration pattern I. Displace S outwards along the direction of the surface normals computed at each vertex to create an outer finger surface S_O. Separate the front S_{OF} and rear portion S_{OR} of S_O (see Fig. 4.6). The front portion S_{OF} of S_O will be used for projection. Retain the original surface S.

2. **Preprocessing 2D calibration pattern**: If the pattern I being projected is a 2D fingerprint image, extract the skeleton I_S of the image I. Increase the ridge width of the skeleton I_S using morphological operations, and smooth the image using a Gaussian filter before projecting it onto the electronic frontal surface S_{OF}. This preprocessing step is necessary to ensure that ridges and valleys present in I are engraved smoothly onto S_{OF}. Note that this preprocessing step is not needed if any other 2D calibration pattern (e.g. sine grating) is being projected.

3. **Mapping 2D fingerprint to 3D surface**: Project the front portion S_{OF} of 3D finger surface S_O to 2D and correct for rotation and flip using corresponding control points between 3D surface S_{OF} and the 2D projection of S_{OF}, and translation with respect to reference coordinates computed from I. Make the front portion of the outer finger surface S_O dense depending on the resolution of I to ensure sufficient fidelity of mapping I. Determine the mapping between the (x, y, z) spatial locations of the vertices on the front portion of the outer 3D surface S_O and the (u, v) image domain of I.

4. **Engraving 2D calibration pattern on 3D surface**: To create ridges and valleys, displace the vertices on the front portion of S_O along the surface normals according to the texture values in I at the mapped (u, v) locations.

5. **Postprocessing 3D finger surface**: Combine the front and rear portions of the outer finger surface S_O. Make the original finger surface S as dense as the outer finger surface S_O and then stitch the two surfaces together to obtain a watertight solid target. This finishes the creation of the 3D target A as an electronic (virtual) target.

6. **3D Printing**: Specify the physical dimensions as well as the printing material according to the hardness and elasticity of the human finger skin before printing the 3D target A using a 3D printer (Stratasys Objet350 Connex).

7. **Chemical Cleaning:** Clean the 3D printed targets using 2M NaOH solution and water to remove the printer support material residue and obtain evaluation-ready 3D targets.

A detailed description of each of these steps used in the 3D target creation process for a given 2D calibration pattern I and a 3D finger surface S is given below.

4.2.1 Preprocessing 3D finger surface

A sequence of preprocessing steps is executed on the 3D finger surface S before projecting the 2D calibration pattern I on S (see Figure 4.6). These steps include: (i) alignment of the 3D finger surface, (ii) remeshing the 3D finger surface, (iii) subdivision of the 3D surface, (iv) creating outer surface from the given 3D surface, and (v) separating front and rear portions of the outer 3D surface.

4.2.1.1 Alignment

The 3D finger surface S, arbitrarily oriented in the (x, y, z) coordinate frame, is first aligned such that the finger length is along the y-axis, width along the x-axis and height on the z-axis. For doing this, each vertex in the set V is translated such that the center of the surface S coincides with the origin of the (x, y, z) coordinate axes. Principal component analysis (PCA) [128] is used to determine the principle directions of the surface spread. The computed principal components are then used to align the surface S. Note that this step only alters the absolute (x, y, z) coordinate values of the vertices in V and retains the geometry of the surface S.

4.2.1.2 Remeshing

The 3D finger surface S is remeshed by sampling vertices from V using the method in [167]. The first vertex v_1 is sampled randomly from V, and the geodesic distance map $U(v_1)$ from v_1 to every other vertex in V is computed by solving the eikonal equation using the fast marching method [129]:

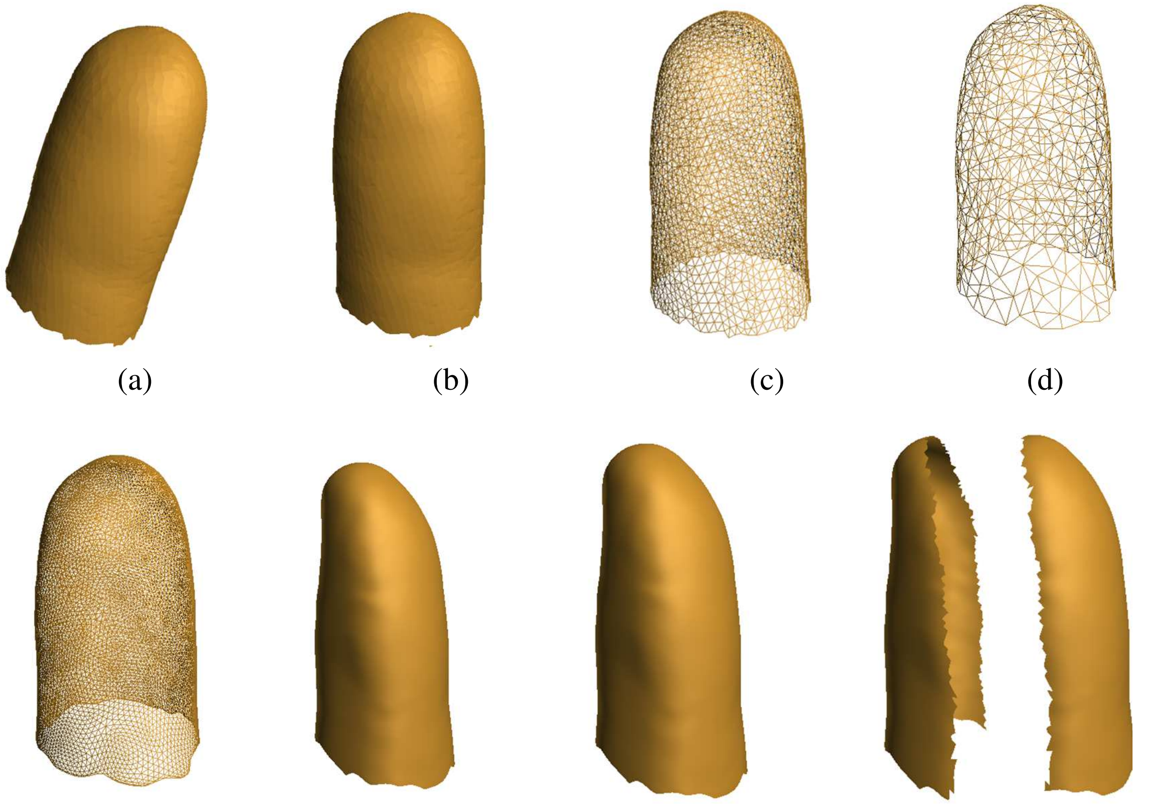

(a) (b) (c) (d)

(e) (f) (g) (h)

Figure 4.6 Preprocessing 3D finger surface. (a) Original finger surface S, (b) aligning S such that the finger length is along the y axis, (c) aligned S (triangular mesh), (d) remeshing S (triangular mesh), (e) subdividing S (triangular mesh), (f) subdivided S (profile view), (g) creating outer finger surface S_O from (f), and (h) separating front and rear portions, S_{OF} and S_{OR}, of S_O.

$$|| \bigtriangledown U(v_1)|| = P(v_1). \tag{4.1}$$

Here, $\bigtriangledown$ is the gradient operator, and $P = 1/F$, where F is the speed of front propagation used in the fast marching method.

Vertices are then sampled iteratively by adding the farthest vertex among the remaining vertices in iteration i from the vertices in the sampled vertex set V_{i-1} at iteration $i-1$. Note that the geodesic distance map U_i, at iteration i, is updated using the following equation:

$$U_i = min(U_{i-1}, U(v_i)), \tag{4.2}$$

where $U(v_i)$ is the geodesic distance map of the vertex sampled at iteration i, and U_{i-1} is the geodesic distance map computed at iteration $i-1$.

During this iterative procedure of sampling vertices, the speed of front propagation F is set to $1/(1+C)$, where C is the aggregate curvature at each vertex in V. This results in more vertices being sampled in the higher curvature regions of the 3D surface and vice versa. The aggregate curvature C is calculated using the two principal curvatures C_{min} and C_{max} as follows,

$$C = |C_{min}| + |C_{max}|. \tag{4.3}$$

Here, $|\ .|$ is the absolute value operator, C_{min} and C_{max} are computed from the 3D curvature tensor C_T calculated using the method in [49]. In particular, C_{min} and C_{max} correspond to the two highest eigenvalues of the curvature tensor C_T.

Finally, Delaunay triangulation is used for recreating the remeshed surface from the set of sampled vertices [51].

4.2.1.3 Subdivision

Although remeshing makes the surface S uniformly dense depending on its curvature, it reduces the density of the vertices. To ensure sufficient fidelity for projecting the 2D calibration pattern I onto the surface S, Loop's surface sub-division method [136] is used to increase density of vertices. Let the set of vertices and triangles obtained after remeshing be denoted by V_R and T_R, respectively. This method creates new vertices at each edge of every triangle in T_R using a weighted combination of neighborhood vertices, and creates new triangles by connecting the sampled vertices at edges adjacent to each other. The original vertices are then translated to maintain surface smoothness and continuity.

4.2.1.4 Creating outer surface

Let V_S and T_S be the set of vertices and triangles obtained after surface subdivision. Let the normal n at a vertex v in the set V_S be denoted by (n_x, n_y, n_z), where n_x, n_y and n_z represent the normal components along the x, y and z directions, respectively. Each vertex v is then displaced by a fixed factor d along the normal n to obtain the displaced coordinates of the vertex (v'_x, v'_y, v'_z):

$$\begin{bmatrix} v'_x \\ v'_y \\ v'_z \end{bmatrix} = \begin{bmatrix} v_x \\ v_y \\ v_z \end{bmatrix} + \begin{bmatrix} n_x \\ n_y \\ n_z \end{bmatrix} \times d \tag{4.4}$$

This is done to create an outer finger surface S_O where the 2D calibration pattern will be projected. The parameter d determines the thickness of the 3D target. Ideally, it is desirable to set d to be as small as possible. However, due to the limitation of the 3D printer resolution used for fabricating the targets, choosing a very small d results in the printed model being fragile. Therefore, d is empirically set to 1.5 mm in our experiments.

4.2.1.5 Separating front and rear portions

Front and rear portions of the outer finger surface S_O are then separated by computing the surface normals at each triangle in T_S, and then retaining the triangles and corresponding vertices where surface normals have the z-component greater than 0 in the front surface, and the rest in the rear surface. Note that the alignment of the finger surface done in step 1) facilitates this separation process. Let us denote the front portion of the outer surface S_O as S_{OF} having the set of vertices V_{OF} and triangles T_{OF}. Similarly, let the rear portion be denoted as S_{OR} with the set of vertices V_{OR} and triangles T_{OR}. We also retain the original finger surface S with the set of vertices V_S and triangles T_S.

4.2.2 Preprocessing 2D calibration pattern

If the pattern I being projected on 3D frontal surface S_{OF} is a fingerprint image, the following preprocessing steps are executed on I (see Figure 4.7):

1. The skeleton, I_S, of I, a 1-pixel wide ridge pattern, is extracted using a commercial fingerprint SDK [146].

(a) (b) (c) (d)

Figure 4.7 Preprocessing a 2D fingerprint pattern before projecting it onto 3D finger surface. (a) Original fingerprint image I, (b) extracted skeleton I_S of the fingerprint in (a), (c) skeleton I_S in (b) after applying the morphological operation of dilation, and (d) dilated skeleton in (c) smoothed using a gaussian filter.

2. The ridge width on the skeleton I_S is increased to 3 pixels by performing the morphological operation of dilation using a 2 pixel radius disk structured element.

3. I_S is filtered using a 4×4 Gaussian filter with $\sigma = 2.5$ to ensure that ridges and valleys in 2D fingerprint pattern I are engraved smoothly onto the 3D finger surface.

This preprocessing is not needed for other calibration patterns (e.g. sine grating of certain orientation and spacing).

4.2.3 Mapping 2D calibration pattern to 3D surface

The front portion S_{OF} of the outer finger surface S_O is projected from 3D ((x, y, z) space) to 2D ((u, v) space) by computing the ISOMAP embedding [177] (see Figure 4.8). Recall that the vertices and triangles in S_{OF} are V_{OF} and T_{OF}, respectively. The ISOMAP embedding is computed by:

1. **Constructing adjacency graph**: An adjacency graph G is created by connecting all vertex pairs $\{v_i, v_j\}$ in V_{OF} that share an edge of any triangle in T_{OF}. The edge weights in G are set to the euclidean distance $D(v_i, v_j)$ between v_i and v_j. For non-adjacent vertex pairs that do not share any edge, D is set to an arbitrary large value.

(a) (b) (c) (d) (e)

Figure 4.8 Mapping and engraving 2D calibration pattern onto the front portion of the outer 3D finger surface S_{OF}. (a) 3D frontal outer finger surface S_{OF}, (b) frontal surface S_{OF} in (a) is projected into 2D, (c) the 2D projected frontal surface S_{OFP} is subdivided, (d) correspondences are determined between the 2D projected frontal finger surface S_{OFP} and 2D calibration pattern I, (e) 3D frontal outer finger surface S_{OF} in (a) is displaced along the surface normals to engrave the pattern.

2. **Computing shortest paths**: Dijkstra's shortest path algorithm [84] is used to compute the shortest path between all pairs of nodes in G. Geodesic distances between all pairs of vertices in V_{OF} are estimated by the shortest path distances of the nodes in G.

3. **Constructing 2D embedding**: Let the matrix D_G contain the shortest path distances computed in the previous step. Given D_G, multidimensional scaling (MDS) [131] is used to create the 2D embedding of vertices.

   ISOMAP embedding is used because it minimizes the distortion induced when projecting the front portion S_{OF} of the 3D surface to 2D by preserving the geodesic distances between neighborhoood vertices on S_{OF}[8].

Let the 2D projected frontal surface in the (u, v) coordinate space be denoted by S_{OFP} with the set of vertices V_{OFP} and the set of triangles T_{OFP}. Rotation and flip during the 3D to 2D projection of S_{OF} are corrected using corresponding control points between S_{OF} and S_{OFP}. Reference coordinates $[r_u, r_v]$ are extracted from the 2D calibration pattern I for translation correction during the 3D to 2D projection of S_{OF}:

[8]Discrete conformal mapping was used for projecting a 2D pattern to 3D finger surface in our preliminary work [53]. It was, however, observed that discrete conformal mapping did not preserve the distances on the calibration pattern near the periphery of the 3D surface since it is an angle preserving mapping.

- If the pattern I being projected is a synthetic fingerprint image, then reference coordinates $[r_u, r_v]$ are extracted from the fingerprint image using the method in [186].

- If any other calibration pattern is being projected (e.g. sine gratings, horizontal/vertical bar patterns etc.), then the location of the center pixel in the 2D calibration pattern I is used as the reference point i.e. $[r_u, r_v] = [w/2, h/2]$, where w and h are the width and height of I.

The next step is to determine the one-to-one mapping between the pixel locations (u, v) on I and the vertices V_{OF} on S_{OFP}. For accurately determining the one-to-one correspondence, the density of S_{OF} as well as its 2D projection S_{OFP} is further increased using midpoint surface subdivision. Vertices are sampled on the midpoints of the edges in T_{OF}, and the sampled vertices on the adjacent edges are joined to create new triangles. The resolution of I being projected is factored into the computations while determining the correspondence between pixel locations on I and vertices V_{OF} on S_{OFP}. For example, if the calibration pattern being projected has a resolution of 500 ppi, the scale of projection is 19.685 pixels/mm. Therefore, the coordinates of I are scaled by this factor before determining the correspondence.

Ideally, the density of S_{OF} should be increased according to the dimensions of the calibration pattern I being projected. For example, if a calibration pattern of width w and height h with $w \times h$ pixels is being projected, then exactly $w \times h$ vertices are required in the projection region for building the exact correspondence between the pixel locations on I and the vertices on S_{OF}. However, it would result in a very large number of vertices and triangles on the surface and considerably increase the computational complexity of any further operations on the surface. Therefore, the density of S_{OF} is only increased to the extent that it retains the essential topology of the pattern being projected[9]. Let the set of vertices and triangles on the 2D projected frontal surface obtained after this step be denoted by V_{OFPS} and T_{OFPS}, and the corresponding vertices and triangles on the outer 3D frontal surface be V_{OFS} and T_{OFS}, respectively. The one-to-one correspondence between the pixel locations on the calibration pattern I and the set of vertices V_{OFP} is then established.

[9]For the finger surface used in our experiments, the density is increased so that there are approximately 250,000 vertices and 500,000 triangles on the front portion of the 3D surface.

(a) (b) (c) (d) (e)

Figure 4.9 Postprocessing 3D finger surface. (a) Separated front and rear portions of outer 3D surface, (b) front and rear portions shown in (a) are combined to create the outer 3D finger surface, (c) outer 3D finger surface (bottom view), (d) the retained original 3D finger surface (bottom view), (e) electronic 3D target created by stitching the outer and original surface in (c) and (d).

4.2.4 Engraving 2D calibration pattern on 3D surface

In the penultimate step, surface normals are computed at each vertex in the set V_{OFPS}. The vertices are then displaced along their surface normals to engrave the fingerprint ridges and valleys on S_{OF} (see Figure 4.8 (e)). Let the normal at a vertex v in the set V_{OFPS} be denoted by (n_x, n_y, n_z), where n_x, n_y and n_z represent the normal components along the x, y and z directions, respectively. The displaced coordinates of the vertex (v'_x, v'_y, v'_z) along the normal are then computed using the principle of vertex displacement mapping [39] as follows:

$$\begin{bmatrix} v'_x \\ v'_y \\ v'_z \end{bmatrix} = \begin{bmatrix} v_x \\ v_y \\ v_z \end{bmatrix} + \begin{bmatrix} n_x \\ n_y \\ n_z \end{bmatrix} \times (1 - I'(u, v)) \times R_d \tag{4.5}$$

Here, $I'(u, v)$ is the scale normalized grayscale value in the range $[0, 1]$ of the mapped grayscale value at (u, v) from the 2D calibration pattern on the vertex v, and R_d is the maximum vertical ridge displacement which is set to 0.22 mm in our experiments[10].

[10]The average ridge height on an adult human fingerprint is about 0.06 mm; however we set R_d to 0.22 mm empirically due to limitation of the state-of-the-art 3D printer resolution used for fabricating the targets.

Table 4.2 Comparison of mechanical properties of the two 3D printer materials used for 3D target fabrication with the human finger skin.

Property	**Human Skin [88] [89]**	**TangoBlackPlus FLX980 [31]**	**FLX 9840-DM [30]**
Shore A hardness	20-41	26-28	35-40
Tensile Strength (MPa)	5-30	0.8-1.5	1.3-1.8
Elongation at Break (%)	35-115	170-220	110-130

4.2.5 Postprocessing 3D finger surface

The engraved S_{OF} and S_{OR} are combined together to recreate the outer finger surface S'_O. The outer finger surface S'_O is then stitched together with the retained original finger surface S_O to create a continuous watertight 3D shell S_W ready for 3D printing. For doing this, the boundary of the two meshes S'_O and the S_O is first computed. Triangles are then synthetically generated to connect the two boundaries to create a continuous shell (see Figure 4.9). This continuous watertight shell is basically the 3D target A in electronic form.

4.2.6 3D printing

We use a state-of-the-art 3D printer (Stratasys Objet350 Connex) that has X and Y resolution of 600 dpi and Z resolution of 1600 dpi for fabricating the 3D targets with UV curable rubber-like polymeric materials. This printer is based on PolyJet printing technology which slices a 3D model into horizontal layers, and then prints the model layer by layer. The 3D targets are printed in high speed mode wherein they are sliced into 30 micrometer (μm) layers during the printing process. Note that the printer does not support printing the target with rubber-like materials in the high resolution mode which allows for even finer 16 micrometer layer slicing. However, we found that 30 μm slicing suffices with ridge displacement R_d of 0.22 mm. In the high speed mode, the time taken to fabricate one 3D target using the printer is approximately 90 minutes.

Two different rubber-like materials, TangoBlackPlus FLX980 [31], and FLX 9840-DM [30] (a digital material synthesized in the printer by combining a rubber-like material and a rigid material) are used for printing the 3D targets. These materials are specifically selected because they are

Figure 4.10 The 2D images of a manually cleaned 3D target (shown on the left) and the same target after chemical cleaning (shown on the right) captured using a single-finger optical fingerprint reader. Chemical cleaning of the 3D target with 2M NaOH solution and water removes the 3D printer support material residue and provides a better quality image.

similar in hardness and elasticity to the human finger skin (see Table 4.2)[11]. Note that we are limited in the choice of the printing material per the printer specifications.

Even though the choice of fabrication materials is limited, our approach is better than a manual process of creating a 2.5D or 3D mould of a finger and then casting the targets. This is because the 3D printing process (i) is automated, (ii) can accurately replicate targets, and (iii) is efficient because it can print several targets in parallel.

4.2.7 Chemical cleaning

While printing the 3D targets, the printer uses a support material to prevent the models being fabricated from breaking. As a result, once the targets are printed they need to be cleaned to remove the support material. Manual cleaning removes the bulk of support material, however, still leaves some residue. Therefore, the manually cleaned targets are dipped in a 2M NaOH solution for approx. 3 hours to dissolve the support material residue. Subsequently, the targets are cleaned

[11] The printing materials used are black in color, and their optical characteristics differ from that of human skin. Therefore, it may not be possible to image the fabricated targets using some optical readers (e.g. dark field readers). To overcome this limitation, we are currently exploring the possibility of using alternative fabrication methods.

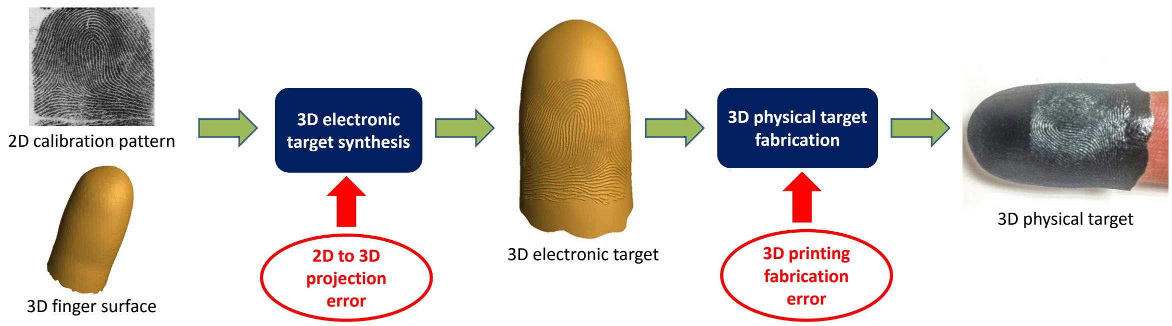

Figure 4.11 The two sources of error in 3D target generation (shown in red) given a 2D calibration pattern and a 3D finger surface: (i) 2D to 3D mapping, (ii) 3D printing fabrication.

with water to obtain evaluation-ready 3D targets. Figure 4.10 shows 2D images of a manually cleaned 3D target and the same target after chemical cleaning with 2M NaOH and water captured using a single-finger optical fingerprint reader. The target image quality improves considerably post chemical cleaning.

4.3 Fidelity of 3D Target Generation

In order to determine the fidelity of 3D target generation, we measure the error introduced during (i) projection of 2D calibration pattern to 3D surface to create electronic (virtual) target, and (ii) fabrication of physical 3D target from the electronic 3D target using 3D printing . We also conduct experiments to determine the fidelity of 2D pattern features during 3D target creation.

4.3.1 2D to 3D Projection Error

Geodesic distances between all pairs of vertices on the frontal 3D finger surface S_{OF}, and Euclidean distances between the corresponding 2D mapping of vertex pairs after the frontal surface is unwrapped to 2D using the ISOMAP algorithm are computed. Ratio of geodesic distances to euclidean distances is computed to determine the extent to which distances are preserved during 2D to 3D projection. For the finger surface used in our experiments, the geodesic to euclidean distance ratio is estimated as 0.942. This indicates that there is a 5.8% reduction in pairwise (point-to-point)

Table 4.3 Observed average grating spacing on three different targets when viewed under the Keyence VHX-600 Digital Microscope at two different magnifications (50X and 100X). Expected average spacing for each target is 0.478 mm.

Target	50X magnification	100X magnification
Horizontal	0.426 mm	0.427 mm
Vertical	0.420 mm	0.412 mm
Circular	0.415 mm	0.419 mm

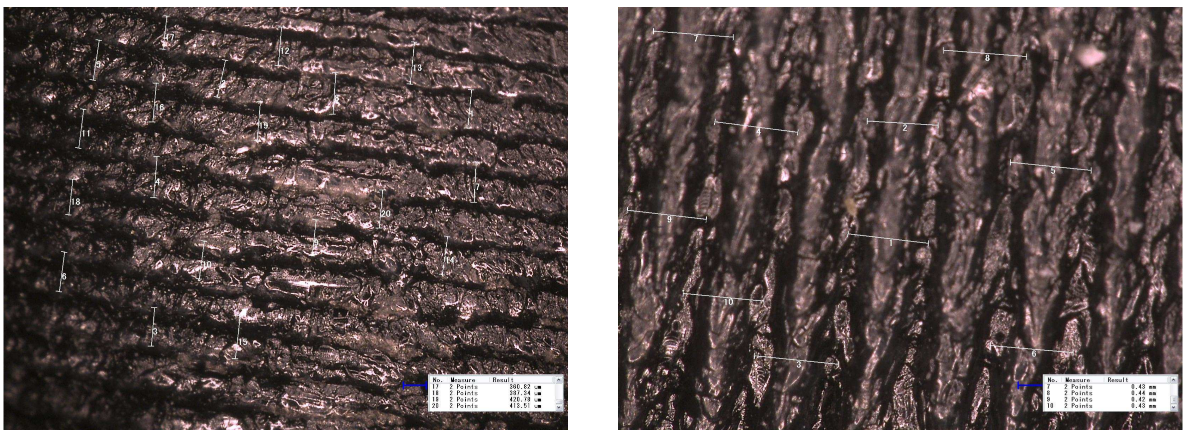

(a) (b)

Figure 4.12 Estimating 3D printing fabrication error by measuring point-to-point distances between horizontal gratings on a 3D target at (a) 50X and (b) 100X magnification using the Keyence Digital Microscope VHX-600.

distances due to 2D to 3D mapping algorithm. We account for this error in fingerprint reader evaluation experiments.

4.3.2 3D printing Fabrication Error

Three different 3D targets are created by projecting synthetically generated 2D test patterns: (i) horizontal, (ii) vertical, and (iii) circular gratings, with a fixed center-to-center spacing of 10 pixels. Spacing of 10 pixels in test pattern gratings should correspond to spacing of 0.508 mm in gratings etched on the fabricated physical targets (at the projection scale of 500 ppi). However, the expected average grating spacing on the physical targets is 0.478 (0.508×0.942) mm due to the 2D to 3D projection error (5.8%). To measure the observed average grating spacing on the fabricated targets, the three targets are viewed under an optical microscope (Keyence VHX 600 Digital Microscope [11]). Five different images of each of the three targets are captured at two different magnifications of 50X and 100X using the microscope. A total of 20 and 10 point pairs are manually marked on consecutive gratings in images captured at the magnifications of 50X and 100X, respectively. Point-to-point distances are measured between the marked point pairs using the software provided with the microscope (see, for example, Figure 4.12). The observed average grating spacing for the three targets at the two magnifications is estimated as the average of the point-to-point distance measurements taken between the manually marked point pairs (see Table 4.3). These measurements indicate that the gratings etched on the physical targets by the 3D printer are much closer to each other than expected or, in other words, grating spacing is reduced upon during 3D fabrication. Based on the difference between the observed and the expected average grating spacing for the three targets, the average reduction in grating spacing due to fabrication is estimated to be 11.42%. Although this error is quite significant, it is expected since we 3D print very fine (0.5 mm) gratings, and the 3D printer is not very accurate in printing objects at such a fine scale. This error is compensated for in fingerprint reader evaluation experiments.

4.3.3 Fidelity of 2D pattern features during 3D target creation

To assess if the features in the 2D calibration pattern are adequately preserved during the 3D target generation process, we determine if the

- features present in the 2D calibration pattern, I, are preserved during projection to 3D surface to create the electronic (virtual) 3D target,
- features engraved on the electronic 3D finger surface are preserved after fabrication of the physical 3D target,
- features present in the 2D pattern, I, are preserved on the physical 3D target, and
- intra-class variability between the captured impressions of the 3D target using fingerprint readers is minimal.

Table 4.4 Similarity scores between the images (2D) of the electronic 3D targets in Meshlab and the 2D fingerprint images from NIST SD4 used for target generation. Verifinger 6.3 SDK was used for generating similarity scores. The threshold on scores @FAR = 0.01% is 33.

Fingerprint	S0005	S0010	S0017	S0083	S0096
Score	171	378	212	116	106

Five different rolled fingerprint impressions from the NIST Special Database 4 (NIST SD4) [19] are used as calibration patterns and projected onto a 3D finger surface to generate electronic 3D targets. The physical 3D targets are fabricated with each of the two fabrication materials using a state-of-the-art 3D printer (see Section 4.2.6). Three single-finger optical readers, abbreviated as OR1, OR2, and OR3 are used for imaging the physical 3D targets[12]. OR1 is a *PIV* certified 500 ppi single-finger optical reader, whereas OR2 and OR3 are 1000 ppi single-finger optical readers complying with the IAFIS *Appendix F* image quality specifications. A commercial fingerprint SDK [146] is used for conducting all matching experiments. The captured images using the three readers are upsampled by a factor of 1.1 to account for ridge spacing reduction due to 2D to 3D projection and 3D printing before conducting the matching experiments.

4.3.3.1 Fidelity of 2D pattern features after projection to 3D surface

Each electronic 3D target is previewed in the 3D mesh processing software Meshlab [15], and its frontal image is taken. The captured image of the electronic 3D target is rescaled manually to the same scale as the original 2D fingerprint images used during the synthesis of the target. The rescaled frontal images of the electronic 3D target is matched to the original 2D fingerprint image using the fingerprint SDK.

Figure 4.13 shows a sample fingerprint image (calibration pattern) from the NIST SD4 and the images of its electronic 3D target. The minutiae extracted and matched using the fingerprint SDK are marked on the two images. Table 4.4 shows the corresponding similarity scores. All similarity

[12]Capacitive fingerprint readers could not be used in our evaluation because state-of-the-art 3D printers currently do not allow printing objects using conductive materials. We are currently exploring the possibility of using alternative fabrication methods to introduce conductivity.

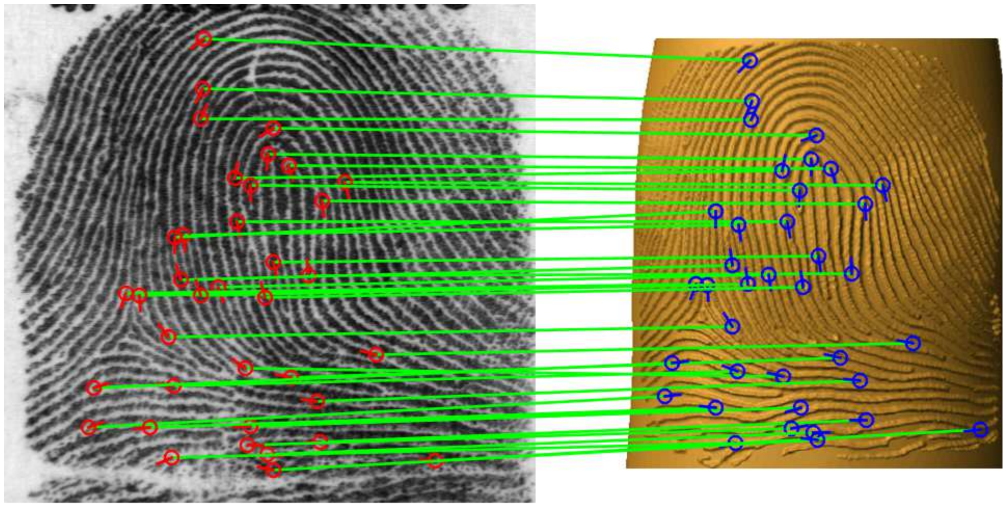

Figure 4.13 Minutiae correspondence between (a) rolled fingerprint image (S0083 from the NIST SD4), and (b) 2D rendering of the electronic 3D target generated using (a). Similarity score of 116 is obtained between (a) and (b) which is above the threshold of 33 at 0.01% FAR.

scores are significantly above the verification score threshold of 33 (@FAR = 0.01%) for NIST SD4. This demonstrates that the features present in the 2D fingerprint images are preserved during the synthesis of the electronic 3D targets.

4.3.3.2 Fidelity of the engraved features on the 3D surface after 3D printing

The image of an electronic 3D target is matched to captured image of the corresponding physical 3D target using the three single-finger optical readers for each of the ten 3D targets. Figure 4.14 shows minutiae correspondences obtained using the fingerprint SDK between the image of one electronic target and its captured image using optical reader OR2. Table 4.5 shows the similarity scores for this experiment. Notice that the similarity scores are significantly above the verification threshold score of 33 (@FAR = 0.01%) for all ten targets. This demonstrates the fidelity of features engraved on the 3D surface after 3D printing.

Table 4.5 Similarity scores between the images (2D) of the electronic 3D targets and the images captured by the three single-finger optical readers of the physical 3D targets fabricated with two different materials (TangoBlackPlus FLX980 and FLX 9840-DM). Verifinger 6.3 SDK was used for generating similarity scores. The threshold on scores @FAR = 0.01% is 33.

TangoBlackPlus FLX980

Fingerprint	OR1 (500 ppi)	OR2 (1000 ppi)	OR3 (1000 ppi)
S0005	165	197	392
S0010	192	350	359
S0017	143	180	207
S0083	372	407	348
S0096	165	204	336

FLX 9840-DM

Fingerprint	OR1 (500 ppi)	OR2 (1000 ppi)	OR3 (1000 ppi)
S0005	201	342	324
S0010	194	390	342
S0017	143	228	302
S0083	326	473	441
S0096	120	210	179

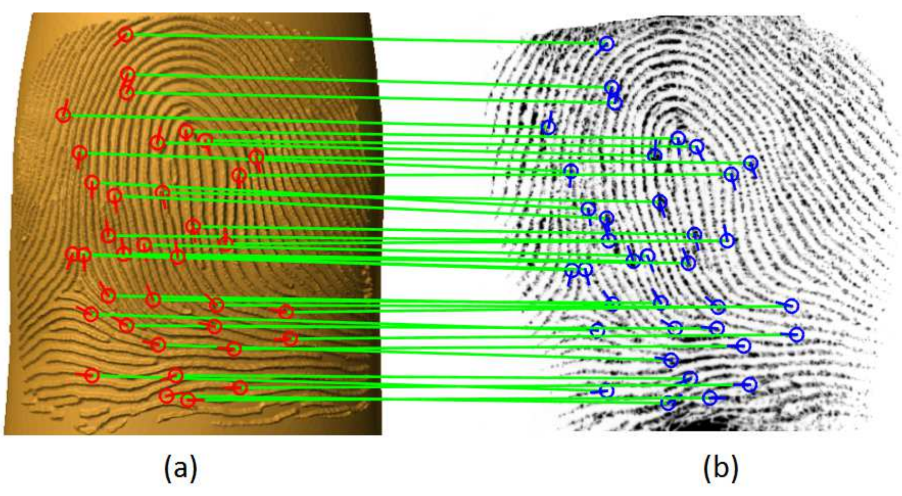

Figure 4.14 Minutiae correspondence between (a) image of the electronic 3D target (of fingerprint S0083 in NIST SD4), and (b) the image captured by optical reader 2 (1000 ppi) of the physical 3D target fabricated with FLX 9840-DM. Similarity score of 473 is obtained between (a) and (b) which is above the threshold of 33 at 0.01% FAR.

Table 4.6 Similarity scores between the images captured by the three single-finger optical readers of the 3D targets fabricated with two different materials (TangoBlackPlus FLX980 and FLX 9840-DM) and the fingerprints from NIST SD4 used in their generation. Verifinger 6.3 SDK was used for generating similarity scores. The threshold on scores @FAR = 0.01% is 33.

TangoBlackPlus FLX980

Fingerprint	OR1 (500 ppi)	OR2 (1000 ppi)	OR3 (1000 ppi)
S0005	93	161	171
S0010	129	150	183
S0017	93	167	167
S0083	174	344	167
S0096	131	240	197

FLX 9840-DM

Fingerprint	OR1 (500 ppi)	OR2 (1000 ppi)	OR3 (1000 ppi)
S0005	114	410	185
S0010	113	209	173
S0017	122	182	158
S0083	140	374	305
S0096	96	177	177

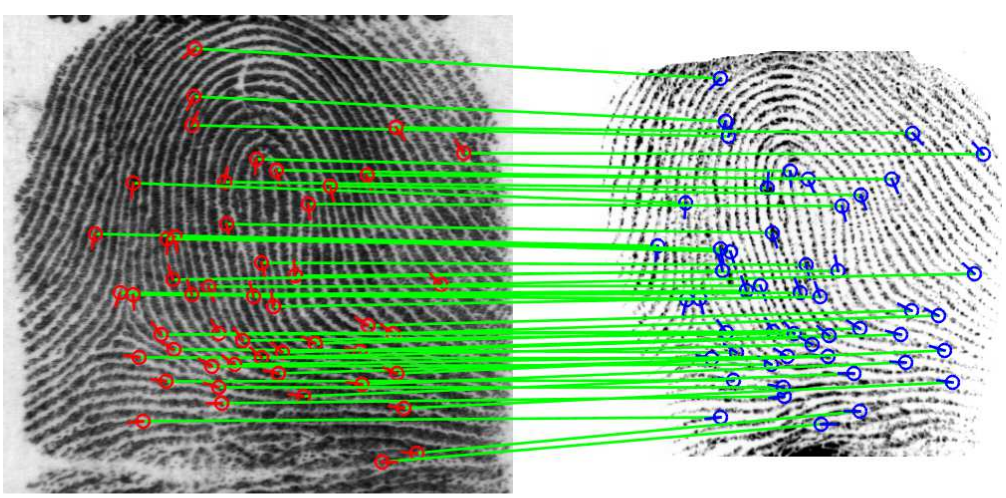

(a) (b)

Figure 4.15 Minutiae correspondence between (a) rolled fingerprint image (S0083 from the NIST SD4), and (b) the image captured by optical reader 2 (1000 ppi) of the 3D single-finger target generated using (a) and fabricated with FLX 9840-DM. Similarity score of 374 is obtained between (a) and (b) which is above the threshold of 33 at 0.01% FAR.

Table 4.7 Range of similarity scores for pairwise comparisons between five different images captured by the three single-finger optical readers of the same 3D target fabricated with two different materials (TangoBlackPlus FLX980 and FLX 9840-DM). Verifinger 6.3 SDK was used for generating similarity scores. The threshold on scores @FAR = 0.01% is 33.

TangoBlackPlus FLX980

Fingerprint	OR1 (500 ppi)	OR2 (1000 ppi)	OR3 (1000 ppi)
S0005	431-1017	675-1146	929-1286
S0010	638-1049	1053-1455	1169-1620
S0017	464-1155	1230-1592	843-1292
S0083	890-1440	1016-1620	744-1325
S0096	726-1286	842-1443	774-1334

FLX 9840-DM

Fingerprint	OR1 (500 ppi)	OR2 (1000 ppi)	OR3 (1000 ppi)
S0005	597-1295	1103-1689	921-1620
S0010	647-1239	1256-1643	1299-1605
S0017	534-1298	1203-1479	1170-1481
S0083	614-1262	1326-1697	1215-1656
S0096	807-1344	1154-1401	1238-1607

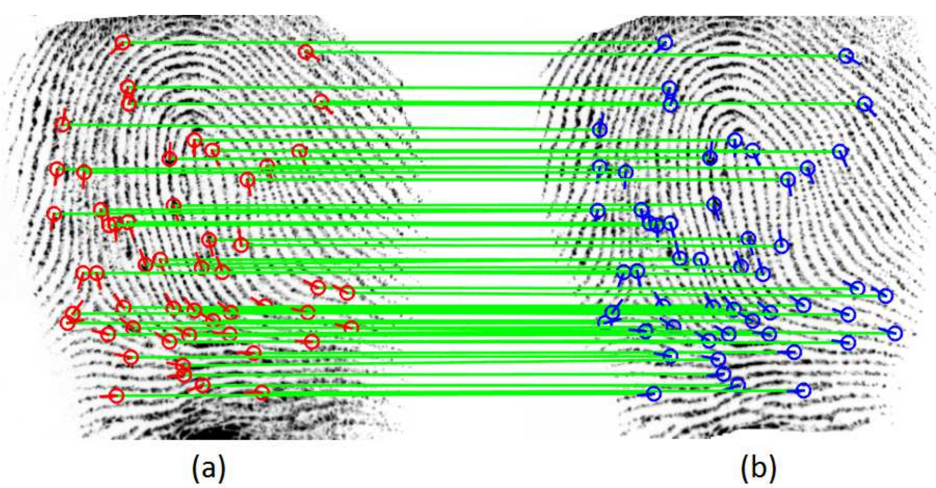

Figure 4.16 Minutiae correspondence between two images (a) and (b) captured by optical reader 2 (1000 ppi) of the 3D target generated from fingerprint S0083 in NIST SD4 and fabricated with FLX 9840-DM. Similarity score of 1494 is obtained between (a) and (b) which is above the threshold of 33 at 0.01% FAR.

4.3.3.3 End-to-end fidelity of 2D calibration pattern features after 3D printing

Table 4.6 shows the similarity scores obtained when comparing the images of all ten 3D targets captured using the three readers to the corresponding original 2D fingerprint images. Figure 4.15 shows minutiae correspondence between the fingerprint image and images of the generated 3D target using the fingerprint SDK. The key observations and inferences based on this experiment are:

- Images of the 3D targets captured using all three single-finger optical readers can be successfully matched to the original fingerprint images used for generating the targets; all the similarity scores in Table 4.6 are significantly above the verification threshold score of 33 (@FAR = 0.01%).

- Because the images of the 3D targets can be successfully matched to the original fingerprint images (@FAR = 0.01%), it can be inferred that the salient features present in the 2D pattern are preserved during the fabrication of the physical 3D target.

4.3.3.4 Intra-class variability between 3D target impressions

Five different impressions of each of the ten 3D targets are captured using all three single-finger optical readers. Pairwise comparisons between the five impressions obtained from a fingerprint reader are performed using the fingerprint SDK. Figure 4.16 shows the minutiae correspondence between two different impressions of a 3D target captured using optical reader OR2. Table 4.7 shows the range of similarity scores all of which are significantly higher than the threshold at 0.01% FAR. This indicates that the intra-class variability between different images of the 3D target is small.

4.4 Behavioral Evaluation of Fingerprint Readers using 3D Targets

In behavioral evaluation, the aim is to test the functionality of the fingerprint reader in the operational scenario. There are several different parameters which can impact the quality of the image captured by the reader in a functional setting, e.g., the amount and direction of the pressure applied by a user and the movement of his finger on the reader platen when capturing the fingerprint image. Our end goal is to assess the effect of these parameters on the reader performance by explicitly controlling these parameters. For this, we plan to mount 3D targets on a robotic hand and conduct controlled experimentation. However, to show the utility of the fabricated 3D targets for behavioral evaluation of fingerprint readers, we conduct two preliminary experiments (i) using 3D targets created from synthetically generated test patterns to evaluate directional imaging capability (Experiment I), and (ii) using 3D targets created by projecting fingerprint patterns to evaluate the capability to capture fingerprint patterns (Experiment II).

4.4.1 Experiment I: Synthetic Sine Grating Targets

Ten different impressions of each of the three targets created using horizontal, vertical and circular sine gratings of 10 pixel spacing are captured using all three single-finger optical readers. Center-to-center spacing is then measured in each of the captured impressions using the method in [104]. Directional imaging capability of fingerprint readers is subsequently assessed based on how well the grating spacing on the three targets is recovered by the readers. Figs. 4.17, 4.18 and 4.19 show the three directional test patterns, the electronic targets generated using the three patterns, and some sample images of the three targets captured using the three optical readers. The average and the standard deviation of the observed center-to-center grating spacing in the captured impressions of the three targets is reported in Table 4.8. Note that the expected grating spacing on these targets is 8.278 (10×0.827) pixels after taking into account the projection (5.8%) and fabrication error (11.42%). Following are some observations based on this experiment:

Table 4.8 Mean (μ) and std. deviation (σ) of center-to-center spacing in the images of the three directional test targets captured using the three single-finger optical readers (OR). (Expected grating spacing = 8.278 pixels.)

Test pattern	**OR1 (500 ppi)**	**OR2 (1000 ppi)**	**OR3 (1000 ppi)**
Horizontal	$\mu = 8.307$, $\sigma = 0.101$	$\mu = 8.445$, $\sigma = 0.085$	$\mu = 8.420$, $\sigma = 0.030$
Vertical	$\mu = 8.869$, $\sigma = 0.076$	$\mu = 8.561$, $\sigma = 0.076$	$\mu = 8.592$, $\sigma = 0.098$
Circular	$\mu = 8.921$, $\sigma = 0.044$	$\mu = 8.823$, $\sigma = 0.048$	$\mu = 8.721$, $\sigma = 0.053$

(a) (b) (c) (d) (e)

Figure 4.17 Evaluating single-finger optical readers with a 3D target generated using a horizontal sine grating. (a) Horizontal sine grating (10 pixel separation between the gratings); (b) electronic 3D target generated using (a); (c), (d) and (e) are sample images of the fabricated target captured using optical readers 1, 2 and 3, respectively. There is a slight distortion apparent in (b) that is due to the 2D to 3D projection error.

- The observed spacing in images of all three targets is, on average, greater than the expected spacing. Since we account for the 2D to 3D projection and 3D fabrication errors in our spacing measurements, this difference should be due to the flattening of 3D target gratings when the target is pressed against the reader platen. We performed one-sample t-test [151] to ascertain if the mean of the observed spacing in each case is statistically different compared to the expected spacing. In all but one case, the mean observed spacing was determined to be significantly different than the expected mean at significance level of 0.05.

- The deviation from the expected spacing is found to be greater for the circular target than the horizontal and vertical targets. This can be explained by the fact that the characteristic flattening induced when the target is pressed against the reader platen is radial around the

(a) (b) (c) (d) (e)

Figure 4.18 Evaluating single-finger optical readers with a 3D target generated using a vertical sine grating. (a) Vertical sine grating (10 pixel separation between the gratings); (b) electronic 3D target generated using (a); (c), (d) and (e) are sample images of the fabricated target captured using optical readers 1, 2 and 3, respectively. There is a slight distortion apparent in (b) that is due to the 2D to 3D projection error.

central point of contact. In other words, target regions closer to the central point of contact with the reader platen flatten out more compared to surrounding regions. The relative effect of such a flattening is not as profound on both horizontal and vertical gratings compared to circular gratings because the circular gratings align symmetrically with the radial flattening.

- The horizontal target spacing captured by all three readers is observed to be closest to the expected spacing compared to vertical and circular targets. This may be due to the way pressure is applied on the reader platen with respect to the relative orientation of the gratings while capturing the target images. Controlled experimentation, where both the magnitude and direction of pressure applied on the reader platen is fixed before capturing the target impressions, is required to understand the underlying cause, which will be undertaken in future studies.

4.4.2 Experiment II: Fingerprint Targets

The ten 3D targets generated by projecting five different fingerprint images from NIST SD4 and fabricated using each of the two printing materials are used to evaluate the imaging capability of the

(a) (b) (c) (d) (e)

Figure 4.19 Evaluating fingerprint readers with a 3D target generated using a circular sine grating. (a) Circular sine grating (10 pixel separation between the gratings); (b) electronic 3D target generated using (a); (c), (d) and (e) are sample images of the fabricated target captured using optical readers 1, 2 and 3, respectively. There is a slight distortion apparent in (b) that is due to the 2D to 3D projection error.

three fingerprint readers to capture fingerprint patterns. Center-to-center ridge spacing is computed on the original 2D fingerprint pattern that is used to create each target using the method in [104]. Analogous to Experiment I, the average and variance of center-to-center ridge spacing values is computed for five different 2D impressions of each target captured using the three single-finger optical readers. Note that the same method [104] is used to compute ridge spacing on the captured 2D plain impressions of the targets. Table 4.9 shows the computed ridge spacing measurements. Following are the main observations based on this experiment:

- To determine if they are statistically different, the mean observed spacing in each case was compared to the expected spacing using one-sample t-test [151]. In all cases, the mean observed spacing was found to be significantly different than the expected spacing at significance level of 0.05.

- The 1000 ppi readers OR2 and OR3 are, on average, better than the 500 ppi reader in preserving fingerprint ridge spacing. This may be due to lesser ridge flattening being induced by the reader platens for these two readers compared to OR1. Amongst the two 1000 ppi

Table 4.9 Mean (μ) and std. deviation (σ) of center-to-center ridge spacing in the fingerprint target images captured using the three single-finger optical readers (OR). The expected average ridge spacing (in pixels) in the target images is indicated in brackets.

TangoBlackPlus FLX980

Test pattern	OR1 (500 ppi)	OR2 (1000 ppi)	OR3 (1000 ppi)
S0005 (7.818)	$\mu = 8.493, \sigma = 0.096$	$\mu = 8.250, \sigma = 0.048$	$\mu = 8.099, \sigma = 0.054$
S0010 (8.433)	$\mu = 9.215, \sigma = 0.156$	$\mu = 9.172, \sigma = 0.024$	$\mu = 9.128, \sigma = 0.053$
S0017 (8.932)	$\mu = 9.893, \sigma = 0.118$	$\mu = 9.525, \sigma = 0.038$	$\mu = 9.523, \sigma = 0.136$
S0083 (8.621)	$\mu = 9.100, \sigma = 0.191$	$\mu = 9.111, \sigma = 0.057$	$\mu = 9.110, \sigma = 0.190$
S0096 (8.473)	$\mu = 8.817, \sigma = 0.056$	$\mu = 8.839, \sigma = 0.075$	$\mu = 8.670, \sigma = 0.102$

FLX 9840-DM

Test pattern	OR1 (500 ppi)	OR2 (1000 ppi)	OR3 (1000 ppi)
S0005 (7.818)	$\mu = 8.440, \sigma = 0.129$	$\mu = 8.288, \sigma = 0.011$	$\mu = 8.135, \sigma = 0.079$
S0010 (8.433)	$\mu = 9.559, \sigma = 0.065$	$\mu = 9.168, \sigma = 0.052$	$\mu = 9.077, \sigma = 0.048$
S0017 (8.932)	$\mu = 9.988, \sigma = 0.073$	$\mu = 9.539, \sigma = 0.032$	$\mu = 9.565, \sigma = 0.055$
S0083 (8.621)	$\mu = 9.302, \sigma = 0.061$	$\mu = 9.131, \sigma = 0.037$	$\mu = 9.080, \sigma = 0.042$
S0096 (8.473)	$\mu = 8.752, \sigma = 0.102$	$\mu = 8.772, \sigma = 0.063$	$\mu = 8.654, \sigma = 0.063$

readers, OR3 seems to perform marginally better, on an average, than OR2 in preserving fingerprint ridge spacing.

- The 500 ppi reader OR1 has a small platen and is only able to partially image the fingerprint targets. Therefore, overall fewer spacing measurements are used for average spacing computations and the variation in spacing is relatively higher for the reader OR1 than the readers OR2 and OR3.

- There is no significant impact of the fabrication material on the ridge spacing measurements in fingerprint images captured using the three readers.

All three single-finger optical readers used for conducting experiments are *PIV/Appendix F* certified. Note, however, that the errors obtained in our evaluation experiments are comparatively greater than permitted geometric errors for the *PIV* and *Appendix F* standards. This is because of the flattening of the patterns on the 3D targets when they are pressed against the reader platens.

The current certification standards do not explicitly account for this error. However, it is important to consider this error in the operational scenario where user-dependent parameters, such as finger placement and pressure applied on the reader platen, directly impact the fingerprint image acquired by a fingerprint reader.

Another important consideration is how many different targets and imaging samples per target are adequate for evaluation of fingerprint readers. To this effect, it is important that the set of targets used for reader evaluation are representative of operational fingerprint data. Targets generated using fingerprint patterns of different types (whorl, loop, and arch) and using different finger shapes are desirable to test for variations encountered in the functional environment. It is also important to capture multiple impressions of these targets to measure the effect of intra-class variations.

4.5 Conclusions

Structural evaluation of fingerprint readers is typically done using 2D or 3D targets designed for calibrating imaging devices. While these targets are used for structural evaluation of fingerprint readers, they cannot be used for behavioral evaluation of fingerprint readers in operational scenarios. In this research, we have designed and fabricated wearable 3D single-finger targets that can be placed on the fingerprint reader platen, and imaged analogous to operational setting where a user's finger will interact with the reader. The 3D targets are created by projecting 2D calibration patterns of known characteristics (e.g. sine gratings of known spacing) onto a generic 3D finger surface to generate electronic 3D targets. The electronic targets are then fabricated using a state-of-the-art 3D printer with material similar in hardness and elasticity to the human finger skin. Our experimental results show that (i) features present in the 2D calibration pattern are preserved during the creation of electronic 3D target, (ii) features engraved on the electronic 3D target are preserved during physical 3D target fabrication, and (iii) intra-class variability between multiple images of the same physical 3D target is sufficiently small for matching at 0.01% FAR. We also show that the generated 3D targets can be used for behavioral evaluation of three different (500/1000 ppi) PIV/Appendix F certified single-finger optical readers in the operational settings.

Chapter 5

3D Whole Hand Targets: Evaluating Slap and Contactless Readers

5.1 Introduction

In the previous chapter, we designed and fabricated 3D single-finger targets for optical readers with skin-like hardness and elasticity that could be worn on a finger to mimic the fingerprint capture process. We projected 2D calibration patterns of known characteristics (e.g. fingerprints with known ridge flow, ridge spacing and minutiae or sine gratings of pre-specified orientation and spacing) onto a 3D finger surface of known dimensions to create electronic 3D targets. The electronic 3D targets were fabricated using a state-of-the-art 3D printer (Stratasys Objet350 Connex); the printed targets were then successfully used for evaluating single-finger optical readers.

Fingerprint recognition systems designed for large-scale applications (e.g. law enforcement [160], homeland security [20] and national ID programs [38]) generally require capturing all ten fingerprints (tenprints) of a person during enrolment (see, e.g., Figure 5.1). To maintain high throughput, tenprint acquisition is usually done by capturing two slap impressions[1] of the four fingers of the left and right hand, followed by simultaneous capture of the two thumbprints (also

[1] A four-finger simultaneous capture (index, middle, ring and little fingers altogether) is called a *slap impression*.

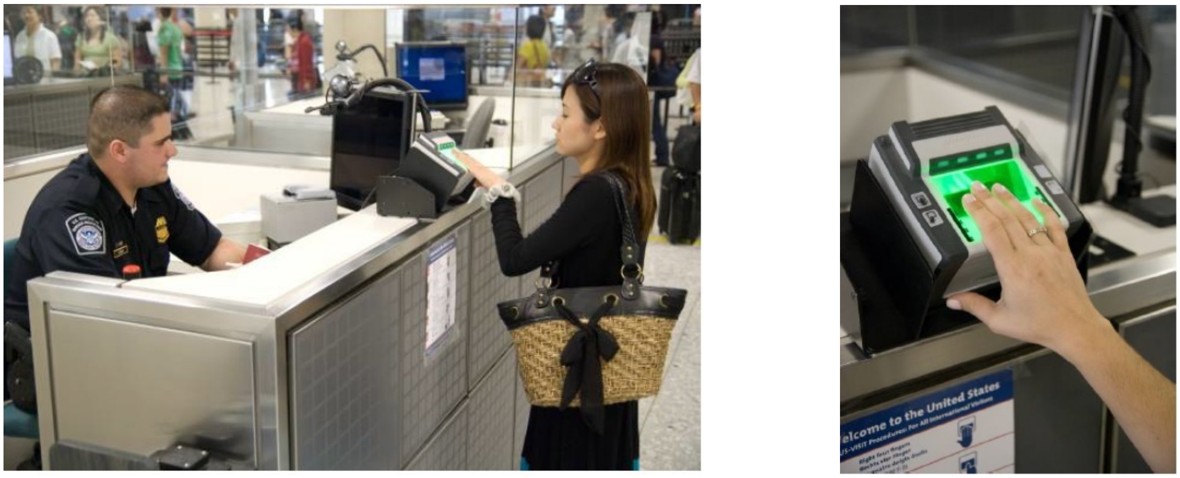

(a) (b)

Figure 5.1 Tenprint capture (four finger capture of each of the two hands (shown in (a) and (b)) followed by simultaneous capture of the two thumbs) by a United States (US) Customs and Border Protection (CBP) officer at a port of entry in the US. Image reproduced from [158].

termed as *4-4-2* capture) using a slap fingerprint reader. Most slap fingerprint readers are contact-based optical devices that capture fingerprints in the following manner: (i) user places four fingers or two thumbs of his hand on a glass platen, (ii) his fingers are illuminated with light of a specific wavelength, (iii) friction ridges on the finger tip absorb the incident light while valleys reflect the light, and (iv) a glass prism deflects the reflected light onto a CCD or CMOS array for imaging the fingers. The quality of the acquired slap impression is a function of several user-dependent variables, e.g., the pressure applied on the reader platen by each finger, and the relative orientation of the fingers with respect to each other and the reader platen, as well as the reader optics.

Contact-based slap capture, however, induces distortion in the captured image due to flattening of the skin when the fingers are pressed against the reader platen. It is also typically required to clean the reader platen after every few captures to prevent accumulated residue due to repeated use of the reader from impacting the quality of the captured image. Further, some users have hygiene-related concerns in using contact-based readers. To alleviate these issues, contactless slap fingerprint capture technology was introduced, and has since garnered significant attention [165]. In 2007, the National Institute of Justice (NIJ) initiated the fast capture initiative to create new

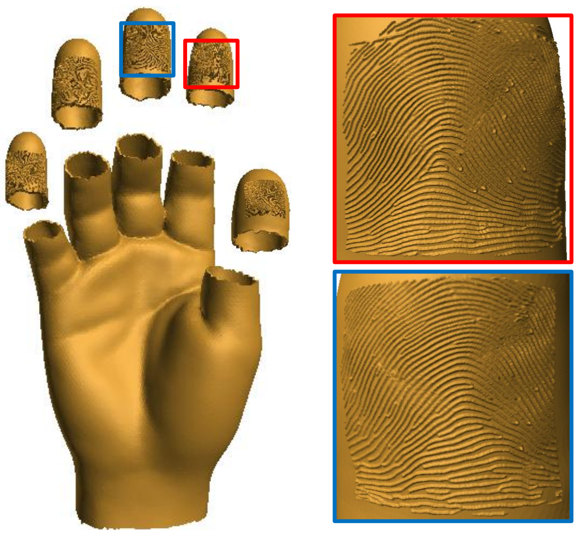

(a)

(b)

(c)

Figure 5.2 3D whole hand target for evaluating slap and contactless fingerprint readers. (a) Electronic 3D hand target complete with the four fingers, thumb and fingerless glove; the index and middle fingerprints engraved on the target are shown at full scale in red and blue boxes, respectively. (b) Fabricated hand target with translucent rubber-like material TangoPlus FLX930 [31]. (c) slap fingerprint capture by a contact-based reader using the fabricated hand target in (b).

technology that will automatically "capture the same images as 10 rolled fingerprints in less than 15 seconds and both palm prints in less than 1 minute" [7]. The goal of NIJ's initiative was to improve fingerprint image quality, throughput and the commercialization of contactless fingerprint readers for law enforcement and homeland security agencies. Given that almost all criminal fingerprint databases contain rolled prints, another objective of this initiative was to improve fingerprint identification accuracy by comparing rolled prints to rolled prints rather than slap to rolled prints. Since then, significant advances have been made in the design and development of commercial-grade contactless slap fingerprint readers.

State-of-the-art contactless fingerprint readers generally use one of the following two optical imaging techniques: (i) structured lighting, where a fixed light pattern is used to estimate the difference in the depth of ridges and valleys for generating a 3D representation of the finger, or (ii) multi-view imaging technique where multiple cameras are used to image the finger from different viewpoints to construct a 3D fingerprint representation. An important requirement for acquiring good quality fingerprint images using contactless slap readers is the proper positioning of the user's hand/finger with respect to the imaging component of the reader. Given that user-induced variabilities can impact the quality of fingerprint images acquired by contactless slap readers, it is important to evaluate the readers to ensure that image quality suffices for fingerprint recognition, i.e., comparing acquired fingerprint images to rolled (or slap) prints in the database. While evaluation procedures have been developed to assess contact-based fingerprint readers [155] [156], there is still an impending need to develop methods, metrics and artifacts for evaluation of contactless fingerprint readers. For this reason, NIST started the Contactless Fingerprint Capture Device Measurement Research Program with the aim of "developing methodologies for measuring the image fidelity of contactless fingerprint capture devices" [3].

Here, we design and fabricate whole hand targets (both electronic and physical) for evaluating contact-based and contactless slap fingerprint readers (see Fig. 5.2)[2]. To create a whole hand

[2]This work was published in the proceedings of the International Conference of the Biometrics Special Interest Group (BIOSIG), 2016 [55].

(a) (b) (c) (d)

Figure 5.3 Images of a 3D fingerprint target fabricated with translucent rubber-like material TangoPlus FLX930 [31] (shown in (a)) captured by three different *PIV* certified [155] single-finger optical readers using different wavelengths of light for fingerprint capture: (b) blue wavelength, (c) combination of blue and red wavelengths, and (d) red wavelength. Targets printed with black colored rubber-like materials (TangoBlackPlus FLX980 [31] and FLX9840-DM [30]) could not be imaged using these three readers.

target, we first segment an electronic 3D hand surface[3] into six different parts: four individual fingers, the thumb, and the remaining middle portion of the hand surface[4]. Individual targets for the four fingers and the thumb are created by projecting pre-specified 2D calibration patterns onto 3D finger surfaces using the method described in the previous chapter. The middle portion of the hand surface is synthetically processed to make a wearable fingerless glove. Each of the six parts of the whole hand are printed using a state-of-the-art 3D printer (Stratasys Objet350/500 Connex[45]) with materials that are similar in hardness and elasticity to the human skin as well as appropriate for imaging with optical readers. The printer slices 3D parts into 2D horizontal layers and prints them layer by layer. It uses a support material to prevent the parts being printed from breaking. The bulk of the support material can be manually removed from the printed parts. However, to remove any support material debris remaining on the printed parts, the individual parts are subsequently

[3] 3D hand surface can either be obtained directly using a 3D scanner or synthetically generated. We use a synthetically designed 3D hand surface.

[4] A single 3D hand target model with all five fingerprints becomes quite complex due to the resolution requirements for engraving fingerprints. Because the 3D printer software does not accept large electronic model files (>100 MB), the hand target is designed and manufactured in parts.

[5] The two printers have X and Y resolution of 600 dpi and Z resolution of 1600 dpi. This suffices for printing targets with micron-scale gratings, e.g., fingerprints.

cleaned with 2M NaOH solution and water. The printed parts are then physically assembled to create the whole hand target (see Fig. 1(b)).

The printed 3D hand targets can be imaged using three different commercial (500/1000 ppi) *Appendix F* certified contact-based slap fingerprint readers and a *PIV* certified contactless slap reader[6]. We extract individual plain prints[7] for each finger from slap impressions of the whole hand targets captured using the three slap readers and show that they can be successfully matched to (i) the original 2D fingerprints used to create the whole hand target, and (ii) the frontal images of electronic whole hand targets. We also conduct experiments to evaluate the three slap readers and the contactless slap reader using the generated whole hand target. The contributions of the research detailed in this chapter are as follows:

1. Generation of whole hand target for evaluating contact-based and contactless slap fingerprint readers. In the previous chapter, we had generated individual finger targets for evaluating single-finger contact-based optical readers only. We further extend our method to generate a whole hand target for use with multi-finger optical devices, e.g. slap fingerprint readers.

2. Determination of optically compatible 3D printing materials for fabricating 3D targets. Previously, we had printed 3D targets with materials similar in hardness and elasticity to the finger skin (TangoBlackPlus FLX980 [31] and FLX9840-DM [30][4]). However, these materials were black in color, and could not be imaged with optical readers using certain light wavelengths (e.g. blue). To remedy this, we now use translucent whitish rubbery materials (TangoPlus FLX930 [31] and FLX9740-DM [30][4]) that provide the desired hardness and elasticity as well as appropriate optical properties for use with a variety of contact-based optical fingerprint readers (see Fig. 5.3). A bluish-gray colored rigid opaque material (RGD8520-DM [30]) is used to manufacture fingerprint targets for the contactless slap

[6]The contactless slap reader captures four fingerprints (index, middle, ring and little fingers) with a single hand movement.

[7]The term *plain print* is used to refer to the fingerprint impression of an individual finger extracted from the slap impression [23].

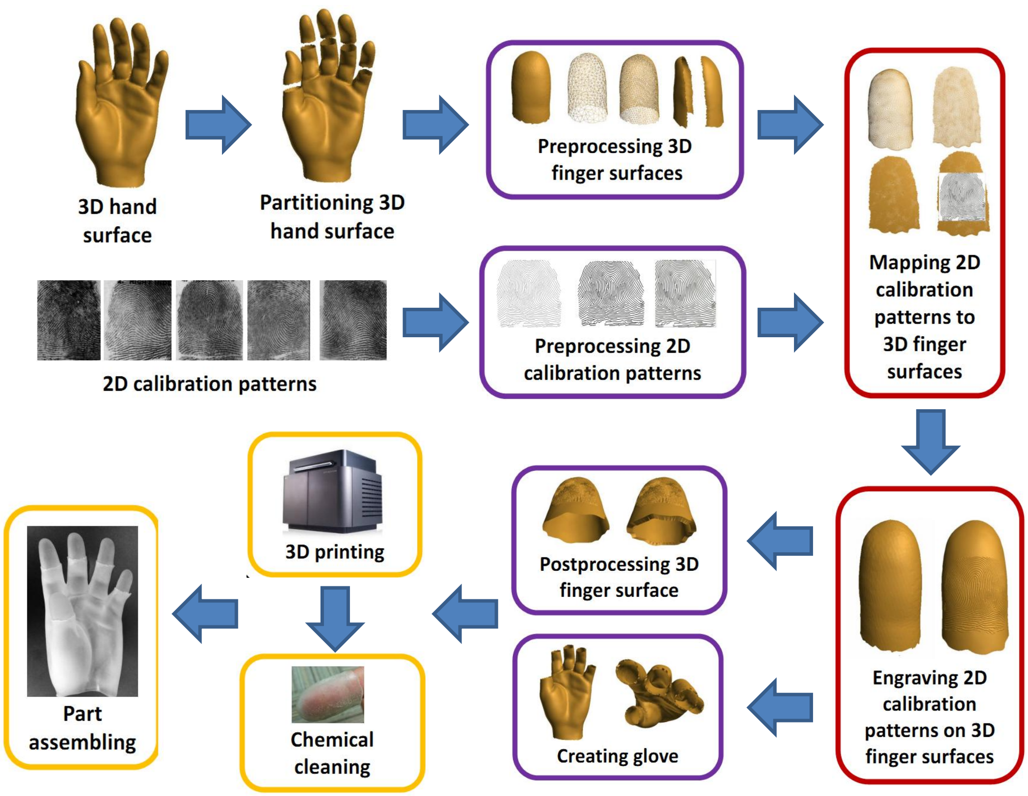

Figure 5.4 Generating a 3D whole hand target from a generic 3D hand surface and a set of 2D calibration patterns.

reader. This material provides optimum contrast between fingerprint ridges and valleys for imaging the target with the contactless slap reader.

5.2 Generating Whole Hand Target

Let a generic electronic 3D hand surface be denoted by H. Assume that the electronic surface H is a triangular mesh with a set of vertices V_H and a set of triangles T_H. Each vertex, v, in V_H has (x, y, z) coordinates corresponding to its spatial location in H, and each triangle in T_H connects a unique set of three vertices in V_H. As mentioned earlier, the whole hand target W is generated from H in parts. Assume that the 2D calibration pattern to be projected onto the i^{th} finger in H is

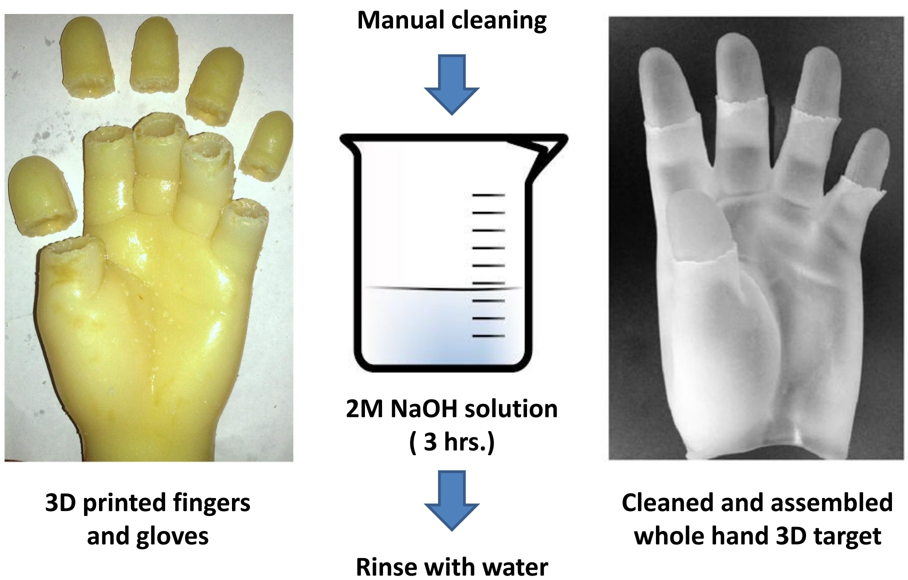

Figure 5.5 Cleaning and assembling the 3D printed fingers and gloves to create a whole hand 3D target.

denoted by I_i ($i = \{1 \ldots 5\}$). The complete process to create the whole hand target W, given H and the set of 2D calibration patterns I, is described below (see Fig. 5.4).

1. **Partitioning 3D hand surface**: The electronic hand surface H is divided into six different parts: the four fingers S_i (i=$\{1 \ldots 4\}$), the thumb S_5, and the remaining middle portion M of the hand surface, which can be described as a *fingerless glove*. The selector tool in open-source 3D mesh processing software Meshlab [15] is used for selecting the different parts. A new mesh layer is then created for each selected part. The registration of the six parts with respect to each other remains intact while partitioning the hand surface. This facilitates assembly of the fabricated parts to create the whole hand target. Assume that the set of vertices and triangles present in each 3D finger surface S_i is denoted by V_i and T_i, respectively. Also, let $I_i(u, v)$ denote the grayscale value at spatial coordinates (u, v) in the calibration pattern I_i.

2. **Preprocessing 3D finger surfaces**: Electronic finger surface S_i is aligned such that the finger length is along the y-axis in S_i. The surface S_i is re-meshed by sampling vertices from the set V_i based on the curvature of S_i [167]. Surface re-meshing reduces the density of S_i, therefore, S_i is subdivided using Loop's method [136] to ensure sufficient fidelity during projection of the 2D calibration pattern I_i. S_i is displaced outwards along the direction of the surface normals computed at each vertex v to create an outer finger surface S_i^O. Note, however, that the original electronic finger surface S_i is retained. The front portion S_i^{OF} and the rear portion S_i^{OR} of S_i^O are separated as only the front portion S_i^{OF} is used for projection.

3. **Preprocessing 2D calibration patterns**: If the pattern I_i being projected is a 2D fingerprint image, skeleton I_i^S of the image I_i is created. The ridge width of the skeleton I_i^S is increased using morphological operations, and the image is smoothed using a Gaussian filter before projecting it onto the frontal surface S_i^{OF}. This preprocessing step is important to ensure that ridges and valleys present in I_i are engraved smoothly onto S_i^{OF}. Note that preprocessing is not needed if any other 2D calibration pattern (e.g. sine grating) is being projected.

4. **Mapping 2D calibration patterns to 3D finger surfaces**: The front portion S_i^{OF} of the outer surface S_i^O is projected to 2D using the ISOMAP algorithm [177]. Rotation and flip are corrected using corresponding control points between front portion S_i^{OF} and the 2D projection of S_i^{OF}. Translation correction is done using the reference coordinates computed from I_i. The front portion S_i^{OF} is further subdivided depending on the resolution of I_i to ensure sufficient fidelity (high similarity scores for a FAR of 0.01%) of mapping I_i. Thereafter, the mapping between the vertex locations (x, y, z) on the front portion S_i^{OF} and the grayscale values at locations (u, v) in I_i is ascertained.

5. **Engraving 2D calibration patterns on 3D finger surfaces**: Ridges and valleys are engraved on S_i^{OF} by displacing the vertices on the front portion S_i^{OF} along the surface normals according to the texture values at the mapped (u, v) locations in I_i.

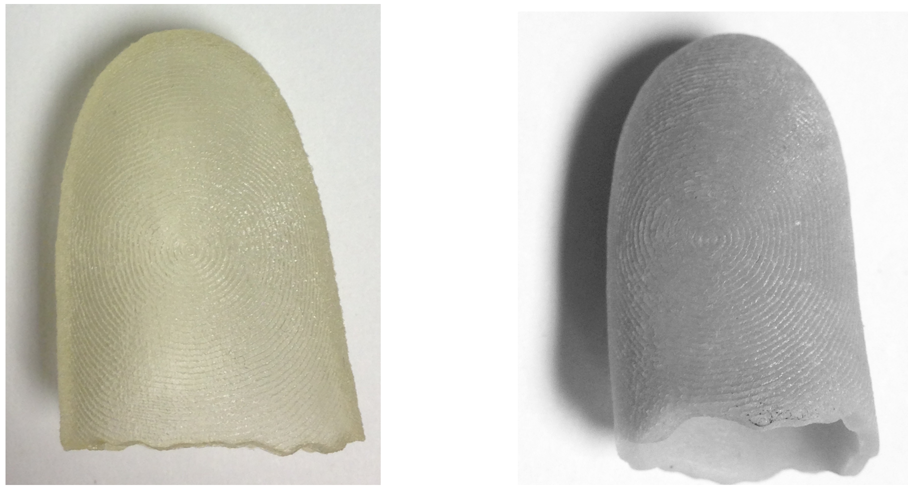

(a) (b)

Figure 5.6 Sample single-finger 3D targets fabricated for (a) contact-based readers (using translucent rubber-like material FLX9740-DM [30]) and (b) contactless readers (using rigid opaque material RGD8520-DM [30]).

6. **Postprocessing 3D finger surfaces**: The front and rear portions of the outer finger surface S_i^O are combined. The original finger surface S_i is made as dense as the outer finger surface S_i^O and then the two surfaces are stitched together to create the 3D target A_i in electronic (virtual) form.

7. **Creating glove**: The middle portion M of the hand is displaced outward along the surface normals computed at each vertex v to create an outer replica M^O of M. M and M^O are then stitched together to create a wearable glove M^W. This finishes the creation of the six parts of the whole hand target in electronic form.

8. **3D Printing**: The thumb and four finger targets A_i and the glove M^W are physically fabricated using a 3D printer (Stratasys Objet350/500 Connex). Two different printing materials, TangoPlus FLX930 [31] and FLX9740-DM [30], are used to fabricate the thumb and four finger targets A_i as well as the glove M^W for contact-based slap fingerprint readers (see, e.g., Figure 5.6 (a)). These materials are semi-translucent whitish rubber-like materials with similar hardness and elasticity as human skin (see Table 5.1). Unlike the black rubber-like materials earlier, these materials are optically suitable for imaging with a variety of contact-

Table 5.1 Comparison of the mechanical properties of the three printing materials used for 3D whole hand target fabrication with the human skin. TangoPlus FLX930 and FLX9740-DM are rubber-like materials similar in mechanical properties to the human skin and are suitable for use with contact-based slap readers. RGD8520-DM is a rigid opaque material that provides optimum fingerprint ridge-valley contrast for use with the contactless slap reader.

Property	**Human Skin [88] [89]**	**TangoPlus FLX930 [31]**	**FLX9740-DM [30]**	**RGD8520-DM [30]**
Shore A hardness	20-41	26-28	35-40	N.A.
Tensile Strength (MPa)	5-30	0.8-1.5	1.3-1.8	40-60
Elongation at Break (%)	35-115	170-220	110-130	15-25

based optical fingerprint readers. A bluish-gray rigid opaque material, RGD8520-DM [30], is used to manufacture the individual thumb and finger targets A_i for the contactless slap reader (see Table 5.1 and Figure 5.6 (b)). This material provides optimum contrast between fingerprint ridges and valleys for imaging with the contactless slap reader. The wearable glove M^W for the contactless slap reader is fabricated with TangoPlus FLX930.

9. **Chemical Cleaning**: The majority of the printer support material is removed manually from the 3D printed parts. After this, the 3D printed parts are soaked in 2M NaOH solution for 3 hours, and then rinsed with water to remove the printer support material residue (Figure 5.5).

10. **Part Assembling**: The cleaned physical parts A_i $(i = 1 \ldots 5)$ and M^W are assembled together with superglue to generate a wearable whole hand target W.

5.3 Fidelity of 3D Whole Hand Target Generation

To ascertain the fidelity[8] of the whole hand target creation process, we assess how well the features present in the 2D calibration patterns are replicated on the electronic 3D hand target after the 2D to 3D projection of the patterns, and on the physical 3D hand target post 3D printing and

[8] *Fidelity* means the degree of exactness with which the 2D calibration patterns are reproduced on the electronic and physical 3D hand target.

cleaning. We create a right hand target using five different rolled fingerprints from NIST SD4 [19]. Two samples of the whole hand target are fabricated with the two printing materials, TangoPlus FLX930 and FLX9740-DM. Five different slap impressions of the hand target are captured using three different *Appendix F* certified contact-based slap readers, SR1, SR2 and SR3[9] (see, e.g., Fig. 5.7). SR1 and SR3 are 500 ppi readers whereas SR2 is a 1000 ppi reader. Comparisons between (i) 2D fingerprints from NIST SD4 and the frontal images of corresponding fingerprints engraved on the electronic 3D hand target, (ii) frontal images of fingerprints engraved on the electronic 3D hand target to corresponding plain prints extracted from slap impressions of the physical 3D hand target, and (iii) the 2D fingerprints used to generate the hand target to corresponding plain prints extracted from slap impressions of the physical 3D hand target, are made to ascertain the fidelity of the 3D whole hand target generation process. Furthermore, plain prints extracted from five different slap impressions of the 3D hand target are compared with each other to determine the consistency between different impressions of the target (intra-impression variability). Verifinger 6.3 SDK [146] is used for conducting all comparison experiments. All slap impressions are upsampled by a factor of 1.2 using bicubic interpolation to account for reduction in ridge spacing due to 2D to 3D projection and 3D printing before conducting matching experiments (see Sections 4.3.1 and 4.3.1, respectively, for 2D to 3D projection and 3D printing fabrication error measurements).

5.3.1 Replication of 2D calibration pattern features on electronic 3D hand target

Frontal images of individual fingerprints engraved on the electronic 3D hand target are captured using Meshlab [15]. They are rescaled manually to approximately the same scale as the 2D fingerprints from NIST SD4. Each individual fingerprint image from the electronic 3D target is compared to the corresponding 2D fingerprint from NIST SD4. Table 5.2 shows the similarity scores obtained for this experiment. All similarity scores are significantly above the verification

[9]Vendor names are not provided to maintain their anonymity in this evaluation.

Figure 5.7 Sample slap impression of the 3D whole hand target captured using a contact-based slap reader.

Table 5.2 Similarity scores between frontal images (2D) of individual fingerprints engraved on the electronic 3D hand target captured in Meshlab and the corresponding 2D fingerprint images from NIST SD4 used for target generation. Verifinger 6.3 SDK was used for generating similarity scores. The threshold on scores @FAR = 0.01% is 33.

Fingerprint	S0005 (index)	S0043 (middle)	S0083 (ring)	S0096 (little)	S0044 (thumb)
score	203	150	399	183	249

threshold of 33 @FAR=0.01% for NIST SD4. This demonstrates that the features present in the 2D calibration patterns are replicated with high fidelity on the electronic 3D hand target.

5.3.2 Replication of electronic 3D hand target features on physical 3D hand target

Individual plain prints are manually extracted (for convenience) from the slap impressions captured using the three contact-based slap readers. Each plain print is compared to the frontal image of the corresponding fingerprint engraved on the electronic 3D hand target. All similarity scores are well

Table 5.3 Similarity scores between the frontal images (2D) of the individual fingerprints engraved on the electronic 3D hand target and the corresponding plain prints extracted from a slap image of the physical 3D hand targets captured by each of the three contact-based slap readers (SR1, SR2 and SR3). Physical targets were fabricated with two different materials (TangoPlus FLX930 and FLX9740-DM). Verifinger 6.3 SDK was used for generating similarity scores. The threshold on scores @FAR = 0.01% is 33.

TangoPlus FLX930

Fingerprint	**SR1 (500 ppi)**	**SR2 (1000 ppi)**	**SR3 (500 ppi)**
S0005 (index)	87	68	168
S0043 (middle)	66	71	122
S0083 (ring)	327	171	158
S0096 (little)	173	141	108
S0044 (thumb)	65	69	93

FLX9740-DM

Fingerprint	**SR1 (500 ppi)**	**SR2 (1000 ppi)**	**SR3 (500 ppi)**
S0005 (index)	147	159	78
S0043 (middle)	48	201	107
S0083 (ring)	362	441	222
S0096 (little)	140	156	129
S0044 (thumb)	63	62	50

above the verification threshold of 33 @FAR=0.01% for NIST SD4 (see Table 4.5). This shows that features engraved on the electronic 3D target are preserved post 3D printing and cleaning.

5.3.3 Replication of 2D calibration pattern features on physical 3D hand target

Plain prints extracted from the slap impressions of the physical 3D hand target, captured using the three contact-based slap readers, are compared to corresponding 2D fingerprints from NIST SD4. Table 5.4 shows the similarity scores obtained for this experiment. Because all similarity scores are well above the verification threshold score of 33 @FAR=0.01% for NIST SD4, it can be inferred

Table 5.4 Similarity scores between the plain prints extracted from slap impressions captured by the three contact-based readers (SR1, SR2 and SR3) of the physical 3D hand targets and the corresponding fingerprints from NIST SD4 used in their generation. Physical targets were fabricated with two different materials (TangoPlus FLX930 and FLX9740-DM). Verifinger 6.3 SDK was used for generating similarity scores. The threshold on scores @FAR = 0.01% is 33.

TangoPlus FLX930

Fingerprint	**SR1 (500 ppi)**	**SR2 (1000 ppi)**	**SR3 (500 ppi)**
S0005 (index)	549	141	321
S0043 (middle)	213	161	315
S0083 (ring)	441	374	411
S0096 (little)	308	392	423
S0044 (thumb)	209	422	345

FLX9740-DM

Fingerprint	**SR1 (500 ppi)**	**SR2 (1000 ppi)**	**SR3 (500 ppi)**
S0005 (index)	719	570	510
S0043 (middle)	221	579	357
S0083 (ring)	426	596	303
S0096 (little)	419	510	366
S0044 (thumb)	119	404	371

that the 2D calibration pattern features are replicated with high fidelity on the physical 3D hand target.

5.3.4 Consistency between different impressions of the physical 3D hand target

Individual plain prints extracted from different slap impressions of the same physical 3D hand target are compared with each other to measure their intra-class similarity. Similarity scores for this experiment are reported in Table 5.5. All similarity scores are significantly above the verification

Table 5.5 Range of similarity scores for pairwise comparisons between plain prints of the same finger extracted from five different slap prints captured by the three contact-based slap readers (SR1, SR2 and SR3) of the same 3D whole hand target. Results are shown for two physical hand targets fabricated with the two printing materials (TangoPlus FLX930 and FLX9740-DM). Verifinger 6.3 SDK was used for generating similarity scores. The threshold on scores @FAR = 0.01% is 33.

TangoPlus FLX930

Fingerprint	**SR1 (500 ppi)**	**SR2 (1000 ppi)**	**SR3 (500 ppi)**
S0005 (index)	839-1373	603-1193	797-1434
S0043 (middle)	551-930	501-909	581-1206
S0083 (ring)	756-1127	843-1290	990-1272
S0096 (little)	644-1071	344-1133	957-1413
S0044 (thumb)	800-1061	743-1263	989-1160

FLX9740-DM

Fingerprint	**SR1 (500 ppi)**	**SR2 (1000 ppi)**	**SR3 (500 ppi)**
S0005 (index)	980-1359	735-1271	779-1229
S0043 (middle)	579-1079	855-1265	539-1190
S0083 (ring)	837-1254	924-1467	897-1503
S0096 (little)	639-1043	710-1059	630-1221
S0044 (thumb)	723-1178	845-1796	822-1469

threshold score of 33 @FAR=0.01% indicating that multiple slap impressions of the same 3D hand target are highly consistent.

5.4 Evaluating Contact-based Slap Fingerprint Readers

Center-to-center ridge spacing measurements are computed (using the method proposed in [104]) in the plain prints extracted from five different slap impressions captured using the three contact-based slap readers. We compare these measurements against the expected average center-to-center ridge spacing in the corresponding 2D fingerprints used during target creation. The expected ridge spacing is computed taking into consideration the 2D to 3D projection error (5.8%) and the 3D

Table 5.6 Mean (μ) and std. deviation (σ) of center-to-center ridge spacings (in pixels) in the plain prints extracted from five different slap images of the 3D whole hand targets captured using the three contact-based slap readers (SR1, SR2 and SR3). Expected average ridge spacing (in pixels) for each 2D fingerprint from NIST SD4 is shown in brackets. The spacing measurements take into consideration the reduction in spacing due to 2D to 3D projection and 3D printing fabrication errors.

TangoPlus FLX930

Fingerprint	SR1 (500 ppi)	SR2 (1000 ppi)	SR3 (500 ppi)
index (7.82)	μ = 8.06, σ = 0.10	μ = 7.87, σ = 0.06	μ = 7.90, σ = 0.05
middle (8.33)	μ = 8.64, σ = 0.03	μ = 8.57, σ = 0.06	μ = 8.35, σ = 0.08
ring (8.62)	μ = 8.58, σ = 0.05	μ = 8.65, σ = 0.10	μ = 8.65, σ = 0.07
little (8.47)	μ = 8.49, σ = 0.07	μ = 8.49, σ = 0.10	μ = 8.49, σ = 0.04
thumb (7.67)	μ = 7.67, σ = 0.04	μ = 7.66, σ = 0.06	μ = 7.67, σ = 0.06

FLX9740-DM

Fingerprint	SR1 (500 ppi)	SR2 (1000 ppi)	SR3 (500 ppi)
index (7.82)	μ = 7.87, σ = 0.08	μ = 7.80, σ = 0.08	μ = 8.00, σ = 0.08
middle (8.33)	μ = 8.61, σ = 0.09	μ = 8.64, σ = 0.05	μ = 8.36, σ = 0.05
ring (8.62)	μ = 8.63, σ = 0.14	μ = 8.66, σ = 0.03	μ = 8.64, σ = 0.10
little (8.47)	μ = 8.52, σ = 0.10	μ = 8.51, σ = 0.14	μ = 8.54, σ = 0.08
thumb (7.67)	μ = 7.66, σ = 0.07	μ = 7.66, σ = 0.03	μ = 7.67, σ = 0.05

printing fabrication error (11.42%) that were estimated in Sections 4.3.1 and 4.3.2, respectively. Table 5.6 lists the measurements taken from slap impressions of the two hand targets. Following are some observations based on this experiment:

- The estimated ridge spacings in slap impressions of the hand targets captured using the three contact-based slap readers, SR1, SR2 and SR3 are, on average, within 0.08 pixels of each other. In other words, all three slap readers SR1, SR2 and SR3 perform equally well in preserving fingerprint ridge spacing.

- The estimated ridge spacings in the plain prints of index, middle, ring and little fingers are, on average, marginally greater than the expected ridge spacing. Although the increase in ridge spacings is not as significant as that reported previously for single-finger 3D targets, it is consistent with our observation. This increase in ridge spacing is due to the flattening of the finger skin because of the pressure applied on the reader platen while capturing fingerprints. For the thumb, however, this flattening effect is not observed to be as profound compared to the other fingers, and does not seem to impact the ridge spacing measurements. One possible reason could be the difference in pressure on the reader platen for each finger while capturing slap impressions. Further, using the one-sample t-test [151], for all fingers except the middle finger, the estimated ridge spacing values are statistically similar to the expected values at significance level of 0.05. This is in contrast to our observation in chapter 4 for single-finger optical readers where estimated values were statistically different compared to expected values. A better understanding of the underlying cause would require controlled experimentation where known contact pressure is applied by each finger during fingerprint capture. This is a topic of future research.

- Choice of fabrication material of the hand target does not seem to significantly impact the ridge spacing measurements in fingerprint images captured using the three slap readers.

5.5 Evaluating Contactless Slap Fingerprint Reader

The contactless slap reader used in our experiment is a *PIV* certified 500 ppi reader that captures a 512×512 image of each fingertip from a single wave of the hand. Therefore, for evaluating the contactless slap reader, we generated a right whole hand target by projecting circular sine gratings of fixed ridge spacing (10 pixels) such that they cover the entire fingertip[10]. The rigid opaque material RGD8520-DM was used to fabricate the thumb and four finger targets whereas rubber-like flexible material TangoPlus FLX930 was used to manufacture the fingerless glove so that it is easy to wear. Five different slap impressions of the whole hand target were captured using the contactless slap reader (see, e.g., Fig. 5.8). Analogous to the earlier experiment, center-to-center ridge spacing measurements are computed in the plain prints extracted from five different

[10] We are designing a method to do a similar projection for fingerprints.

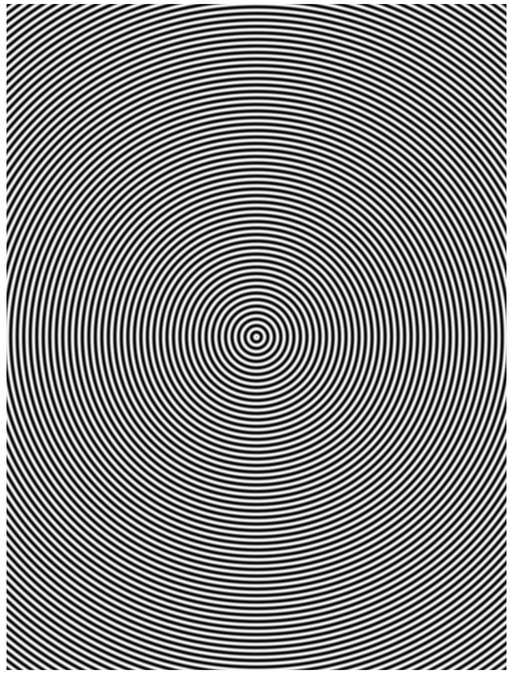

(a)

(b)

Figure 5.8 Circular sine grating (ridge spacing = 10 pixels) used to generate the 3D whole hand target (shown in (a)) and the slap impression of the corresponding hand target captured using the contactless slap reader (shown in (b)). The circular sine grating appears to exhibit the moire effect [16].

Table 5.7 Mean (μ) and std. deviation (σ) of center-to-center ridge spacings (in pixels) in the plain prints extracted from five different slap images of the circular grating whole hand target captured using the contactless slap fingerprint reader (CR). Expected average ridge spacing (in pixels) of the circular grating engraved on the hand target is 8.28. The spacing measurements take into consideration the reduction in spacing due to 2D to 3D projection and 3D printing fabrication errors.

RGD8520-DM

Fingerprint	**CR (500 ppi)**
index	$\mu = 8.12$, $\sigma = 0.16$
middle	$\mu = 8.35$, $\sigma = 0.10$
ring	$\mu = 8.28$, $\sigma = 0.15$
little	$\mu = 8.03$, $\sigma = 0.15$
thumb	$\mu = 7.67$, $\sigma = 0.08$

slap impressions captured using the contactless slap reader. We compare these measurements against the expected average center-to-center ridge spacing in the circular gratings used during target creation. The expected ridge spacing takes into consideration the 2D to 3D projection error (5.8%) and the 3D printing fabrication error (11.42%). Table 5.7 lists the measurements taken from contactless slap impressions of the hand target. Following are some observations based on this experiment:

- The average deviation in estimated center-to-center ridge spacings in slap impressions of the circular grating hand target is about 0.25 pixels from the expected ridge spacing. Using one sample t-test [151], the estimated spacings are statistically different than expected spacings for all but one finger. Further analysis is needed to interpret this measurement and understand, in more details, the effects of the unconstrained nature of contactless fingerprint capture, the size of the captured area as well as the nature of the material used to create the target.

- The estimated ridge spacings in the plain prints of index, middle, ring and little fingers are, on average, closer to the expected ridge spacing compared to the thumb. This may be because the four fingers are captured together in a slap impression whereas thumb is captured individually as a separate impression, and the user dynamics involved in the two capture processes (e.g. finger alignment with respect to the optical capture, relative finger movement) are quite different. Controlled experimentation where the relative positioning of the user's fingers/hand with respect to the reader is fixed at the time of contactless slap capture is required to investigate this further. It is a topic of future research.

5.6 Conclusions

We have presented a method to design and fabricate whole hand 3D targets for evaluating multi-finger capture devices, e.g., contact-based and contactless slap fingerprint readers. 2D calibration patterns of known characteristics (e.g. fingerprints of known ridge flow and ridge spacing, sine gratings of known orientation and center-to-center spacing) are projected onto a generic 3D hand model to create an electronic 3D hand target. Physical 3D hand target is fabricated from the electronic target using a state-of-the-art 3D printer. Material(s) similar in hardness and elasticity to the human skin as well as optically suitable for use with a variety of fingerprint readers are used for 3D hand target fabrication. Our experimental results show that features present in the 2D calibration patterns are replicated with high fidelity both on the electronic and physical 3D hand target during the 3D hand target generation process. We also conduct experiments to evaluate three *Appendix F* certified slap readers and a *PIV* certified contactless slap reader using the fabricated 3D hand targets. To the best of our knowledge, this is the first study that demonstrates the utility[11] of the wearable 3D hand targets for evaluation of slap readers, both contact and contactless.

[11] Wearable finger spoofs were used to spoof a fingerprint based security system in the CBS crime thriller TV show Person of Interest's Season 3 episode 14 titled Provenance (https://www.youtube.com/watch?v=mzfDG2wmqc4). Our research has shown that this is now possible in reality!

Chapter 6

Generating 3D Conductive Fingerprint Targets

6.1 Introduction

There are, at present, over 2 billion smartphone users worldwide, and it is estimated that the user base will grow to around 2.66 billion by 2019, *i.e.*, within the next few years, every third person in the world will be using a smartphone [28]. Following the introduction of fingerprint-based smartphone unlock and payment technology by major vendors (e.g., Apple, Samsung and Google), a large number of these users now use smartphones equipped with fingerprint readers. One of the primary reasons of the increasing use of fingerprint-based authentication on smartphones is the relative ease of use and higher security of fingerprint-based technology compared to traditional authentication mechanisms such as passcodes. In 2016, about 29% of the smartphones that were shipped had a fingerprint reader, and this number is expected to more than double in the next two years. It is estimated that in 2018, two out of every three shipped smartphones will have a fingerprint reader [29]. Further, the number of users using Near Field Communication (NFC) technology for mobile phone payments is expected to triple from about 54 million in 2016 to 166 million in 2018 [27].

(a) (b)

Figure 6.1 3D targets for evaluating capacitive readers. (a) Sample (*goldfinger*) target, and (b) an impression of the goldfinger in (a) captured using a *PIV* certified 500 ppi single-finger capacitive reader.

The embedded fingerprint readers on most smartphones, including those from major vendors (Apple iPhone [36], Samsung Galaxy S [25] and Google Nexus[1]), use capacitive sensing. Capacitive readers typically consist of a silicon plate, where each element of the plate is a mini-sensor in itself that senses the capacitance difference between ridges and valleys. Typically, they have a small form factor, with the sensing area between 5-8 cm^2, to keep the reader cost low. The small form factor coupled with low cost makes capacitive readers suitable for embedding on mobile devices including smartphones, laptops and tablets. In addition, capacitive readers have also been embedded in standalone terminals for access control.

In chapter 4, we designed and fabricated 3D targets for operational evaluation of single-finger optical fingerprint readers. We projected 2D calibration patterns with known features, e.g., sine gratings generated with predefined orientation and spacing, synthetic fingerprints with known fingerprint type, ridge flow, ridge spacing and minutiae points, onto a generic 3D finger surface to create electronic 3D targets. A state-of-the-art 3D printer was used for physical fabrication of the

[1] www.google.com/nexus/

Table 6.1 Mechanical and electrical properties of human skin.

Property	Description/Benefit	Human Skin
Hardness [88] [89]	Proper presentation on the reader platen	20-41 (Shore A)
Tensile Strength [88]	Durability for repeatable operational evaluation	5-30 MPa
Elongation at Break [88]	Pertinent distortion on contact with the reader platen	35-115 %
Electrical Resistance [72] [127]	Resistance to flow of electric charge	˜1-2 MΩm

3D targets with materials similar in hardness and elasticity to the human skin. We showed that the 3D target synthesis and fabrication process was able to reproduce calibration patterns with high fidelity on both electronic and physical 3D targets. We also performed evaluation of three different single-finger optical readers using the fabricated targets.

Subsequently, in chapter 5, we extended the single-finger target generation method to create whole hand 3D targets for evaluating contact-based and contactless slap fingerprint readers. We segmented 3D finger surfaces pertaining to each of the four fingers and the thumb from a 3D hand surface and projected calibration patterns onto each finger surface to generate electronic 3D whole hand target. We used a high-resolution 3D printer to manufacture physical 3D hand target with materials that were similar in mechanical properties to the human skin as well as compatible for imaging with a variety of optical fingerprint readers. Furthermore, we used the generated targets to evaluate three contact-based slap readers and one contactless slap reader.

Although suitable for use with optical readers, the 3D targets designed earlier were not compatible with capacitive readers as the fabrication materials used to print the 3D targets (UV-curable rubber-like polymeric materials: TangoBlackPlus FLX 980, FLX 9840-DM, TangoPlus FLX930 and FLX 9740-DM) were non-conductive. This is because state-of-the-art high-resolution 3D printers only support printing with limited rubber-like polymer materials and the supported materials are electric insulators.

Given that a large number of capacitive fingerprint readers are being used in consumer and access control applications, e.g., mobile phone unlock and payments (Apple Pay [1], Samsung Pay [26]), in this chapter we address the aforementioned limitation by designing and fabricating targets suitable for imaging with capacitive fingerprint readers (see Figure 6.1; also see Table 6.1 for the mechanical and electrical properties of the human skin). We first use the method proposed in chapter 4 to create 3D targets with materials similar in hardness and elasticity to the human skin. We then use a sputter deposition technique to coat the surface of 3D targets with thin layers of specific materials with conductive properties (titanium (Ti) + gold (Au)). We refer to the Ti-Au coated 3D targets as *goldfingers*. We show that the sputter deposition of 30 nm Ti + 300 nm Au does not significantly impact the features etched on the 3D targets. Further, we show that the coated 3D targets can be imaged with two different types of capacitive fingerprint readers: small area readers (~0.5 cm $\times$ 1.2 cm) designed for smartphones, and relatively larger area (~1.3 cm $\times$ 1.8 cm) readers designed for access control applications. In summary, the contributions of this chapter are as follows:

- Method to coat 3D printed targets with a thin layer of conductive materials (~300 nm) to impart appropriate electrical conductivity for the targets to be sensed by capacitive readers.

- Demonstrate both qualitatively and quantitatively that the coating process does not impact fingerprint features extracted from the 3D printed targets.

- Show the utility of the coated targets for evaluating standalone single-finger capacitive readers, as well as readers embedded in access control terminals and smartphones.

- Investigate the potential use of conductive 3D spoofs to evaluate spoof vulnerability of capacitive readers.

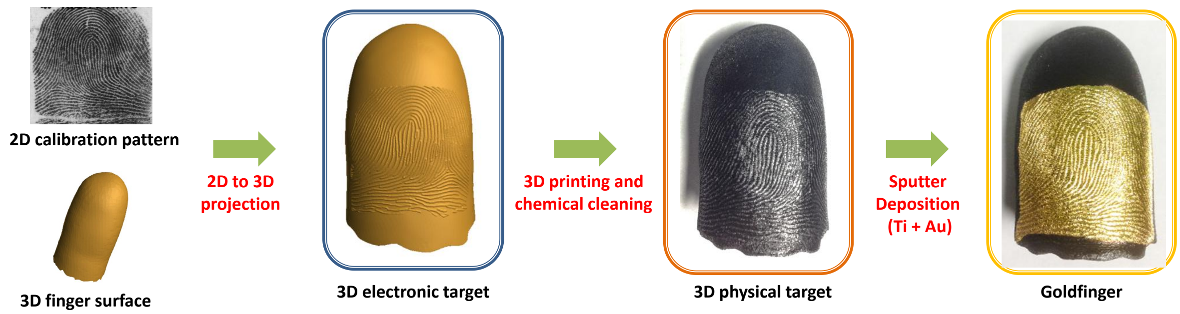

Figure 6.2 Main steps involved in creating a goldfinger given a 2D calibration pattern and a 3D finger surface.

6.2 Sputter Coating 3D Targets

We first generate 3D targets using the method detailed in chapter 4. 2D calibration patterns with known features (e.g. fingerprints with known minutiae locations, sine gratings with predefined orientation and spacing) are mapped onto an electronic 3D finger surface to create electronic 3D targets. Wearable physical 3D targets are fabricated using the Stratasys Objet Connex350 with materials similar in hardness and elasticity to the human skin (TangoBlackPlus FLX980 [31] and FLX 9840-DM [30]). Bulk of the printer support material is manually removed from the printed 3D targets. The targets are then dipped in a 2M solution of NaOH for approximately 3 hrs. and rinsed with water for complete removal of the support material residue.

Given the cleaned 3D targets, the DC sputter deposition technique [175] is used to coat their surface with thin layers of conductive materials. Figure 6.2 illustrates the main steps involved in generating a goldfinger given a 2D calibration pattern and a 3D finger surface. Sputter deposition is one of the most popular techniques for depositing thin conductive films on insulators and semi-conductors [171]. It is widely used in the semi-conductor industry to deposit thin films on integrated circuit components, for anti-glare coatings on glass in optical applications, and to deposit thin metallic layers on CDs, DVDs and solar cells [171]. Different types of sputter deposition methods, e.g., ion beam sputtering, DC sputtering, RF sputtering, can be used depending on the characteristics of the substrate and the target material to be deposited and the desired coating thick-

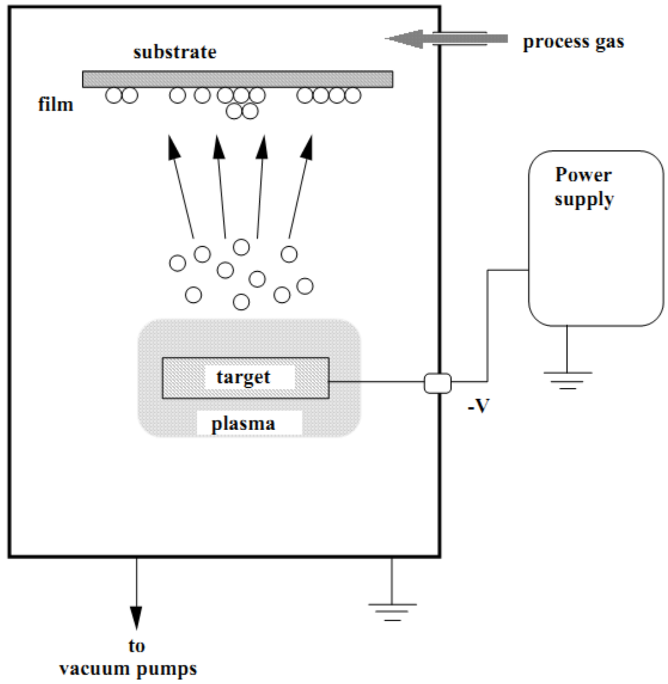

(a)

(b)

Figure 6.3 DC sputter deposition to coat the 3D targets with thin layers of conductive materials. (a) Simplified representation of the DC sputtering process (image reproduced from [175]), and (b) the Denton Vacuum DC sputtering system [4] used for DC sputtering. Titanium (Ti) and Gold (Au) ions from the cathode target are deposited on the anode substrate using Argon (Ar) as the process gas.

ness. Here, we use DC sputtering because this method is both suitable and efficient for applying conductive material coatings on 3D printed targets.

6.2.1 DC Sputtering Process

Figure 6.3 (a) illustrates the DC sputtering process [175]. The sputtering chamber is first vacuumed to evacuate potential contaminants, e.g, water vapour and atmospheric gases, that could interfere with the sputtering process. The sputtering target made of the material to be deposited (e.g. silver (Au), Copper (Cu), or Gold (Au)) is placed at the cathode, and the substrate on which the thin layer has to be deposited is placed at the anode. A process gas (typically Argon (Ar)) is then added to the vacuumed chamber at a pre-specified pressure, typically between 1-100 mTorr. A negative potential bias that is sufficient for electron emission from the sputtering target (generally between 500-5000 V DC) is applied to the cathode. Electrons emitted from the target due to this negative bias strike the molecules of the process gas in the neighborhood of the cathode (sputtering target) and produce positively charged process gas ions. The generated positive gas ions travel towards the cathode due to the negative potential bias. When the process gas ions collide with the cathode (sputtering target), their kinetic energy is transferred to the target resulting in the emission of sputtering material atoms. The ejected material atoms move towards the anode where they condense to form a thin layer on the substrate surface.

6.2.2 Choice of Sputtering Materials

We initially sputter coated other metals, e.g., silver (Ag), copper (Cu), and chromium (Cr)) on the 3D targets post the Ti coating (see, e.g, Figure 6.4 (a) and (b)). Although coatings of these metals were found to be sufficiently conductive for the 3D targets to register on capacitive readers, the metal coatings would react with atmospheric gases and water vapours over time to form compounds with low electrical conductivity (e.g. copper carbonate ($CuCO_3$) and chromium oxide (Cr_2O_3)) on the 3D target surface. This would render the 3D targets unusable with capacitive readers.

(a) (b) (c)

Figure 6.4 3D fingerprint targets coated with (a) and (b) a thin layer (300 nm) of silver (Ag) and copper (Cu), respectively over a thin layer (30 nm) of titanium (Ti), and (c) 100 nm of tin (Sn) doped indium oxide (ITO). The targets in (a) and (b) were printed with TangoBlackPlus FLX980 [31] and the target in (c) was printed with TangoPlus FLX930 [31]. Targets coated with other conductive transparent oxides are not shown here because they are visually similar to (c).

We also attempted to coat transparent conductive oxides, e.g, Tin (Sn) doped Indium Oxide (ITO) [62], Zinc (Zn) and Al doped Indium Oxide (IZAO) [73], and Sn, Zn and Al doped Indium Oxide (IZATO) [106] on 3D printed targets using DC sputtering (see, e.g, Figure 6.4 (c)). The primary advantage of using transparent conductive oxide coatings over metallic coatings is their high transparency which preserves the underlying optical properties [58] of the 3D targets. However, the wear and tear (abrasion resistance) of conductive oxide coatings was found to be inadequate for repeatable evaluation of capacitive readers over time. In our tests, the coatings were found to wear out after taking about 5-10 impressions of the coated targets with capacitive readers. Based on this experimental observation, we formulated the following two hypothesis for low abrasion resistance of conductive oxide coatings: (i) surface of the 3D printed targets is not receptive of conductive oxide coatings and requires some pre-treatment before sputtering, or (ii) the coatings cannot be cured, e.g., using high temperature annealing post DC sputtering because the 3D printing materials are sensitive to high temperatures ($\geq 60^\circ$ C). To increase the receptivity of the 3D target surface to

Table 6.2 Qualitative comparison of different thin film coatings applied on 3D targets using DC sputtering.

Coating	Thickness	Conductivity	Stability in air	Abrasion Resistance
Ti + Au	30 nm + 300 nm	Adequate	High (doesn't react)	Moderate
Ti + Ag	30 nm + 300 nm	Adequate	Low (~1 week)	Moderate
Ti + Cu	30 nm + 300 nm	Adequate	Low (~2 weeks)	Moderate
Cr	300 nm	Adequate	Low (~1-2 days)	Moderate
ITO	100 nm	Adequate	High (doesn't react)	Low
IZAO	300 nm	Adequate	High (doesn't react)	Low
IZATO	300 nm	Adequate	High (doesn't react)	Low

conductive oxide coatings, we attempted to pre-treat the 3D target surface with high energy plasma for a short duration of time before sputtering ITO. However, the 3D printing materials were found to be highly sensitive to this pre-treatment and the high energy plasma impacted the calibration patterns etched on the 3D surface. Further investigation is required to identify the exact underlying cause which is a topic of future research.

We also experimented with the application of a thin layer (50 nm) of poly(3,4-ethylenedioxythiophene):poly(styrenesulfonate) (PEDOT:PSS) colloidal solution on a 3D target using spin coating (at 2000 rpm). However, the conductivity of the sample was found to be inadequate for registration on capacitive readers. Exploration of methods to improve the conductivity of PEDOT:PSS (e.g., [176], [48]) before its coating on 3D targets is a topic of future research.

Based on the results of our initial experimentation, Au was specifically chosen for coating 3D targets because it is an inert metal that does not react with atmospheric gases and Au coating has relatively high abrasion resistance. Table 6.2 lists the advantages and disadvantages of applying different conductive coatings on 3D fingerprint targets using DC sputtering.

6.2.3 Sputtering Ti+Au

The Denton Vacuum Desktop Pro [4] which is a compact, high vacuum sputtering system is used for DC sputtering (see Figure 6.3 (b)). The sputtering system has a rotary platform where the

(a) (b) (c)

Figure 6.5 3D mount fabricated to hold a 3D target for stable placement on the sputtering system's rotary platform. (a) Electronic 3D model, (b) 3D printed physical model and (c) 3D target on the mount shown in (b) after gold coating.

substrate to be coated needs to be placed and rotated in order to uniformly coat the substrate surface with the target material. Because directly placing the 3D targets on the rotary platform was found to be unstable, we fabricated a stable 3D mount to hold the 3D targets before placing them on the platform. The 3D mount is designed in Meshlab [15] by combining a generic 3D model of a finger with a rectangular base with dimensions of 35 mm $\times$ 37 mm $\times$ 10 mm (see Figure 6.5 (a)). The mount is 3D printed using the Stratasys Objet Connex350 with the rigid opaque white material, VeroWhite [31] (Figure 6.5 (b)). Each 3D target is mounted on this mount before sputtering. Further, the 3D target region without the etchings is covered with tape to only sputter target material on regions that contained the etched pattern, e.g, fingerprint pattern. This tape is removed after sputtering to obtain the coated 3D target analogous to that shown in Figure 6.1 (a).

Table 6.3 lists the experimental parameters used for DC sputtering. High purity (>99%) thick gold (Au) and titanium (Ti) sputtering targets with 2.00" diameter $\times$ 0.125" [12] [13] are used. Argon (Ar) is used as the process gas at a pressure of 4 mTorr. Power source of 125 W is used. 30 nm of Titanium (Ti) is first sputter deposited on the 3D printed samples because it has good adhesion/binding properties to the 3D printing material as well as gold (Au). This is followed by

Table 6.3 Parameter settings for Ti+ Au DC Sputtering.

Parameter	Value
Ar gas pressure	4 mTorr[1]
Power source	125 W[2]
Ti sputtering rate	0.21 nm/s
Ti layer thickness	30 nm[3]
Ti sputtering time	2.4 min
Au sputtering rate	1.1 nm/s
Au layer thickness	300 nm
Au sputtering time	5 min

[1] milliTorr; [2] Watts; [3] nanometers

sputter deposition of 300 nm of Au[2] on the 3D targets. The sputtering rates for Ti and Au at 125 V negative bias are 0.21 nm/s and 1.1 nm/s, respectively. At these sputtering rates, it takes about 2.4 minutes to sputter 30 nm Ti and about 5 minutes to sputter 300 nm Au. The estimated in-house cost of sputter coating each 3D target with 30 nm Ti and 300 nm Au, including labor, is approximately US \$2. Given that the cost to generate a physical 3D target is approximately US \$10, the total estimated cost to fabricate a goldfinger is about US \$12.

6.3 Impact of Sputter Coating on 3D Target Features

In chapter 4, we had demonstrated that the 2D calibration pattern features are replicated with high fidelity on electronic 3D targets after 2D to 3D projection and on fabricated physical 3D targets post 3D printing and cleaning. Because we sputter coat the cleaned 3D targets generated using the same method, we conduct fidelity assessment of friction ridge etchings on the *goldfingers* post sputter deposition with Ti and Au.

To conduct the fidelity experiments, we generate four different 3D targets by projecting different fingerprints (S0005, S0010, S0083, S0096) from NIST SD4 [19] onto a 3D finger surface.

[2]In contrast, the diameter of a human hair is an order of magnitude thicker (typically between 17-181 μm [5]).

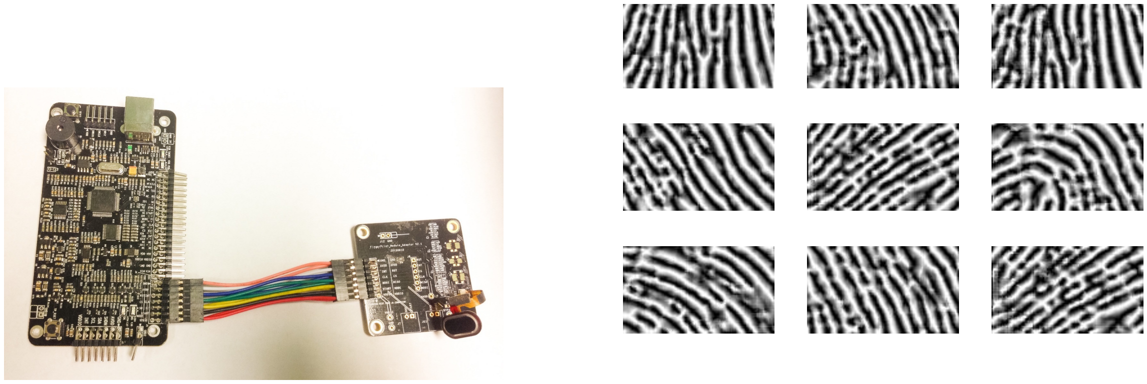

(a) (b)

Figure 6.6 Sample impressions shown in (b) of a goldfinger captured using the embedded capacitive reader designed for smartphones in (a).

Two of these targets (S0005, S0010) are fabricated with TangoBlackPlus FLX980 [31], and the other two (S0083 S0096) are fabricated with FLX 9840-DM [30]. In chapter 4, we had reported the reduction in etching spacings on physical 3D targets due to 2D to 3D projection (5.8%) and 3D printing (11.42%). We set the projection scale to 16.79 pixels/mm during 2D to 3D projection to account for these errors. Unlike our earlier method of accounting for these errors in distance measurements by upsampling the target images captured using fingerprint readers, this a priori projection scale adjustment ensures that spacings in the original 2D calibration patterns are maintained in the 3D target etchings post 2D to 3D projection and 3D printing. Further, the depth between ridges and valleys on the 3D targets is set to 0.24 mm.

A commercial 500 ppi *Appendix F* certified single-finger optical reader[3] is used to capture plain impressions of the physical 3D targets post 3D printing and cleaning, whereas a commercial 500 ppi *PIV* certified single-finger capacitive reader is used for capturing the plain impressions of the *goldfingers* post sputter deposition. Verifinger 6.3 [146], which is a commercially available fingerprint SDK, is used for conducting all fingerprint comparison experiments.

[3]The make and model of the readers used in the experiments cannot be disclosed because of proprietary reasons.

Table 6.4 Similarity scores between 500 ppi plain impression of fabricated physical 3D targets captured by the optical reader to 500 ppi plain impression of the corresponding sputter coated goldfingers captured by the capacitive reader. Physical 3D targets S0005 and S0010 were fabricated with TangoBlackPlus FLX980, and S0083 and S0096 were fabricated with FLX 9840-DM. Verifinger 6.3 SDK was used for generating similarity scores. The threshold on scores @FAR = 0.01% is 33.

Fingerprint	S0005	S0010	S0083	S0096
Score	764	810	680	708

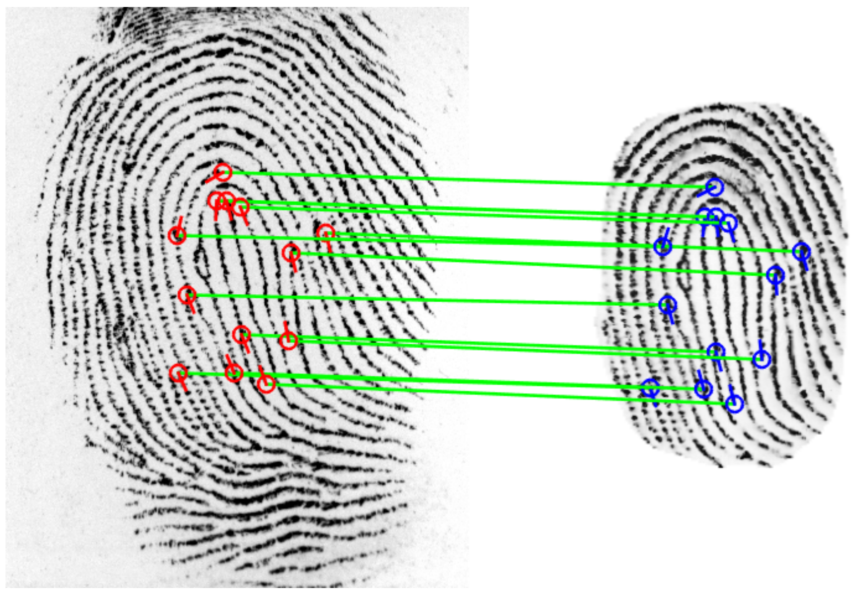

Figure 6.7 Minutiae correspondence between (a) plain impression of the 3D target generated using fingerprint image S0083 from NIST SD4 captured by the optical reader, and (b) plain impression of the same target captured by the capacitive reader (a). Similarity score of 680 is obtained between (a) and (b) which is above the threshold of 33 at 0.01% FAR.

6.3.1 Fidelity of physical 3D target features on goldfingers

Plain impressions of the physical 3D targets captured using the optical reader before sputter coating are compared to the plain impressions of the corresponding *goldfinger* captured using the single-finger capacitive reader after sputter deposition. This comparison of pre and post sputter deposition target images is used to assess how well the features on the physical 3D targets are preserved on *goldfingers* after sputter deposition. Table 6.4 shows the comparison results of this experiment. The similarity scores obtained for all comparisons are significantly above the verification threshold score of 33 computed for NIST SD4 at a fixed false accept rate (FAR) of 0.01%. This indicates

Table 6.5 Similarity scores between plain impressions of the sputter coated goldfingers captured using a 500 ppi capacitive reader to the corresponding 2D fingerprints from NIST SD4 used in their generation. Physical 3D targets S0005 and S0010 were fabricated with TangoBlackPlus FLX980, and S0083 and S0096 were fabricated with FLX 9840-DM. Verifinger 6.3 SDK was used for generating similarity scores. The threshold on scores @FAR = 0.01% is 33.

Fingerprint	S0005	S0010	S0083	S0096
Score	471	333	183	203

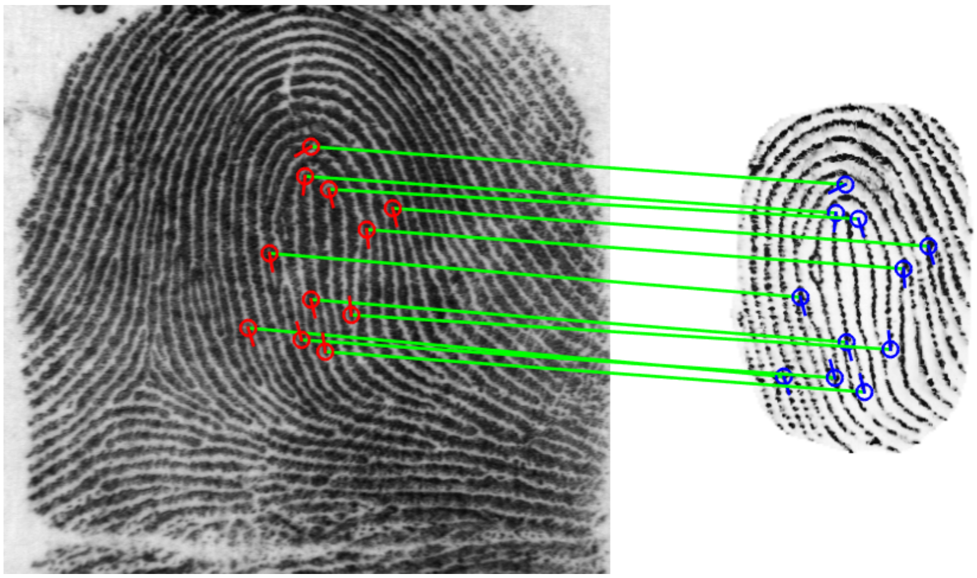

Figure 6.8 Minutiae correspondence between (a) rolled fingerprint image S0083 from NIST SD4, and (b) plain impression of the 3D target generated using (a) captured by the capacitive reader. Similarity score of 183 is obtained between (a) and (b) which is above the threshold of 33 at 0.01% FAR.

that features present on the physical 3D targets are replicated with high fidelity on the *goldfingers* post sputter deposition.

6.3.2 Fidelity of 2D calibration pattern features on goldfingers

Plain impressions of the *goldfingers* captured using the single-finger capacitive reader are compared to the corresponding 2D fingerprint images from NIST SD4 used in their generation. End-to-end fidelity of 2D calibration pattern features on goldfingers is assessed based on how well the 2D pattern features are replicated on the *goldfingers* post 3D printing, cleaning and sputter deposition. Table 6.5 shows the comparison results. For all comparisons, the similarity scores generated

Table 6.6 Range of similarity scores between five different 500 ppi plain impressions of each sputter coated goldfinger. Physical 3D targets S0005 and S0010 were fabricated with TangoBlackPlus FLX980, and S0083 and S0096 were fabricated with FLX 9840-DM. Verifinger 6.3 SDK was used for generating similarity scores. The threshold on scores @FAR = 0.01% is 33.

Fingerprint	S0005	S0010	S0083	S0096
Score range	926-1251	884-1164	824-1215	462-1008

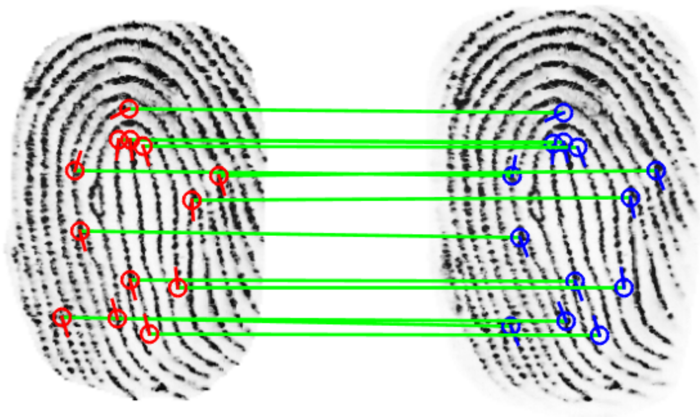

Figure 6.9 Minutiae correspondence between two different plain impressions (a) and (b) of the same 3D target generated using image S0083 from NIST SD4 captured by the capacitive reader. Similarity score of 1164 is obtained between (a) and (b) which is above the threshold of 33 at 0.01% FAR.

are above the verification threshold score of 33 for NIST SD4 at FAR of 0.01%. This demonstrates that the 2D calibration pattern features were replicated with high fidelity on the *goldfingers*.

6.3.3 Intra-class variability between impressions of goldfingers

Five different plain impressions of each *goldfinger* are captured using the single-finger capacitive reader and compared against each other in order to assess the consistency between different impressions of the same *goldfinger*. Table 6.6 shows the range of similarity scores obtained for this experiment. All similarity scores are significantly higher than the verification threshold score of 33 for NIST SD4 at FAR of 0.01%. This shows that different impressions of the same *goldfinger* are highly consistent. In other words, there is low intra-class variability between different impressions of the same *goldfinger*.

Table 6.7 Mean (μ) and std. deviation (σ) of center-to-center spacing (in pixels) in the images of the *goldfingers* captured using the 500 ppi single-finger capacitive reader (CR). Expected grating spacing (in pixels) is shown in brackets.

Test pattern	**CR (500 ppi)**
S0005 (9.45)	$\mu = 9.57$, $\sigma = 0.14$
S0010 (10.20)	$\mu = 10.34$, $\sigma = 0.21$
S0083 (10.44)	$\mu = 10.60$, $\sigma = 0.14$
S0096 (10.24)	$\mu = 10.28$, $\sigma = 0.11$

6.4 Evaluation of Capacitive Readers

In this section, we describe the preliminary experiments to evaluate (i) a large area *PIV* certified 500 ppi single-finger standalone reader, and (ii) small area capacitive readers embedded in smartphones using goldfingers.

6.4.1 Large area reader

Five different plain impressions of each *goldfinger* are captured with the capacitive reader. The ridge spacing in each captured impression is measured using the method proposed in [104]. The average measured ridge spacing from the five impressions of each *goldfinger* is compared to the ridge spacing of the corresponding original fingerprint (computed using the same method [104]) used in the generation of the *goldfinger*. Table 6.7 shows the average and variation in ridge spacing measurements from the five impressions of each goldfinger captured using the reader. Following are the key observations based on this experiment:

- The computed ridge spacing in images of all four goldfingers is, on average, observed to be greater than (but within 0.15 pixels of) the expected spacing. This is most likely due to the flattening of goldfinger gratings when they are pressed against the capacitive reader platen and is consistent with our earlier observation regarding contact-based optical readers. Using the one-sample t-test [151], the computed ridge spacing values are statistically different than the expected values for all goldfingers at a significance level of 0.05. Note, however, that

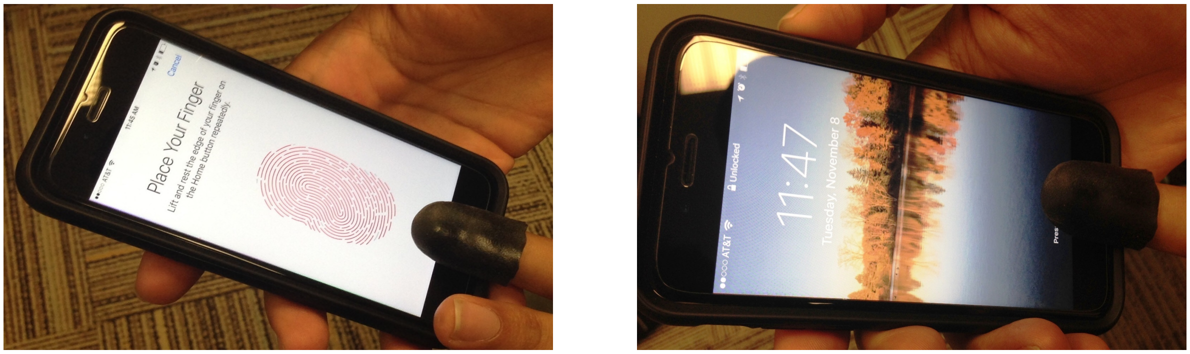

(a) (b)

Figure 6.10 Evaluation of capacitive readers embedded in smartphones using goldfingers. (a) Enrolment of a goldfinger on an Apple iPhone 6s, and (b) unlocking of the iPhone 6s using the same goldfinger.

the increase in ridge spacing observed here is not as significant as that reported with optical readers in chapter 4. To better understand these differences, controlled experimentation with known contact pressure during fingerprint capture is required.

- The average deviation in ridge spacing between different impressions of the same goldfinger is between 0.1-0.2 pixels. These are comparable to the ridge spacing deviation measurements using 3D targets for one of the single-finger optical readers, but slightly greater than spacing measurements reported for the other two optical readers in chapter 4. This is because the capacitive reader has a smaller platen compared to the two optical readers which results in only partially images of the goldfingers. Therefore, overall fewer ridge spacing measurements are used for spacing computations.

6.4.2 Embedded small area readers

We perform feasibility experiments using two different smartphones, the Apple iPhone 6s and the Samsung Galaxy S7[4], and a capacitive reader module designed for smartphones. Figure 6.6 shows the impressions acquired with capacitive reader module designed for smartphones. We first enroll a *goldfinger* using the fingerprint enrolment procedure on the two phones (see Figure 6.10

[4]Commercial smartphones do not provide access to fingerprint images.

(a) (b)

Figure 6.11 Sample 3D finger spoof. (a) Electronic 3D spoof, and (b) physical 3D spoof after conductive carbon coating.

(a)). Subsequently, we make ten independent attempts to unlock the two phones using the enrolled *goldfinger*. The enrolled *goldfinger* template is then deleted and we repeat this procedure using a different *goldfinger*. We were able to successfully unlock the two phones in all our attempts using each of the four *goldfingers* (see Figure 6.10 (b)). This indicates the potential feasibility of using *goldfingers* as targets for evaluating capacitive readers embedded in smartphones.

6.5 Presentation Attacks on Capacitive Readers

Although the primary goal of manufacturing conductive 3D fingerprint artifacts (goldfingers) is evaluation of capacitive readers, a significant by-product is the potential use of such artifacts in performing presentation attacks (spoofing) on capacitive readers. Below, we describe a simple procedure that can be used to create a conductive 3D spoof from a 2D plain fingerprint of a known subject.

1. Use a 3D modeling software, e.g, Meshlab [15] to synthetically generate a cuboidal surface for projecting the 2D print. Set the length and width of the cuboid to at least 3.5 cm and

2.5 cm, respectively. This ensures that there is adequate surface area for projecting the plain print. Also, set the height (wall thickness) of the cuboid to atleast 1 mm for 3D printing the cuboid as a solid object.

2. Use the method described in chapter 4 to create the 3D spoof by etching the plain print onto the cuboidal surface. While creating the electronic spoof, set the 2D to 3D projection scale appropriately (16.79 pixels/mm) to account for 2D to 3D projection error and 3D printing fabrication error. Print the spoof using a high-resolution 3D printer (e.g. Stratasys Objet Connex350) with materials similar in hardness and elasticity to the human skin (e.g. TangoBlackPlus FLX 980).

3. Dip the 3D printed spoof in 2M NaOH solution for approx. 3 hrs. and then rinse it with water. Once it dries, spray coat conductive carbon (e.g. [35]) onto the 3D spoof. This imparts the required conductivity for registering the spoof with capacitive readers[5].

We generated five 3D spoofs from index fingerprints of five different subjects using the aforementioned procedure. The spoofs were fabricated with TangoBlackPlus FLX980. Figure 6.11 shows an example. For conducting spoofing experiments, the index fingerprints of the subjects were enrolled on two different capacitive readers, a single-finger capacitive reader and an embedded capacitive reader in an access control terminal. Verfinger 6.3 SDK was interfaced with the single-finger capacitive reader for performing fingerprint comparisons. For the embedded reader, the fingerprint comparison algorithm built into the access control terminal was used for fingerprint comparisons. Five separate spoofing attempts were made on each of the readers using the five spoofs. In all attempts, we were able to successfully spoof the three readers.

Note, however, that the generated 3D spoofs were not able to spoof the capacitive readers embedded in smartphones. We believe this is because fingerprint comparison algorithms in smartphones use texture-based features in addition to minutiae features. Given that the texture charac-

[5]Spray coating of conductive carbon is non-uniform. Furthermore, the carbon coating only imparts conductivity for a limited time (1-2 hours), and has low abrasion resistance. This process, therefore, cannot be used for creating capacitive 3D targets.

teristics of the created 3D spoofs differ from the human skin, these spoofs are not effective for capacitive readers in smartphones.

6.6 Conclusions

Capacitive fingerprint readers are now being increasingly used in consumer and access control applications, e.g., for smartphone unlock and point of sale (POS) payments. Given the widespread deployment of capacitive readers, an important requirement is to develop standard artifacts and procedures for repeatable evaluation of these readers. In this chapter, we described a procedure to generate 3D targets, termed *goldfingers*, specifically for capacitive reader evaluation. We used a state-of-the-art method to create electronic 3D targets by mapping 2D calibration patterns with known features onto a 3D finger surface. Physical 3D targets were fabricated from electronic 3D models using a state-of-the-art high-resolution 3D printer. A sputter deposition technique was subsequently used to coat the surface of 3D printed targets with a thin layer of titanium and gold particles.

We demonstrated that the 2D calibration pattern features can be replicated with high fidelity on the *goldfingers*. Furthermore, we evaluated a commercially available 500 ppi single-finger capacitive reader using *goldfingers*. We showed that the *goldfingers* can be used as targets for testing capacitive readers embedded in smartphones. The spoof vulnerability of commercially available capacitive readers to presentation attacks using 3D printed spoofs was also assessed.

Chapter 7

Summary

In this dissertation, we have proposed improvements to (i) the design of fingerprint recognition systems for latent fingerprint matching, and (ii) the operational evaluation methods for fingerprint readers using 3D single-finger and whole hand targets. Our contributions are summarized below:

- Design of a top-down matching paradigm for automatic matching of latents to exemplar prints. This framework takes feedback from the top-K candidate prints from the reference database, output by a latent matcher, to improve the overall latent matching accuracy. Our approach can be wrapped around any baseline latent matcher in order to improve its matching performance. To determine the adequacy of feedback, we developed (i) a statistical test based on the distribution of similarity scores between the latent and the top-K candidate exemplars to decide when feedback is required, and (ii) a local quality based metric to determine which latent regions would benefit from feedback in order to improve the similarity score with the true mate. Using the proposed paradigm, the matching performance of a state-of-the-art latent matcher improved by 0.5-3.5% on two latent databases.

- Design of a latent markup crowdsourcing framework where multiple human examiners and the AFIS work in synergy to boost latent matching performance. Given a latent, an AFIS is first used to automatically match the latent against exemplars in the reference database. Based on the output of the AFIS, a statistical test is used to decide if additional markup from fingerprint examiners is required. If so, the latent is crowdsourced to a pool of examiners for providing markups. The set of markups provided by examiners are then individually fed to the AFIS to obtain the new set of similarity scores. The output of the AFIS for different examiners is fused together via score level fusion with the initial automatic match output to improve the overall latent matching accuracy. A greedy crowdsourcing framework is also proposed where instead of crowdsourcing the latent to all examiners at once, examiner markups are obtained incrementally, as determined by our statistical test, to boost the overall accuracy. Significance performance improvement (2.5-11.5%) is obtained using the crowdsourced markups in conjunction with a state-of-the-art latent matcher.

- Design and fabrication of 3D targets for operational evaluation of single-finger optical readers. 2D calibration patterns (e.g., sine gratings and 2D fingerprints with known singular points and minutiae) are projected onto a 3D finger surface to create electronic 3D targets. A state-of-the-art 3D printer is used to fabricate physical 3D targets from the electronic models. A procedure to chemically clean the 3D printed targets using 2M NaOH solution and water is also developed. We measure the (i) 2D to 3D projection error, and (ii) fabrication error introduced by the 3D printer to assess the fidelity of 3D target synthesis and fabrication process. We show that the 2D calibration pattern features are replicated with high fidelity both on electronic and physical 3D targets. We also conduct experiments to estimate the error introduced by three different 500/1000 ppi commercial fingerprint readers using 3D targets created using sine gratings as well as fingerprint patterns.

- Design and fabrication of 3D whole hand targets complete with all four fingerprints and the thumbprint for evaluating slap and contactless fingerprint readers. 2D calibration patterns are mapped to 3D finger surfaces corresponding to each of the five fingers and a fingerless glove is created to generate electronic 3D hand target. 3D physical targets are subsequently printed using a state-of-the-art 3D printer and cleaned with 2M NaOH and water. We show that the 2D calibration pattern features are replicated with high fidelity both on the electronic and physical 3D whole hand targets. We also demonstrate that the manufactured 3D whole hand targets can be used for evaluating three different 500/1000 ppi contact-based slap readers and a contactless slap reader.

- Fabrication of conductive 3D targets for evaluation of capacitive fingerprint readers. The 3D printed targets are electrically non-conductive. To impart conductivity, the surface of 3D printed targets is coated with thin layers of metals (titanium + gold) using DC sputtering. We show that this process imparts conductivity to image the targets with capacitive readers without degrading the fidelity of engraved features on the target. The fabricated conductive 3D targets are used for evaluating standalone as well as embedded capacitive readers. A simple procedure to create 3D printed spoofs for performing presentation attacks on capacitive readers is also described. We show that the 3D printed spoofs can successfully spoof a 500 ppi single-finger commercial capacitive reader and a capacitive reader embedded on an access control terminal.

7.1 Future Work

Following are some possible future research directions for the problems investigated in this thesis:

- **Feedback paradigm for latent matching**: Incorporate level-2 fingerprint features such as ridge skeleton and minutiae into the feedback paradigm to further improve latent matching accuracy.

- **Latent markup crowdsourcing framework**: Validate the proposed framework against a larger reference database of a few million reference prints. Explore ensemble-based meta algorithms such as bagging and boosting to further improve the matching performance of AFIS.

- **3D single-finger and whole hand targets**: Explore methods to build universal 3D targets with the optical and electrical properties similar to human skin for use with both optical and capacitive readers, e.g., by creating a negative (mold) of the 3D targets and then casting universal targets with appropriate materials. Investigate procedures to impart conductivity to targets manufactured via molding and casting, e.g, mixing conductive inks to casting materials. This would facilitate benchmarking of different optical and capacitive readers using the same target, as well as investigation of reader interoperability using 3D targets. Further, experimental procedures based on 3D targets can potentially be useful to revise the existing fingerprint evaluation standards (*PIV/Appendix F*). Simulate the effects of dry and worn out fingers using 3D targets with different depths of engravings to further study the imaging capabilities of different readers. Study how user-induced variabilities, e.g. contact-pressure applied on the reader platen and relative finger orientations with respect to each other as well as the reader platen, impact the quality of the captured fingerprint images. To do this, controlled experimentation where known contact-pressure is applied on the reader platen while capturing fingerprint impressions is required. Develop anti-spoofing solutions to prevent presentation attacks using 3D printed spoofs.

BIBLIOGRAPHY

BIBLIOGRAPHY

[1] Apple Pay. http://www.apple.com/apple-pay/.

[2] Artec Eva 3D scanner. http://www.artec3d.com/hardware/artec-eva/.

[3] Contactless Fingerprint Capture, National Institute of Standards and Technology. http://www.nist.gov/itl/iad/ig/contactless_fingerprint.cfm.

[4] Denton Vacuum Desktop Pro Sputtering System. http://www.dentonvacuum.com/technologies/production-solutions/desktop-pro/.

[5] Diameter of a Human Hair. http://hypertextbook.com/facts/1999/BrianLey.shtml.

[6] ELFT-EFS public challenge dataset. http://biometrics.nist.gov/cs_links/latent/elft-efs/ELFT-EFSPublicChallenge_2009-04-23.pdf.

[7] Faster and Better Fingerprinting: The Fast Capture Initiative, National Institute of Justice. http://www.nij.gov/topics/technology/biometrics/pages/fast-capture-initiative.aspx.

[8] FBI Biospecs IAFIS FAQs. https://www.fbibiospecs.org/iafis_faq.html.

[9] FBI IAFIS certified product listing. http://www.fbi.gov/about-us/cjis/fingerprints_biometrics/iafis/iafis_cert.

[10] FlashScan3D touchless fingerprint sensor. http://www.flashscan3d.com/.

[11] Keyence Digital Microscope VHX-600. http://www1.keyence.eu/products/microscope/microscope/vhx6002/vhx6002_specifications_1.php.

[12] Kurt J. Lesker Gold (Au) Sputtering Targets. http://www.lesker.com/newweb/deposition_materials/depositionmaterials_sputtertargets_1.cfm?pgid=au1.

[13] Kurt J. Lesker Titanium (Ti) Sputtering Targets. http://www.lesker.com/newweb/deposition_materials/depositionmaterials_sputtertargets_1.cfm?pgid=ti1.

[14] Meet Phannie, NIST's Standard "Phantom" for Calibrating MRI Machines. http://www.nist.gov/pml/electromagnetics/phannie_051110.cfm.

[15] Meshlab. http://sourceforge.net/projects/meshlab/.

[16] Moire effect. http://whatis.techtarget.com/definition/moire-effect.

[17] Morpho Finger on the Fly. http://www.morpho.com/identification/border-control-242/semi-automated-control/finger-on-the-fly-r-946/?lang=en.

[18] NIST SD27 Latent Database. http://www.nist.gov/srd/nistsd27.cfm.

[19] NIST Special Database 4. http://www.nist.gov/srd/nistsd4.cfm.

[20] Office of Biometric Identity Management Identification Services. http://www.dhs.gov/obim-biometric-identification-services.

[21] ONEprint touchless fingerprint reader. http://www.idairco.com/products/.

[22] Operation ASHA's healthcare e-compliance biometric system. http://www.opasha.org/our-work/ecompliance-innovation-and-health/.

[23] Recording Legible Fingerprints, Federal Bureau of Investigation. https://www.fbi.gov/about-us/cjis/fingerprints_biometrics/recording-legible-fingerprints.

[24] Ron Smith and Associates. http://www.ronsmithandassociates.com/.

[25] Samsung Fingerprint Sensor. http://www.samsung.com/us/support/answer/ANS00039905/997339942/SM-G920TZKATMB.

[26] Samsung Pay. http://www.samsung.com/us/samsung-pay/.

[27] Statista: NFC mobile payment users worldwide from 2012 to 2018. http://www.statista.com/statistics/461512/nfc-mobile-payment-users-worldwide/.

[28] Statista: Number of smartphone users worldwide from 2014 to 2019. http://www.statista.com/statistics/330695/number-of-smartphone-users-worldwide/.

[29] Statista: Penetration of smartphones with fingerprint sensors from 2014 to 2018. http://www.statista.com/statistics/522058/global-smartphone-fingerprint-penetration/.

[30] Stratasys Digital Materials (DMs) Data Sheet. http://www.stratasys.com/~/media/Main/Secure/Material%20Specs%20MS/PolyJet-Material-Specs/Digital_Materials_Datasheet.pdf.

[31] Stratasys Polyjet Material Data Sheet. http://www.stratasys.com/~/media/Main/Secure/Material%20Specs%20MS/PolyJet-Material-Specs/PolyJet_Materials_Data_Sheet.pdf.

[32] TBS contactless 3D fingerprint sensor. http://www.tbs-biometrics.com/en/hardware/3d-enroll.html.

[33] Thor Labs Calibration Targets. http://www.thorlabs.com/newgrouppage9.cfm?objectgroup_id=7502.

[34] Torso Phantom. https://www.kyotokagaku.com/products/detail03/ph-4.html.

[35] Total Ground Carbon Conductive Coating. http://www.unicornelex.com/ProductDetails.asp?ProductCode=26-0801&gclid=CN7Nh5qmv88CFQMdaQodkNMNNA.

[36] TouchID System. http://support.apple.com/kb/ht5949.

[37] UID Biometric Device Certification. http://www.uidai.gov.in/biometric-device-certification.html.

[38] Unique Identification Authority of India. http://uidai.gov.in/.

[39] Vertex Displacement Mapping using GLSL. http://www.ozone3d.net/tutorials/vertex_displacement_mapping_p02.php.

[40] Walt Disney World. https://disneyworld.disney.go.com/.

[41] X-Ray Phantom Hand. http://www.anatomicalmodel.eu/x-ray-phantom-hand-transparent.

[42] Biometric Design Standards for UID Applications v 1.0. *UIDAI Committee on Biometrics*, Dec 2009.

[43] Guidance to applicant for biometric devices for UID Application (BDCS-03-02). *STQC IT Services*, Dec 2010.

[44] Latent Print Examination and Human Factors: Improving the Practice through a Systems Approach. Technical report, U.S. Department of Commerce, National Institute of Technology, 2012.

[45] Forensic Science in Criminal Courts: Ensuring Scientific Validity of Feature-Comparison Methods. Technical report, Presidents Council of Advisors on Science and Technology (PCAST), 2016.

[46] Qualcomm Snapdragon Sense. https://www.qualcomm.com/products/snapdragon/security/sense-id, 2016.

[47] A. Abhyankar and S. Schuckers. Fingerprint liveness detection using local ridge frequencies and multiresolution texture analysis techniques. In *IEEE International Conference on Image Processing (ICIP)*, pages 321–324, 2006.

[48] D. Alemu, H. Wei, K. Ho, and C. Chu. Highly conductive PEDOT: PSS electrode by simple film treatment with methanol for ito-free polymer solar cells. *Energy & Environmental Science*, 5(11):9662–9671, 2012.

[49] P. Alliez, D. Cohen-Steiner, O. Devillers, B. Lévy, and M. Desbrun. Anisotropic polygonal remeshing. In *ACM Transactions on Graphics (TOG)*, volume 22, pages 485–493, 2003.

[50] F. Alonso-Fernandez, J. Bigun, J. Fierrez, H. Fronthaler, K. Kollreider, and J. Ortega-Garcia. Fingerprint Recognition. In *Guide to Biometric Reference Systems and Performance Evaluation*, pages 51–88. Springer, 2009.

[51] N. Amenta, M. Bern, and D. Eppstein. The crust and the β-skeleton: Combinatorial curve reconstruction. *Graphical Models and Image Processing*, 60(2):125–135, 1998.

[52] S. S. Arora, K. Cao, A. K. Jain, and G. Michaud. Crowd powered latent fingerprint identification: fusing AFIS with examiner markups. In *International Conference on Biometrics (ICB)*, pages 363–370, 2015.

[53] S. S. Arora, K. Cao, A. K. Jain, and N. G. Paulter Jr. 3D Fingerprint Phantoms. In *22nd International Conference on Pattern Recognition (ICPR)*, pages 684–689, 2014.

[54] S. S. Arora, K. Cao, A. K. Jain, and N. G. Paulter Jr. Design and Fabrication of 3D Fingerprint Targets. *IEEE Transactions on Information Forensics and Security*, 11(10):2284–2297, 2016.

[55] S. S. Arora, A. K. Jain, and N.G. Paulter Jr. 3d Whole Hand Targets: Evaluating Slap and Contactless Fingerprint Readers. In *International Conference of the Biometrics Special Interest Group (BIOSIG)*, 2016.

[56] S. S. Arora, E. Liu, K. Cao, and A. K. Jain. Latent Fingerprint Matching: Performance Gain via Feedback from Exemplar Prints. *IEEE Transactions on Pattern Analysis and Machine Intelligence*, 36(12):2452–2465, 2014.

[57] D. R. Ashbaugh. *Quantitative-Qualitative Friction Ridge Analysis: An Introduction to Basic and Advanced Ridgeology*. CRC Press, 1999.

[58] C. A. Bishop. Transparent Conducting Coatings on Polymer Substrates for Touchscreens and Displays. In *Handbook of Visual Display Technology*, pages 975–988. Springer, 2012.

[59] R. Black. *Managing the Testing Process*. John Wiley & Sons, 2002.

[60] D. A. Boas, C. Pitris, and N. Ramanujam. *Handbook of Biomedical Optics*. Taylor & Francis, 2011.

[61] M. Bodén. A guide to recurrent neural networks and backpropagation. *The DALLAS project. Report from the NUTEK-supported project AIS-8, SICS. Holst: Application of data analysis with learning systems*, (2):1–10, 2001.

[62] M. Boehme and C. Charton. Properties of ITO on PET film in dependence on the coating conditions and thermal processing. *Surface and Coatings Technology*, 200(1):932–935, 2005.

[63] E. Borenstein and S. Ullman. Combined top-down/bottom-up segmentation. *IEEE Transactions on Pattern Analysis and Machine Intelligence*, 30(12):2109–2125, 2008.

[64] K. Cao and A. K Jain. Latent Orientation Field Estimation via Convolutional Neural Network. In *IAPR International Conference on Biometrics*, pages 1–8, 2015.

[65] K. Cao and A. K. Jain. Hacking mobile phones using 2D printed fingerprints. *Michigan State University Technical Report, MSU-CSE-16-2*, 2016.

[66] K. Cao, E. Liu, and A. K. Jain. Segmentation and enhancement of latent fingerprints: A coarse to fine ridge structure dictionary. *IEEE Transactions on Pattern Analysis and Machine Intelligence*, 36(9):1847–1859, 2014.

[67] R. Cappelli. SFinGe: an approach to synthetic fingerprint generation. In *International Workshop on Biometric Technologies (BT2004)*, pages 147–154, 2004.

[68] R. Cappelli, M. Ferrara, and D. Maltoni. Minutia cylinder-code: A new representation and matching technique for fingerprint recognition. *IEEE Transactions on Pattern Analysis and Machine Intelligence*, 32(12):2128–2141, 2010.

[69] R. Cappelli, D. Maio, and D. Maltoni. Synthetic fingerprint-database generation. In *16th IEEE International Conference on Pattern Recognition*, volume 3, pages 744–747, 2002.

[70] G. Casella and R. L. Berger. *Statistical Inference*, volume 70. Duxbury Press Belmont, CA, 1990.

[71] C. Champod, C. J. Lennard, P. Margot, and M. Stoilovic. *Fingerprints and Other Ridge Skin Impressions*. CRC press, 2004.

[72] Y. A. Chizmadzhev, A. V. Indenbom, P. I. Kuzmin, S. V. Galichenko, J. C. Weaver, and R. O. Potts. Electrical properties of skin at moderate voltages: contribution of appendageal macropores. *Biophysical Journal*, 74(2):843–856, 1998.

[73] D. Cho, K. Kim, T. Kim, Y. Noh, S. Na, K. Chung, and H. Kim. Transparent and flexible amorphous InZnAlO films grown by roll-to-roll sputtering for acidic buffer-free flexible organic solar cells. *Organic Electronics*, 24:227–233, 2015.

[74] H. Choi, M. Boaventura, I. A. G. Boaventura, and A. K. Jain. Automatic segmentation of latent fingerprints. In *IEEE Fifth International Conference on Biometrics: Theory, Applications and Systems*, pages 303 –310, 2012.

[75] H. Choi, A. Nagar, and A. K. Jain. On the evidential value of fingerprints. In *International Joint Conference on Biometrics (IJCB)*, pages 1–8, 2011.

[76] S. A. Cole. *Suspect Identities: A History of Fingerprinting and Criminal Identification*. Harvard University Press, 2009.

[77] B. Coppin. *Artificial Intelligence Illuminated*. Jones & Bartlett Learning, 2004.

[78] National Research Council. Strengthening Forensic Science in the United States: A Path Forward. 2009.

[79] Polk County Sherrif's office. Fingerprinting Service. http://www.polksheriff.org/INSIDEPCSO/OBA/HR/Pages/FingerprintingService.aspx.

[80] J. Daugman. 600 million citizens of India are now enrolled with biometric ID. http://spie.org/x108321.xml, 2014.

[81] Delta ID - Mobile Security. http://www.deltaid.com/.

[82] M. Desbrun, M. Meyer, and P. Alliez. Intrinsic parameterizations of surface meshes. In *Computer Graphics Forum*, volume 21, pages 209–218, 2002.

[83] T. G. Dietterich. Ensemble methods in machine learning. In *Multiple Classifier Systems*, pages 1–15. Springer, 2000.

[84] E. W. Dijkstra. A note on two problems in connexion with graphs. *Numerische Mathematik*, 1(1):269–271, 1959.

[85] I. E. Dror, A. E. Peron, S. L. Hind, and D. Charlton. When emotions get the better of us: the effect of contextual top-down processing on matching fingerprints. *Applied Cognitive Psychology*, 19(6):799–809, 2005.

[86] I. E. Dror, K. Wertheim, P. Fraser-Mackenzie, and J. Walajtys. The Impact of Human–Technology Cooperation and Distributed Cognition in Forensic Science: Biasing Effects of AFIS Contextual Information on Human Experts. *Journal of Forensic Sciences*, 57(2):343–352, 2012.

[87] R. O. Duda, P. E. Hart, and D. G. Stork. *Pattern Classification*. John Wiley and Sons Inc., second edition, 2001.

[88] C. Edwards and R. Marks. Evaluation of biomechanical properties of human skin. *Clinics in Dermatology*, 13(4):375–380, 1995.

[89] V. Falanga and B. Bucalo. Use of a durometer to assess skin hardness. *Journal of the American Academy of Dermatology*, 29(1):47–51, 1993.

[90] H. Faulds. On the Skin-Furrows of the Hand. *Nature*, 22:605, 1880.

[91] Federal Bureau of Investigation. Integrated Automated Fingerprint Identification System (IAFIS). http://www.fbi.gov/about-us/cjis/fingerprints_biometrics/iafis.

[92] J. Feng and A. K. Jain. Fingerprint reconstruction: From minutiae to phase. *IEEE Transactions on Pattern Analysis and Machine Intelligence*, 33(2):209–223, 2011.

[93] J. Feng, J. Zhou, and A. K. Jain. Orientation field estimation for latent fingerprint enhancement. *IEEE Transactions on Pattern Analysis and Machine Intelligence*, 35(4):925–940, 2013.

[94] H. Fronthaler, K. Kollreider, and J. Bigun. Local features for enhancement and minutiae extraction in fingerprints. *IEEE Transactions on Image Processing*, 17(3):354–363, 2008.

[95] J. Galbally, F. Alonso-Fernandez, J. Fierrez, and J. Ortega-Garcia. A high performance fingerprint liveness detection method based on quality related features. *Future Generation Computer Systems*, 28(1):311–321, 2012.

[96] F. Galton. *Finger Prints*. MacMillan, 1892.

[97] Francis Galton. Personal dentification and description. *Journal of Anthropological Institute of Great Britain and Ireland*, pages 177–191, 1889.

[98] E. German. Latent Print Examination. http://www.onin.com/fp/, 2007.

[99] L. Ghiani, A. Hadid, G. L. Marcialis, and F. Roli. Fingerprint liveness detection using binarized statistical image features. In *IEEE Sixth International Conference on Biometrics: Theory, Applications and Systems (BTAS)*, pages 1–6, 2013.

[100] L. K. Hansen and P. Salamon. Neural network ensembles. *IEEE Transactions on Pattern Analysis and Machine Intelligence*, 12(10):993–1001, 1990.

[101] M. R. Hawthorne. *Fingerprints: Analysis and Understanding*. CRC Press, 2009.

[102] W. J. Herschel. *The Origins of Fingerprinting*. Oxford University Press, 1916.

[103] J. G. Hollands and C. D. Wickens. *Engineering Psychology and Human Performance.* Prentice Hall, New Jersey, 1999.

[104] L. Hong, Y. Wan, and A. K. Jain. Fingerprint image enhancement: algorithm and performance evaluation. *IEEE Transactions on Pattern Analysis and Machine Intelligence*, 20(8):777–789, 1998.

[105] IBG. Synthetic biometric image generator. *Department of Homeland Security Small Business Innovation Research Final Report*, 2012.

[106] H. Im, H. Hong, J. Lee, J. Lee, Y. Heo, and J. Kim. Structural and electrical properties of al and b co-doped zno thin films. *Journal of Nanoelectronics and Optoelectronics*, 6(3):301–305, 2011.

[107] Applied Image Inc. Seimens/star sector target. https://www.appliedimage.com/products/test-targets-and-charts-1/rit-siemens-sayce-and-other-test-targets/siemens-star-sector-target-t-50.

[108] M. Indovina, V. Dvornychenko, R. A. Hicklin, and G. I. Kiebuzinski. ELFT-EFS Evaluation of Latent Fingerprint Technologies: Extended Feature Sets [Evaluation# 2]. *NISTIR*, 7859, 2012.

[109] M. Indovina, R. A. Hicklin, and G. I. Kiebuzinski. ELFT-EFS Evaluation of Latent Fingerprint Technologies: Extended Feature Sets [Evaluation# 1]. *NISTIR*, 7775, 2011.

[110] A. K. Jain. Fingerprints: Proving ground for pattern recognition. *International Conference on Pattern Recognition (ICPR)*, 2006.

[111] A. K. Jain. Technology: Biometric Recognition. *Nature*, 449(7158):38–40, 2007.

[112] A. K. Jain, S. S. Arora, L. Best-Rowden, K. Cao, P. S. Sudhish, and A. Bhatnagar. Biometrics for child vaccination and welfare: Persistence of fingerprint recognition for infants and toddlers. *arXiv preprint arXiv:1504.04651*, 2015.

[113] A. K Jain, S. S. Arora, L. Best-Rowden, K. Cao, P. S. Sudhish, A. Bhatnagar, and Y. Koda. Giving Infants an Identity: Fingerprint Sensing and Recognition. In *8th International Conference on Information and Communication Technologies and Development*, page 29, 2016.

[114] A. K. Jain, K. Cao, and S. S. Arora. Recognizing infants and toddlers using fingerprints: Increasing the vaccination coverage. In *IEEE International Joint Conference on Biometrics (IJCB)*, pages 1–8, 2014.

[115] A. K. Jain, Y. Chen, and M. Demirkus. Pores and ridges: high-resolution fingerprint matching using level 3 features. *IEEE Transactions on Pattern Analysis and Machine Intelligence*, 29(1):15–27, 2007.

[116] A. K. Jain and J. Feng. Latent palmprint matching. *IEEE Transactions on Pattern Analysis and Machine Intelligence*, 31(6):1032–1047, 2009.

[117] A. K. Jain and J. Feng. Latent fingerprint matching. *IEEE Transactions on Pattern Analysis and Machine Intelligence*, 33(1):88–100, 2011.

[118] A. K. Jain, P. Flynn, and A. A. Ross. *Handbook of Biometrics*. Springer, 2007.

[119] A. K. Jain, L. Hong, and R. Bolle. On-line fingerprint verification. *IEEE Transactions on Pattern Analysis and Machine Intelligence*, 19(4):302–314, 1997.

[120] A. K. Jain and S. Z. Li. *Handbook of Face Recognition*. Springer, 2011.

[121] A. K. Jain, K. Nandakumar, and A. Ross. Score normalization in multimodal biometric systems. *Pattern Recognition*, 38(12):2270–2285, 2005.

[122] A. K. Jain, K. Nandakumar, and A. Ross. 50 years of Biometric Research: Accomplishments, Challenges, and Opportunities ". *Pattern Recognition Letters*, 2016.

[123] A. K. Jain, S. Prabhakar, and S. Pankanti. On the Similarity of Identical Twin Fingerprints. *Pattern Recognition*, 35(11):2653–2663, 2002.

[124] A. K. Jain and A. Ross. Bridging the gap: From biometrics to forensics. *Philosophical Transactions of the Royal Society B*, 370(1674):20140254, 2015.

[125] A. K. Jain and D. Zongker. Feature selection: Evaluation, application, and small sample performance. *IEEE Transactions on Pattern Analysis and Machine Intelligence*, 19(2):153–158, 1997.

[126] Z. Jin, A. B. J. Teoh, T. S. Ong, and C. Tee. Fingerprint template protection with minutiae-based bit-string for security and privacy preserving. *Expert Systems with Applications*, 39(6):6157–6167, 2012.

[127] G. K. Johnsen. *Skin electrical properties and physical aspects of hydration of keratinized tissues*. PhD thesis, University of Oslo, 2010.

[128] I. Jolliffe. *Principal Component Analysis*. Wiley Online Library, 2005.

[129] R. Kimmel and J. A. Sethian. Computing geodesic paths on manifolds. *Proceedings of the National Academy of Sciences*, 95(15):8431–8435, 1998.

[130] P. Komarinski. *Automated Fingerprint Identification Systems (AFIS)*. Academic Press, 2005.

[131] J. B. Kruskal and M. Wish. *Multidimensional Scaling*. Sage, 1978.

[132] S. Lalitha and N. Kumar. Multiple outlier test for upper outliers in an exponential sample. *Journal of Applied Statistics*, 39(6), 2012.

[133] H. O. Lancaster and E. Seneta. *Chi-Square Distribution*. Wiley Online Library, 1969.

[134] T. Lewis and N. R. J. Fieller. A recursive algorithm for null distributions for outliers: I. gamma samples. *Technometrics*, 21(3):371–376, 1979.

[135] E. Liu, S. S. Arora, K. Cao, and A. K. Jain. A feedback paradigm for latent fingerprint matching. In *International Conference on Biometrics (ICB)*, pages 1–8, 2013.

[136] C. Loop. Smooth subdivision surfaces based on triangles. Master's thesis, University of Utah, 1987.

[137] Dongguan Hongcheng Optical Products Ltd. Vision calibration grid targets. http://hcgxcy.en.ec21.com/Opencv_Vision_Calibration_Grid_Targets--8591570_8603700.html.

[138] Y. Lu, H. Tang, S. Fung, Q. Wang, J. M. Tsai, M. Daneman, B. E. Boser, and D. A. Horsley. Ultrasonic fingerprint sensor using a piezoelectric micromachined ultrasonic transducer array integrated with complementary metal oxide semiconductor electronics. *Applied Physics Letters*, 106(26):263503, 2015.

[139] A. V. Maceo. Anatomy and physiology of adult friction ridge skin. *The Fingerprint Sourcebook*, 2011.

[140] V. Mäkinen and E. Ukkonen. Point pattern matching. In *Encyclopedia of Algorithms*, pages 657–660. Springer, 2008.

[141] D. Maltoni, D. Maio, A. K. Jain, and S. Prabhakar. *Handbook of Fingerprint Recognition*. Springer, 2009.

[142] Del Mar Live Scan. San Diego Fingerprinting. http://www.delmarlivescan.com/san-diego-fingerprinting-services/.

[143] E. Marasco and A. Ross. A survey on antispoofing schemes for fingerprint recognition systems. *ACM Computing Surveys*, 47(2):28, 2015.

[144] T. Matsumoto. Gummy and conductive silicone rubber fingers importance of vulnerability analysis. In *Advances in Cryptology-ASIACRYPT 2002*, pages 574–575. Springer, 2002.

[145] T. Matsumoto, H. Matsumoto, K. Yamada, and S. Hoshino. Impact of artificial gummy fingers on fingerprint systems. In *Electronic Imaging*, pages 275–289, 2002.

[146] Neurotechnology Inc. Verifinger. http://www.neurotechnology.com/verifinger.html.

[147] NIST Special Database 14. http://www.nist.gov/srd/nistsd14.cfm.

[148] NIST Special Database 27. http://www.nist.gov/srd/nistsd27.cfm.

[149] U.S. Marshals Service for Students. http://www.usmarshals.gov/usmsforkids/fingerprint_history.htm.

[150] West Virginia University (WVU) latent fingerprint database. http://www.cse.msu.edu/~rossarun/.

[151] D. S. Moore. *The Basic Practice of Statistics*, volume 2. WH Freeman, 2007.

[152] A. Nagar and A. K. Jain. On the security of non-invertible fingerprint template transforms. In *International Workshop on Information Forensics and Security (WIFS)*, pages 81–85, 2009.

[153] A. Nagar, K. Nandakumar, and A. K. Jain. Securing fingerprint template: Fuzzy vault with minutiae descriptors. In *19th International Conference on Pattern Recognition*, pages 1–4, 2008.

[154] K. Nandakumar and A. K. Jain. Biometric template protection: Bridging the performance gap between theory and practice. *IEEE Signal Processing Magazine*, 32(5):88–100, 2015.

[155] N. B. Nill. Test procedures for verifying image quality requirements for personal identity verification (PIV) single finger capture devices. Technical Report MTR 060170, MITRE, 2006.

[156] N. B. Nill. Test procedures for verifying IAFIS image quality requirements for fingerprint scanners and printers v 1.4. Technical Report MTR 05B0016R7, MITRE, 2013.

[157] NIST. Summary of results from ELFT07 Phase I Testing. http://fingerprint.nist.gov/latent/elft07/phase1_aggregate.pdf, 2007.

[158] U.S. Department of Homeland Security. New Biometric Technology improves security and facilitates U.S. entry process for International Travelers. https://www.dhs.gov/xlibrary/assets/usvisit/usvisit_edu_10-fingerprint_consumer_friendly_content_1400_words.pdf.

[159] Federal Bureau of Investigation. *The Science of Fingerprints: Classification and Uses*. United States Department of Justice, 1984.

[160] Federal Bureau of Investigation. Next Generation Identification. http://www.fbi.gov/about-us/cjis/fingerprints_biometrics/ngi, 2012.

[161] A. Oliva, A. Torralba, M. S. Castelhano, and J. M. Henderson. Top-down control of visual attention in object detection. In *Proceedings of International Conference on Image Processing*, volume 1, pages I–253, 2003.

[162] N. M. Oliver, B. Rosario, and A. P. Pentland. A bayesian computer vision system for modeling human interactions. *IEEE Transactions on Pattern Analysis and Machine Intelligence*, 22(8):831–843, 2000.

[163] Precision Optics. Calibration targets. http://www.pog.eu/en/ms/sms-calibration-targets.html.

[164] S. Pankanti, S. Prabhakar, and A. K. Jain. On the individuality of fingerprints. *IEEE Transactions on Pattern Analysis and Machine Intelligence*, 24(8):1010–1025, 2002.

[165] G. Parziale and Y. Chen. Advanced technologies for touchless fingerprint recognition. In M. Tistarelli, S. Z. Li, and R. Chellappa, editors, *Handbook of Remote Biometrics*, Advances in Pattern Recognition, pages 83–109. Springer, 2009.

[166] A. A. Paulino, J. Feng, and A. K. Jain. Latent fingerprint matching using descriptor-based Hough transform. *IEEE Transactions on Information Forensics and Security*, 8(1):31–45, 2013.

[167] G. Peyré and L. D. Cohen. Geodesic remeshing using front propagation. *International Journal of Computer Vision*, 69(1):145–156, 2006.

[168] D. Retelny, S. Robaszkiewicz, A. To, W. Lasecki, J. Patel, N. Rahmati, T. Doshi, M. Valentine, and M. S. Bernstein. Expert crowdsourcing with flash teams. In *ACM Symposium on User Interface Software and Technology*, 2014.

[169] R. K. Rowe, S. P. Corcoran, K. A. Nixon, and R. E. Ostrom. Multispectral imaging for biometrics. In *Biomedical Optics*, pages 90–99, 2005.

[170] S. Sangiorgi, A. Manelli, T. Congiu, A. Bini, G. Pilato, M. Reguzzoni, and M. Raspanti. Microvascularization of the Human Digit as Studied by Corrosion Casting. *Journal of Anatomy*, 204(2):123–131, 2004.

[171] K. Seshan. *Handbook of Thin Film Deposition*. William Andrew, 2012.

[172] N. C. Sickler and S. J. Elliott. An evaluation of fingerprint image quality across an elderly population vis-a-vis an 18-25 year old population. In *International Carnahan Conference on Security Technology*, pages 68–73, 2005.

[173] C. Su and S. N. Srihari. Generative models for fingerprint individuality using ridge models. In *19th International Conference on Pattern Recognition (ICPR)*, pages 1–4, 2008.

[174] C. Su and S. N. Srihari. Probability of random correspondence for fingerprints. In *Computational forensics*, pages 55–66. Springer, 2009.

[175] T. Swain. Vacuum Technology 60A & 60B: Thin Film Deposition Processes. http://lpc1.clpccd.cc.ca.us/lpc/tswain/chapt14.pdf.

[176] T. Takano, H. Masunaga, A. Fujiwara, H. Okuzaki, and T. Sasaki. PEDOT nanocrystal in highly conductive PEDOT:PSS polymer films. *Macromolecules*, 45(9):3859–3865, 2012.

[177] J. B. Tenenbaum, V. De Silva, and J. C. Langford. A global geometric framework for nonlinear dimensionality reduction. *Science*, 290(5500):2319–2323, 2000.

[178] M. Tico and P. Kuosmanen. Fingerprint matching using an orientation-based minutia descriptor. *IEEE Transactions on Pattern Analysis and Machine Intelligence*, 25(8):1009–1014, 2003.

[179] M. Trauring. Automatic Comparison of Finger-ridge Patterns. *Nature*, 197:938–940, 1963.

[180] V. V. Tuchin, A. N. Bashkatov, E. A. Genina, V. I. Kochubey, V. V. Lychagov, S. A. Portnov, N. A. Trunina, D. R. Miller, S. Cho, and H. Oh. Finger tissue model and blood perfused skin tissue phantom. *Proc. SPIE*, 7898:78980Z–78980Z–11, 2011.

[181] B. T. Ulery, R. A. Hicklin, J. Buscaglia, and M. A. Roberts. Repeatability and reproducibility of decisions by latent fingerprint examiners. *PloS one*, 7(3):e32800, 2012.

[182] U. Uludag and A. Jain. Securing fingerprint template: Fuzzy vault with helper data. In *International Conference on Computer Vision and Pattern Recognition Workshop*, pages 163–169, 2006.

[183] M. Vatsa, R. Singh, S. Bharadwaj, H. Bhatt, and R. Mashruwala. Analyzing fingerprints of Indian population using image quality: a UIDAI case study. In *International Workshop on Emerging Techniques and Challenges for Hand-Based Biometrics*, pages 1–5, 2010.

[184] C. Watson, G. Fiumara, E. Tabassi, S. L. Cheng, P. Flanagan, and W. Salamon. Fingerprint Vendor Technology Evaluation, NISTIR 8034. http://nvlpubs.nist.gov/nistpubs/ir/2014/NIST.IR.8034.pdf, 2012.

[185] C. Wilson. Fingerprint Vendor Technology Evaluation 2003: Summary of Results and Analysis Report, NISTIR 7123. http://fpvte.nist.gov/report/ir_7123_analysis.pdf, 2004.

[186] S. Yoon, K. Cao, E. Liu, and A. K. Jain. LFIQ: Latent fingerprint image quality. In *IEEE International Conference on Biometrics: Theory, Applications and Systems*, pages 1–8, 2013.

[187] S. Yoon, J. Feng, and A. K. Jain. On latent fingerprint enhancement. In *SPIE Conference Series*, volume 7667, pages 766707_01–766707_10, 2010.

[188] S. Yoon, J. Feng, and A. K. Jain. Altered fingerprints: Analysis and detection. *IEEE Transactions on Pattern Analysis and Machine Intelligence*, 34(3):451–464, 2012.

[189] S. Yoon and A. K. Jain. Longitudinal study of fingerprint recognition. *Proceedings of the National Academy of Sciences*, 112(28):8555–8560, 2015.

[190] S. Yoon, E. Liu, and A. K. Jain. On latent fingerprint image quality. In *Proceedings of International Workshop on Computational Forensics*, 2012.

[191] Z. Zhai, P. Sempolinski, D. Thain, G. Madey, D. Wei, and A. Kareem. Expert-citizen engineering: “crowdsourcing” skilled citizens. In *IEEE Digital Avionics Systems Conference*, 2011.

[192] Q. Zhao, A. K. Jain, N. G. Paulter Jr, and M. Taylor. Fingerprint image synthesis based on statistical feature models. In *IEEE Fifth International Conference on Biometrics: Theory, Applications and Systems (BTAS)*, pages 23–30, 2012.

[193] Y. Zhu, S. C. Dass, and A. K. Jain. Statistical models for assessing the individuality of fingerprints. *IEEE Transactions on Information Forensics and Security*, 2(3):391–401, 2007.